Doctoral Dissertation

博士論文

Three-dimensional Dirac electrons in Sr$_3$PbO antiperovskite

(Sr$_3$PbO アンチペロブスカイト における三次元ディラック電子)

A Dissertation Submitted for the Degree of Doctor of Philosophy

December, 2019

令和元年 12 月博士 (理学) 申請

Department of Physics, Graduate School of Science, The University of Tokyo

東京大学大学院理学系研究科
物理学専攻

Shota Suetsugu
末次 祥大

Abstract

Three-dimensional (3D) topological Dirac semimetals (TDSs) with 3D linear dispersion in bulk have been attracting considerable interest. 3D TDS can host topological surface states and can be driven into topologically distinct phases such as a topological insulating or a Weyl semimetallic state by controlling a band gap or breaking symmetry. Because of the possible realization of chiral anomaly, the quantum limit where all carriers reside in the lowest Landau level has been studied with great interest. Nontrivial topology of conduction and valence bands mixing in Dirac semimetals can give rise to giant orbital diamagnetism. To explore such unconventional physics of 3D Dirac electrons, chemically flexible 3D TDS, in which it is easy to break symmetries, to introduce magnetism, and to control band filling and spin-orbit coupling, is highly desirable. Recently, a family of cubic antiperovskite A_3TtO (A = Ca, Sr, Ba; Tt = Sn, Pb) was theoretically proposed as a 3D massive Dirac electron system, free from the contribution from other parabolic bands. The antiperovskite family with chemical flexibility is promising for band engineering of 3D Dirac electrons.

In this thesis, we report the magnetotransport, the bulk magnetic susceptibility and the nuclear magnetic resonance (NMR) experiments on Sr_3PbO, one of the antiperovskite family. The Hall resistivity and Shubnikov-de Haas oscillation measurements indicate a low density of holes $n \sim 10^{18}$ cm^{-3} with an extremely light cyclotron mass of $\sim 0.01m_e$, one percent of free electron. A linear magnetoresistance (MR) with a giant MR ratio $\Delta\rho_{xx}(B)/\rho_{xx}(0) \sim 10$ was observed similar to other 3D TDSs. The temperature dependence of NMR spin lattice relaxation rate T_1^{-1} with the deviation from the Korringa behavior at high temperature reflects a V shaped density of states expected for 3D Dirac electrons. These results are fully consistent with the presence of 3D Dirac electrons in Sr_3PbO. The next step is to explore unconventional physics anticipated for the 3D Dirac electrons.

Chiral anomaly has been experimentally explored and expected negative longitudinal MR has been observed in several 3D TDSs. However, current jetting effects, focusing of a current density, raised ongoing discussion about these experiments. We studied the angular dependences of the longitudinal MR and the planar Hall effect in the Sr_3PbO antiperovskite. The intrinsic contribution associated with the chiral anomaly may be captured by the negative longitudinal MR and the planar Hall effect at low magnetic field $B \sim 0.5$ T. The angular dependences at high field $B > 0.5$ T indicate the predominant effect of the current jetting rather than the chiral anomaly. The detailed experiments will be left for future study to extract

clear conclusion.

In Dirac semimetals, the topology of an inter-band mixing, represented by inter-band Berry connection, can give rise to a giant orbital diamagnetism which strongly depends on the chemical potential and temperature. The large diamagnetism has been observed, for example, in the bulk magnetic susceptibility of Bi. However, the orbital origin of the large diamagnetism has not been experimentally confirmed owing to the presence of other contributions to the magnetic susceptibility associated with the complicated Fermi surface of Bi. We report the bulk magnetic susceptibility and the ^{207}Pb NMR experiments on Sr_3PbO antiperovskite samples with different carrier density from $\sim 10^{18}$ to $\sim 10^{20}$ cm^{-3}. The magnitude of T_1^{-1} is well scaled by a density of states derived from a band calculation. This enables us to separate spin and orbital contributions of NMR Knight shift by analyzing K, T_1^{-1} and χ with the help of a Korringa relation, which provides the evidence for the presence of the giant orbital diamagnetism in Sr_3PbO.

Contents

Chapter 1
Background

1.1. Dirac electron

1.1.1. Dirac equation in high energy physics

In 1928, P.A.M. Dirac proposed the Dirac equation [1] which describes relativistic spin 1/2 fermions such as an electron. Dirac equation can be written by

$$i\hbar\frac{\partial}{\partial t}\psi = \hat{H}\psi = \left(c\boldsymbol{\alpha}\cdot\boldsymbol{p} + mc^2\beta\right)\psi \tag{1.1}$$

where c, m, $\boldsymbol{p}$ are the speed of light, mass, momentum. Here, $\boldsymbol{\alpha}$ and β are 4×4 matrices which satisfy

$$\left\{\alpha^i,\alpha^j\right\} = 2\delta^{ij}, \ \left\{\alpha^i,\beta\right\} = 0, \ \beta^2 = 1. \tag{1.2}$$

In the Dirac representation, these matrices are explicitly written by

$$\alpha^i = \tau_x \otimes \sigma_i = \begin{pmatrix} 0 & \sigma_i \\ \sigma_i & 0 \end{pmatrix}, \ \beta = \tau_z \otimes I = \begin{pmatrix} I & 0 \\ 0 & -I \end{pmatrix} \tag{1.3}$$

and Dirac Hamiltonian becomes

$$H = \begin{pmatrix} mc^2 & ic\boldsymbol{p}\cdot\boldsymbol{\sigma} \\ ic\boldsymbol{p}\cdot\boldsymbol{\sigma} & -mc^2 \end{pmatrix} \tag{1.4}$$

where σ_i and I are Pauli matrix and identity matrix, respectively. A wave function ψ has four components which represent two spin states (up and down) and two kinds of particles (particle and antiparticle). The energy dispersion can be obtained by solving

$$\hat{H}\psi = E\psi, \tag{1.5}$$

which yields linear energy dispersion, $E = \pm\sqrt{mc^2 + (cp)^2}$, as shown in Fig. 1.1. This contrasts to the Schrödinger equation with quadratic energy dispersion, $E = p^2/2m$. The energy gap
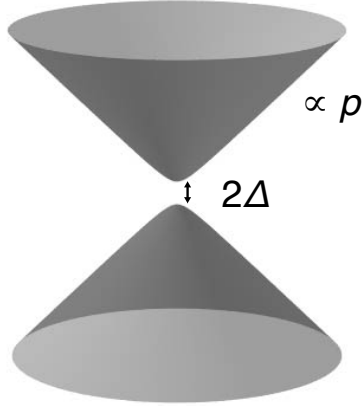
Fig. 1.1. Linear energy dispersion of Dirac electron with mass gap Δ.

$\Delta = 2mc^2$ corresponds to the energy for pair creation of two particles, for example, a electron and a positron. mc^2 is equal to the energy of the mass m, and thus $\Delta = mc^2$ is called (Dirac) mass gap. Considering the low energy limit $p \sim 0$, the energy dispersion becomes

$$E = \Delta\left(1 + \left(\tfrac{cp}{\Delta}\right)^2\right)^{1/2} \sim \Delta + \frac{p^2}{2m} + O\left(k^4\right) \tag{1.6}$$

which reproduces the quadratic dispersion of the Schrödinger equation if we neglect a constant offset Δ and higher order terms $O(k^4)$.

1.1.2. Chirality

In 3D Dirac electron system, a concept of chirality is important. Using the Weyl representation

$$\beta = \begin{pmatrix} 0 & I \\ I & 0 \end{pmatrix}, \ \alpha^i = \begin{pmatrix} -\sigma_i & 0 \\ 0 & \sigma_i \end{pmatrix}, \tag{1.7}$$

the Dirac equation can be written by

$$i\hbar\frac{\partial}{\partial t}\psi = \begin{pmatrix} -ic\boldsymbol{p}\cdot\boldsymbol{\sigma} & mc^2 \\ mc^2 & ic\boldsymbol{p}\cdot\boldsymbol{\sigma} \end{pmatrix}\psi \tag{1.8}$$

When $m = 0$, Eq.1.8 can be decomposed into 2×2 Weyl equation as

$$i\hbar\frac{\partial}{\partial t}\psi_{\mathrm{R/L}} = \pm ic\boldsymbol{p}\cdot\boldsymbol{\sigma}\psi_{\mathrm{R/L}} \tag{1.9}$$

$$\psi = \begin{pmatrix} \psi_{\mathrm{L}} \\ \psi_{\mathrm{R}} \end{pmatrix} \tag{1.10}$$

where $\psi_{\mathrm{R/L}}$ is called Weyl spinor. Chirality χ for $\psi_{\mathrm{R/L}}$ is defined as $\chi = +1/-1$. In the massless Dirac equation, chirality corresponds to helicity which takes $+1$ (-1) when $\boldsymbol{p}$ is parallel (anti-parallel) to $\boldsymbol{\sigma}$. Since $\psi_{\mathrm{R/L}}$ are independent solutions of the Weyl equations in Eq.1.8, chirality is a good quantum number for massless Dirac fermions. Chiralities $\chi = \pm 1$ are hybridized in the massive Dirac equation with $\Delta \neq 0$. However, chirality can be approximately a valid quantum number when Δ is sufficiently small.

1.1.3. Dirac electron in condensed matter

In condensed matter physics, low energy excitation with much smaller energy than mc^2 is important. According to Eq.1.6, this indicates electrons in solids can be basically described by the non-relativistic Schrödinger equation with the quadratic energy dispersion. A relativistic effect is usually taken into account as a perturbation by spin-orbit coupling. However, the relativistic Dirac Hamiltonian can be realized as a low energy effective Hamiltonian in some material where a band crossing is protected against gap formation and gives rise to a linear energy dispersion.

The most famous example of the realization of such Dirac electrons is graphene [2, 3], a single layer of hexagonal lattice of carbon atoms, which hosts two-dimensional (2D) Dirac electrons. Another important class of materials with 2D Dirac electrons is a topological insulator (TI) [4, 5]. TI is insulating in the bulk but has gapless surface states with linear dispersion protected by time reversal symmetry [6–10]. Topological crystalline insulator (TCI) [11] also hosts gapless surface states protected by a crystalline symmetry. The presence of nontrivial surface states in TI and TCI is attributed to the nontrivial topology of their bulk band structures where topological invariants such as Z_2 index or mirror Chern number take nontrivial values. The low energy effective Hamiltonian in these 2D Dirac materials are given by

$$H = \hbar v_F \boldsymbol{k} \cdot \boldsymbol{\sigma} \tag{1.11}$$

where v_F, $\boldsymbol{k}$ are Fermi velocity and wave vector, respectively. Here, Pauli matrix $\boldsymbol{\sigma}$ corresponds to the sublattice degree of freedom in grapehen and that of real spin in TI respectively. In addition to Eq.1.11, the two distinct Dirac cones at K and K' points in the first Brillouine zone (BZ) of graphene yields valley degree of freedom. These 2D Dirac materials have been attracting considerable interest because of their unconventional properties such as the half-integer quantum Hall effect, which was observed in graphene [2, 3], and the anomalous quantum Hall effect in a magnetic TI [12, 13].

3D topological Dirac semimetal (TDS) [14–16], a 3D analogue of graphene, has 3D linear

dispersion in bulk where crystalline symmetry protects the band crossing. Na_3Bi is theoretically proposed as a candidate for 3D TDS [15] and experimentally confirmed by angle resolved photoemission spectroscopy (ARPES) measurements [17, 18]. After the first realization of the 3D TDS phase in Na_3Bi, several 3D TDSs such as Cd_3As_2 [16, 19–30], TlBiSSe [31] and $ZrTe_5$ [32–34] were discovered. 4×4 matrix elements of 3D Dirac Hamiltonian can be explicitly written by

$$
\begin{array}{cc}
|\text{conduction}\rangle & |\text{valence}\rangle
\end{array}
$$
$$
H = \begin{pmatrix} \Delta & i\hbar v_F \, \boldsymbol{k} \cdot \boldsymbol{\sigma} \\ i\hbar v_F \, \boldsymbol{k} \cdot \boldsymbol{\sigma} & -\Delta \end{pmatrix}
$$
$$
= \begin{pmatrix} \Delta & 0 & i\hbar v_F \, k_z & i\hbar v_F \, k_+ \\ 0 & \Delta & i\hbar v_F \, k_- & -i\hbar v_F \, k_z \\ i\hbar v_F \, k_z & i\hbar v_F \, k_+ & -\Delta & 0 \\ i\hbar v_F \, k_- & -i\hbar v_F \, k_z & 0 & -\Delta \end{pmatrix}
$$

or

$$
\begin{array}{cc}
|\chi=+1\rangle & |\chi=-1\rangle
\end{array}
$$
$$
H = \begin{pmatrix} i\hbar v_F \, \boldsymbol{k} \cdot \boldsymbol{\sigma} & \Delta \\ \Delta & -i\hbar v_F \, \boldsymbol{k} \cdot \boldsymbol{\sigma} \end{pmatrix}
$$
$$
= \begin{pmatrix} i\hbar v_F \, k_z & i\hbar v_F \, k_+ & \Delta & 0 \\ i\hbar v_F \, k_- & -i\hbar v_F \, k_z & 0 & \Delta \\ \Delta & 0 & -i\hbar v_F \, k_z & -i\hbar v_F \, k_+ \\ 0 & \Delta & -i\hbar v_F \, k_- & i\hbar v_F \, k_z \end{pmatrix}
$$

where $k_\pm = k_x \pm i k_y$. $|\text{conduction}\rangle$, $|\text{valence}\rangle$ and $|\chi = \pm 1\rangle$ indicate bases for matrix elements. 3D Dirac bands in 3D TDS are spin degenerate due to the combination of time reversal and inversion symmetries.

1.2. Origin of Dirac electrons

Band repulsion usually gives rise to an avoided crossing which can be explained by the Schrödinger equation in terms of effective mass approximation. However, linear dispersion can be realized by a band crossing in some materials. In this section, an origin of the band crossing is discussed based on previous theoretical works [14–16, 35–37].

1.2.1. Time reversal and inversion symmetry

Let us discuss transformation of a $|\boldsymbol{k}, \sigma\rangle$ state under time reversal and space inversion operation. The time reversal operation inverts the signs of both momentum $\boldsymbol{k}$ and spin σ as $|\boldsymbol{k}, \sigma\rangle \rightarrow$
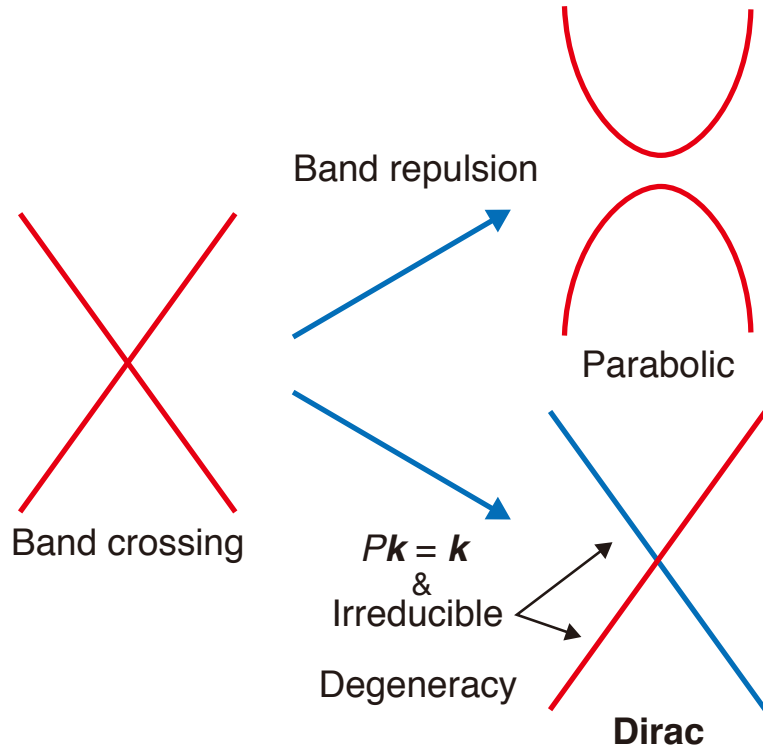
Fig. 1.2. Band repulsion usually gives rise to an avoided crossing and parabolic bands. When wave vector k is invariant under an operator of symmetry, P, a band crossing between different irreducible representations can be protected agains gap formation. This can realize linear dispersion, leading to Dirac bands.

$|-\boldsymbol{k}, -\sigma\rangle$. The space inversion operation also inverts the sign of the momentum, but it does not flip the spin as $|\boldsymbol{k}, \sigma\rangle \to |-\boldsymbol{k}, \sigma\rangle$. When the system preserves both time reversal and inversion symmetries, $|\boldsymbol{k}, \uparrow\rangle \to |\boldsymbol{k}, \downarrow\rangle$ holds by combining these operations. This indicates the system with both time reversal and inversion symmetries is spin degenerate.

1.2.2. Band degeneracy protected by symmetry

Let us consider system which preserves certain symmetry. An operator of the symmetry P and the Bolch Hamiltonian $H(\boldsymbol{k})$ satisfies

$$PH(\boldsymbol{k})P^{-1} = H(P\boldsymbol{k}). \tag{1.12}$$

When $\boldsymbol{k}$ is invariant under the operator P as $P\boldsymbol{k} = \boldsymbol{k}$, the above relation becomes commutation relation $\big[H(\boldsymbol{k}), \boldsymbol{P}\big] = 0$. $H(\boldsymbol{k})$ can be block diagonalized by eigenvalue of P, λ_i, as

$$H(\boldsymbol{k}) = \begin{pmatrix} \text{eigenvalue } \lambda_1 & 0 & \cdots & 0 \\ 0 & \text{eigenvalue } \lambda_2 & & \vdots \\ \vdots & & \ddots & 0 \\ 0 & \cdots & 0 & \text{eigenvalue } \lambda_n \end{pmatrix} \qquad (1.13)$$

where each block matrix corresponds to an irreducible representation of P. The states from different irreducible representations have no off-diagonal elements, and therefore they are not hybridized. When two bands from different irreducible representations form a band crossing at invariant $\boldsymbol{k}$ under P, the band degeneracy point is protected against gap formation (Fig. 1.2). The energy dispersion around the band touching point k_0 can be expanded as

$$E = \text{const.} + \hbar v_F \left(k - k_0 \right) + O\!\left((k - k_0)^2 \right) \qquad (1.14)$$

which gives linear energy dispersion if $k - k_0$ is sufficiently small.

A band crossing protected by rotational symmetry is a typical example of 3D TDS. Let us consider system with n-fold symmetry. A rotation operator $\mathrm{C_n}$ satisfies $\mathrm{C_n}\boldsymbol{k} = \boldsymbol{k}$ on the rotational axis where $H(k)$ and $\mathrm{C_n}$ are commutative. As discussed above, $\mathrm{C_n}$ protects the band crossing between the bands with different eigenvalues of $\mathrm{C_n}$. Typical 3D TDSs, for example Na_3Bi, Cd_3As_2 and antiperovskites, realize linear dispersion by rotational symmetry [15, 16, 35, 36]. For example, the band crossing by Na $3s$ and Bi $6p$ orbitals gives rise to Dirac bands in Na_3Bi [15] as shown in Fig. 1.3. The Dirac Hamiltonian can be expressed as below.

$$\begin{array}{cccc} \left|s,\uparrow\right\rangle & \left|p,\uparrow\right\rangle & \left|p,\downarrow\right\rangle & \left|s,\downarrow\right\rangle \end{array}$$

$$H = \begin{pmatrix} i\hbar v_F k_z & i\hbar v_F k_+ & 0 & 0 \\ i\hbar v_F k_- & -i\hbar v_F k_z & 0 & 0 \\ 0 & 0 & -i\hbar v_F k_z & -i\hbar v_F k_+ \\ 0 & 0 & -i\hbar v_F k_- & i\hbar v_F k_z \end{pmatrix} \qquad (1.15)$$

Here, $\boldsymbol{\sigma}$ in the Weyl representation Eq.1.8 is pseudospin which represents orbital degree of freedom (s and p orbitals). Spin up or down components reside in chirality $\chi = +1$ or $\chi = -1$ states, respectively. The chirality degree of freedom corresponds to the spin degree of freedom. Since the spin up and down states are degenerate at zero magnetic field, the $\chi = \pm 1$ states are also degenerate. The chirality ± 1 states are split in magnetic field due to Zeeman split, which may realize chiral anomaly in 3D TDS, as will be discussed in 1.4.8.
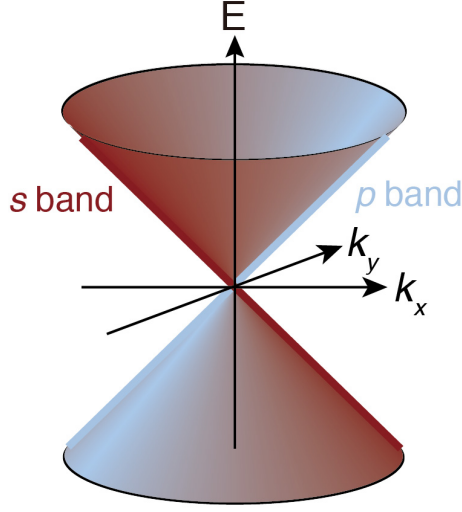
Fig. 1.3. 3D Dirac electrons in Na_3Bi are formed by the band crossing between s and p bands.

1.3. Dirac and topological materials

1.3.1. Dirac semimetal

In contrast to high energy physics, Dirac Hamiltonian in condensed matter physics is realized as a low energy effective Hamiltonian. This means the linear energy dispersion $E(\boldsymbol{k}) = \sqrt{\Delta^2 + (\hbar v_F k)^2}$ can take several variations. For example, Fig. 1.4 (a-c) shows massless, massive and anisotropic Dirac cones, respectively. The energy dispersion of the anisotropic Dirac electrons is written by

$$E(\boldsymbol{k}) = \sqrt{\Delta^2 + \left(\hbar v_x k_x\right)^2 + \left(\hbar v_y k_y\right)^2 + \left(\hbar v_z k_z\right)^2} \tag{1.16}$$

with anisotropic Fermi velocities v_i ($i = x, y, z$). In addition, 3D TDS can be driven into topologically distinct phases by breaking symmetries or controlling parameters such as magnetism. In the following sections, several topological materials related to 3D TDS are introduced.

1.3.2. Weyl semimetal

A Weyl semimetallic phase can be derived from 3D TDS by breaking time reversal or inversion symmetry [38–41]. Weyl semimetals possess spin split Weyl points each of which acts as source or sink of Berry curvature with chirality $\pm$ 1. One of the intriguing features of Weyl semimetal is the presence of Fermi arc surface states [38] which connect the projection points of Weyl nodes with opposite chiralities. TaAs and its family materials [42–47] are confirmed to be a Weyl semimetal with inversion symmetry breaking. Several candidates for magnetic
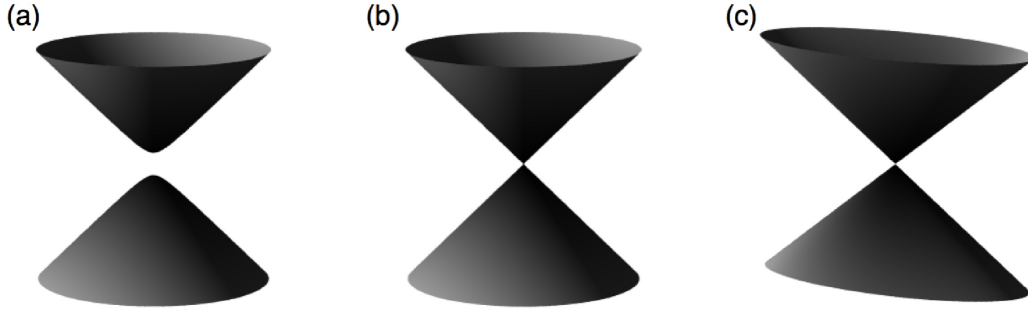
Fig. 1.4. Variation of Dirac cones. (a) Massive Dirac cone. (b) Massless Dirac cone. (c) Anisotropic Dirac cone.

Weyl semimetal, where time reversal symmetry is broken, such as $Mn_3(Sn/Ge)$ [48–50] and $Co_3Sn_2S_2$ [51, 52] have been reported.

1.3.3. Type II Dirac/Weyl semimetal

Electron bands with tilted Dirac cones can be realized in condensed matter as seen in Fig. 1.5. With a large enough tilt, the conduction and the valence bands of a Dirac cone disperse across the Fermi energy, where electron and hole naturally coexist as shown in Fig. 1.5 (c). Dirac/ Weyl semimetals with such tilted Dirac cones are called type-II Dirac/Weyl semimetal [53]. Although the Dirac equation Eq.1.4 is originally invariant under a Lorentz transformation, type-II Dirac/Weyl cone violates the Lorentz invariance. The type II Dirac/Weyl semimetal phase is discussed in, for example, WTe_2 [53, 54], $MoTe_2$ [55–57].

1.3.4. Line node semimetal

In Dirac/Weyl semimetals, the conduction and the valence bands touch at discrete Dirac/ Weyl nodes. When a certain plane in k space is invariant under a symmetry operator P, band crossing between different irreducible representations of P does not open a gap on the plane. This can result in a band touching along closed lines [58] instead of discrete points for Dirac/ Weyl semimetals. Topological semimetals with the line nodes are called nodal line semimetal or line node semimetal. Several materials such as $(Ca/Sr)IrO_3$ [59–64], $(Zr/Hf)SiS$ [65–68] and $CaAg(As/P)$ [69, 70] were proposed as candidates for the line node semimetal.

1.4. Property of Dirac electron

1.4.1. Number and Density of states

Linear energy dispersion of Dirac electrons has unconventional energy dependence of number
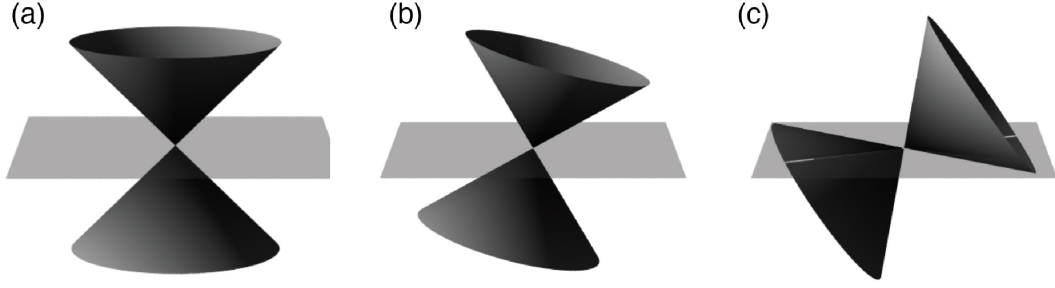
Fig. 1.5. Tilted Dirac cones. (a) A Dirac cone without tilt. (b) A Dirac cone with small tilt. (c) A Dirac cone with large tilt. This is called type-II Dirac/Weyl fermion where electron and hole coexist.

and density of states (DOS). Carrier density n for 3D free electron gas is given by

$$n = g_s \frac{1}{(2\pi)^3} \frac{4\pi}{3} k_F^3 = \frac{g_s k_F^3}{6\pi}. \tag{1.17}$$

Here, g_s and k_F are spin degeneracy and Fermi wave vector respectively. Applying linear or quadratic energy dispersions of

$$E = \begin{cases} \sqrt{\Delta^2 + (\hbar v_F k)^2} & \text{(Dirac)} \\ \dfrac{\hbar^2 k^2}{2m} & \text{(Quadratic)} \end{cases} \tag{1.18}$$

to the above carrier density n, n can be written by

$$n = \begin{cases} \dfrac{g_s}{6\pi^2} \left(\dfrac{E^2 - \Delta^2}{\hbar^2 v_F^2} \right)^{\frac{3}{2}} & \text{(Dirac)} \\ \dfrac{g_s}{6\pi^2} \left(\dfrac{2mE}{\hbar^2} \right)^{\frac{3}{2}} & \text{(Quadratic)} \end{cases} \tag{1.19}$$

respectively. DOS, $D(E)$, can be calculated as below.

$$D(E) = \frac{dn}{dE} = \begin{cases} \dfrac{g_s}{2\pi^2 \hbar^3 v_F^3} |E| \sqrt{E^2 - \Delta^2} & \text{(Dirac)} \\ \dfrac{g_s}{4\pi^2} \left(\dfrac{2m}{\hbar^2} \right)^{\frac{3}{2}} \sqrt{E} & \text{(Quadratic)} \end{cases} \tag{1.20}$$

The DOS of 3D Dirac electrons are proportional to $\sim E^2$ unlike $\sqrt{E}$ for the quadratic disper-

sion. The unconventional energy dependence of the DOS can be reflected in, for example, temperature dependence of nuclear magnetic resonance (NMR) spin lattice relaxation rate T_1^{-1} [71–73] which is proportional to thermal averaged $D(E)^2$, as will be discussed in 1.4.11.

1.4.2. Light effective mass & High mobility

Dirac semimetals have high mobility carriers with extremely light cyclotron effective mass. The cyclotron effective mass m_c^* is defined by

$$m_c^* = \frac{\hbar^2}{2\pi}\frac{\partial S_k}{\partial E}\bigg|_{E=E_F} \tag{1.21}$$

where S_k is a cross section of Fermi surface (FS) normal to magnetic field. Assuming Fermi sphere, $S_k = \pi k^2$, Eq.1.21 gives constant effective mass m_c^* for quadratic energy dispersion of $E = \hbar^2 k^2/2m_c^*$. Cyclotron effective mass m_c^* of Dirac electrons with linear energy dispersion $E = \sqrt{\Delta^2 + (\hbar v_F k)^2}$ can be calculated as

$$\begin{aligned} m_c^* &= \frac{\hbar^2}{2\pi}\frac{\partial}{\partial E}\left(\pi\frac{E^2-\Delta^2}{\hbar^2 v_F^2}\right)\bigg|_{E=E_F} = \frac{E_F}{v_F^2} \\ &= \frac{\sqrt{\Delta^2 + (\hbar v_F k_F)^2}}{v_F^2} = \sqrt{m_D^2 + m_{c0}^{*2}} \to m_D \quad (k \to 0) \end{aligned} \tag{1.22}$$

which depends on the Fermi energy E_F. Here, $m_D = \Delta/v_F^2$ and $m_{c0}^* = \hbar k_F/v_F$ are Dirac mass and cyclotron effective mass for massless 3D Dirac electrons, respectively. Extremely light cyclotron effective mass can be realized around the Dirac node as seen in Fig. 1.6. For example, typical parameters for Dirac semimetals, $v_F = 5 \times 10^5$ m/s and $E_F = 30$ meV, yield 2% of free electron mass, $m_c^* \simeq 0.02 m_e$.

High mobility of Dirac electrons is attributed to the light effective mass. Mobility μ is given by

$$\mu = \frac{e\tau}{m_c^*} \tag{1.23}$$

where τ is scattering time. Dirac electrons with light effective mass can realize high mobility $\mu \propto 1/m_c^*$. Compared to a conventional metal with mobility $\mu \sim 10$ cm^2/Vs, 3D TDS shows high mobility of $\mu \sim 10^4$ cm^2/Vs as observed in Cd$_3$As$_2$ [23, 24] and ZrTe$_5$ [34].
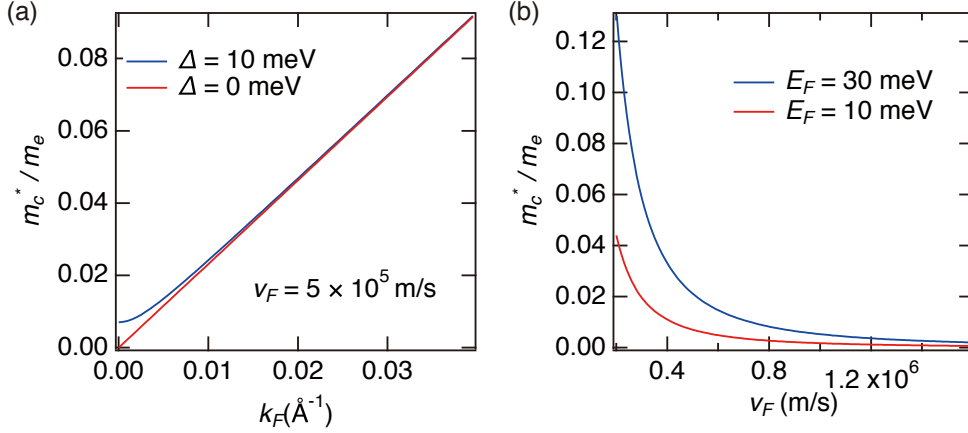
Fig. 1.6. (a) Fermi wave vector k_F dependence of cyclotron effective mass m_c^* for 3D Dirac electrons with Fermi velocity $v_F = 5.0 \times 10^5$ m/s and mass gap $\Delta = 0$ meV (red line) or 10 meV (blue line). (b) v_F dependence of m_c^* for 3D Dirac electrons with Fermi energy $E_F = 10$ meV (red line) or 30 meV (blue line).

1.4.3. Berry phase and Berry curvature

Berry phase and Berry curvature [74, 75] in Dirac/Weyl semimetals give rise to unconventional magnetic responses such as half-integer quantum Hall effect [2, 3] and chiral anomaly [76, 77]. In quantum mechanics, time development of the nth eigenstate $\left|\psi_n\right\rangle$ with the eigenenergy E_n adds a phase factor to the eigenstate as

$$\left|\psi_n(t)\right\rangle = e^{-iE_n t/\hbar}\left|\psi_n(0)\right\rangle. \tag{1.24}$$

When a certain parameter adiabatically changes along a closed loop, the phase factor of the wave function can also acquire a topological term, Berry phase. Let us consider Bloch Hamiltonian $H(\boldsymbol{k})$ with the nth Bloch states $\left|u_n(\boldsymbol{k})\right\rangle$. Since the Bloch states depend on $\boldsymbol{k}$, the variation of $\boldsymbol{k}$ along a closed path C gives rise to Berry phase γ_n as

$$\gamma_n = \oint_C d\boldsymbol{k} \cdot \boldsymbol{A_n}(\boldsymbol{k}) \tag{1.25}$$

where Berry connection $\boldsymbol{A_n}(\boldsymbol{k})$ is given by

$$\boldsymbol{A_n}(\boldsymbol{k}) = i\left\langle u_n(\boldsymbol{k})\middle|\nabla_{\boldsymbol{k}}\middle|u_n(\boldsymbol{k})\right\rangle. \tag{1.26}$$

As seen in Eq.1.26 and Fig. 1.7, the Berry connection can be intuitively regarded as the variation of $\left|u_n(\boldsymbol{k})\right\rangle$ in k space. Note C must be closed in order to preserve gauge invariance of γ_n.
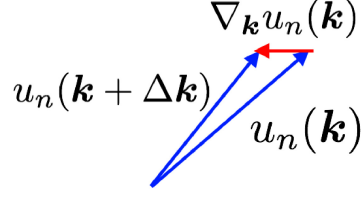
Fig. 1.7. Berry connection can be thought as the variation of the nth Bloch state $\left|u_n(\boldsymbol{k})\right\rangle$ as in Eq.1.26.

Because Dirac electrons are formed by a band crossing between different orbitals, the strong variation of the wave function around the Dirac node yields nontrivial Berry phase. Let us consider cyclotron motion of Dirac electrons in magnetic field along a z direction. A closed path C is a circle on a k_x-k_y plane as $(k\cos\theta, k\sin\theta, 0)$. 3D Dirac Hamiltonian on C can be decomposed into 2×2 matrix as below.

$$H \pm (\boldsymbol{k}) = \begin{pmatrix} \Delta & i\hbar v_F\, ke^{\pm i\theta} \\ i\hbar v_F\, ke^{\mp i\theta} & \Delta \end{pmatrix} \tag{1.27}$$

The eigenvalues are $\pm \sqrt{\Delta^2 + (\hbar v_F k)^2}$. The eigenstate $\left|u_\theta\right\rangle$ for the eigenvalue $\sqrt{\Delta^2 + (\hbar v_F k)^2}$ is given by

$$\left|u_\theta\right\rangle = \frac{1}{\sqrt{2}} \frac{1}{\sqrt{1+\alpha^2 + \sqrt{1+\alpha^2}}} \begin{pmatrix} \sqrt{1+\alpha^2} + 1 \\ \alpha e^{-i\theta} \end{pmatrix} \tag{1.28}$$

where $\alpha = \hbar v_F k/\Delta$. By substituting $\left|u_n(\boldsymbol{k})\right\rangle$ in Eq.1.25 for $\left|u_\theta\right\rangle$, the Berry phase γ is calculated as

$$\gamma = \pi \frac{\alpha^2}{1+\alpha^2 + \sqrt{1+\alpha^2}} \tag{1.29}$$

which depends on Fermi energy E_F and Fermi wave vector k_F. For massless Dirac Hamiltonian with $\Delta = 0$, the Berry phase is obtained by $\alpha \to \infty$ in Eq.1.29, leading to nontrivial Berry phase π independent of E_F and k_F. The nontrivial Berry phase π of Dirac electrons plays an important role in the formation of Landau levels.

According to Stokes's theorem, Berry phase γ_n in Eq.1.25 is also written by

$$\gamma_n = \int_S d\boldsymbol{S} \cdot \boldsymbol{\Omega}_{\boldsymbol{k}}^n \tag{1.30}$$

where S is an arbitrary surface enclosed by the path C. Here, Berry curvature $\boldsymbol{\Omega}_{\boldsymbol{k}}^n(\boldsymbol{k})$ is given

by

$$\boldsymbol{\Omega}_{\boldsymbol{k}}^n(\boldsymbol{k}) = \nabla_{\boldsymbol{k}} \times \boldsymbol{A_n}(\boldsymbol{k}) = i\nabla_{\boldsymbol{k}} \times \left\langle u_n(\boldsymbol{k}) \middle| \nabla_{\boldsymbol{k}} \middle| u_n(\boldsymbol{k}) \right\rangle. \tag{1.31}$$

For example, an explict form of a k_z element of Berry curvature is

$$\boldsymbol{\Omega}_{k_x k_y}^n = i\left(\left\langle \frac{\partial u_n(\boldsymbol{k})}{\partial k_x} \middle| \frac{\partial u_n(\boldsymbol{k})}{\partial k_y} \right\rangle - (x \Leftrightarrow y) \right). \tag{1.32}$$

Let us consider 3D massless Dirac/Weyl Hamiltonian which can be decomposed into two 2×2 matrices $H(\boldsymbol{k}) = \pm\hbar v_F\, \boldsymbol{k} \cdot \boldsymbol{\sigma}$ for chirality ± 1. The Berry curvature can be calculated as

$$\boldsymbol{\Omega}(\boldsymbol{k}) = \pm\frac{1}{2}\frac{\boldsymbol{k}}{k^3} \tag{1.33}$$

which takes the same form as magnetic field generated by a magnetic monopole. This indicates the Dirac cone acts as a monopole of the Berry curvature, in which chirality ± 1 states corresponds to source or sink respectively. Since Dirac cones in 3D TDS are spin degenerate, the source and sink of Berry curvature are canceled out. 3D TDS in the magnetic field or Weyl semimetal have spin split Dirac cones. The separated source and sink form the flow of Berry curvature as shown in Fig. 1.8. Applying Gauss's theorem to Eq.1.30 and Eq.1.33, γ_n can be calculated as

$$\gamma_n = \int_{S^2\big|_{k_z \geq 0}} d\boldsymbol{S} \cdot \boldsymbol{\Omega}(\boldsymbol{k}) = \pm\pi \tag{1.34}$$

which is, of course, the same value as massless case ($\alpha \to \infty$) of Eq.1.29. Here, $S^2\big|_{k_z \geq 0}$ is a semisphere for $k_z \geq 0$.

In addition, Berry curvature acts as pseudo magnetic field in k space. Boltzmann equation with contribution from Berry curvature [75, 77] is written by

$$\begin{cases} \dot{\boldsymbol{r}} = \dfrac{\partial \varepsilon_n(\boldsymbol{k})}{\hbar\, \partial \boldsymbol{k}} + \hbar\boldsymbol{k} \times \boldsymbol{\Omega}^n(\boldsymbol{k}) \\[2mm] \dot{\boldsymbol{k}} = e\boldsymbol{E} + \dfrac{e}{c}\dot{\boldsymbol{r}} \times \boldsymbol{B} \end{cases} \tag{1.35}$$

The velocity $\dot{\boldsymbol{r}}$ has not only a conventional term from band dispersion but also an extra term including Berry curvature, $\hbar\dot{\boldsymbol{k}} \times \boldsymbol{\Omega}^n(\boldsymbol{k})$. This term can be regarded as 'Lorentz force' from pseudo magnetic field $\boldsymbol{\Omega}^n(\boldsymbol{k})$ in k space. Let us consider Eq.1.35 with time reversal symmetry (TRS) or inversion symmetry (IS). $\dot{\boldsymbol{r}}$ and $\boldsymbol{k}$ invert the signs while $\dot{\boldsymbol{k}}$ preserves the sign under
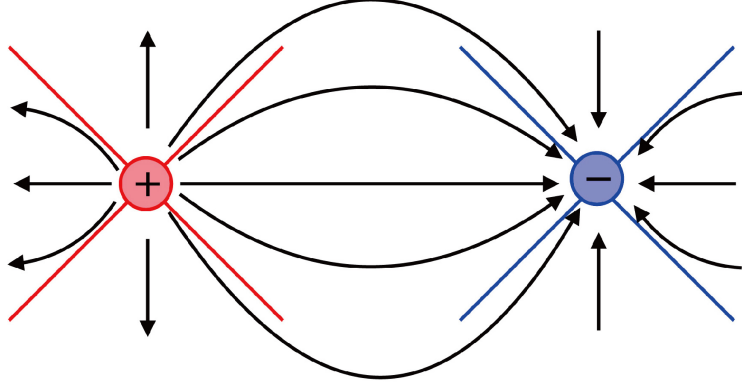
Fig. 1.8. In Weyl semimetal or 3D TDS under magnetic field, Berry curvature flows from the source with chirality $+1$ into the sink with chirality -1.

TRS. IS changes the signs of all $\dot{\boldsymbol{r}}$, $\boldsymbol{k}$ and $\dot{\boldsymbol{k}}$. When system has TRS or IS, Berry curvature $\boldsymbol{\Omega}^n(\boldsymbol{k})$ satisfies the following conditions.

$$
\begin{aligned}
\boldsymbol{\Omega}^n(\boldsymbol{k}) &= -\boldsymbol{\Omega}^n(-\boldsymbol{k}) \qquad \text{(TRS)} \\
\boldsymbol{\Omega}^n(\boldsymbol{k}) &= \boldsymbol{\Omega}^n(-\boldsymbol{k}) \qquad \text{(IS)}
\end{aligned}
\tag{1.36}
$$

Both relations hold in system with both TRS and IS, where $\boldsymbol{\Omega}_n(\boldsymbol{k})$ vanishes in whole the BZ. 3D TDS under magnetic field or Weyl semimetal, where TRS or IS are broken, have finite Berry curvature which can contribute to transport phenomena. For example, Berry curvature plays an important role in anomalous Hall effect [48, 51, 78] and chiral anomaly [76, 77, 79].

1.4.4. Anomalous Landau level splitting

Dirac electron has unconventional Landau level (LL) under magnetic field [80], which is attributed to k-linear dispersion and nontrivial Berry phase π. Magnetic field can be taken into account by substituting $\hbar\boldsymbol{k}$ to $\boldsymbol{\pi} = \hbar\boldsymbol{k} - e\boldsymbol{A}$

$$
H\psi = \begin{pmatrix} \Delta & iv_F\left(\hbar\boldsymbol{k} - e\boldsymbol{A}\right)\cdot\boldsymbol{\sigma} \\ iv_F\left(\hbar\boldsymbol{k} - e\boldsymbol{A}\right)\cdot\boldsymbol{\sigma} & -\Delta \end{pmatrix}\begin{pmatrix}\psi_c \\ \psi_v\end{pmatrix} = E\begin{pmatrix}\psi_c \\ \psi_v\end{pmatrix}
\tag{1.37}
$$

where $\boldsymbol{A}$, E, $\psi_{c(v)}$ are a vector potential, the energy of LL and the wave function for conduction (valence) band, respectively. Applying $(\boldsymbol{\sigma}\cdot\boldsymbol{a})(\boldsymbol{\sigma}\cdot\boldsymbol{b}) = \boldsymbol{a}\cdot\boldsymbol{b} + i\boldsymbol{\sigma}\cdot(\boldsymbol{a}\times\boldsymbol{b})$ and $\boldsymbol{\pi}\times\boldsymbol{\pi} = i\hbar e\boldsymbol{B}$ to the above equation, we obtain

$$
\left(\frac{\boldsymbol{\pi}^2}{2m_c^*} - \frac{\hbar e}{2m_c^*}\boldsymbol{\sigma}\cdot\boldsymbol{B}\right)\psi_{c,v} = \frac{E^2 - \Delta^2}{2\Delta}\psi_{c,v}
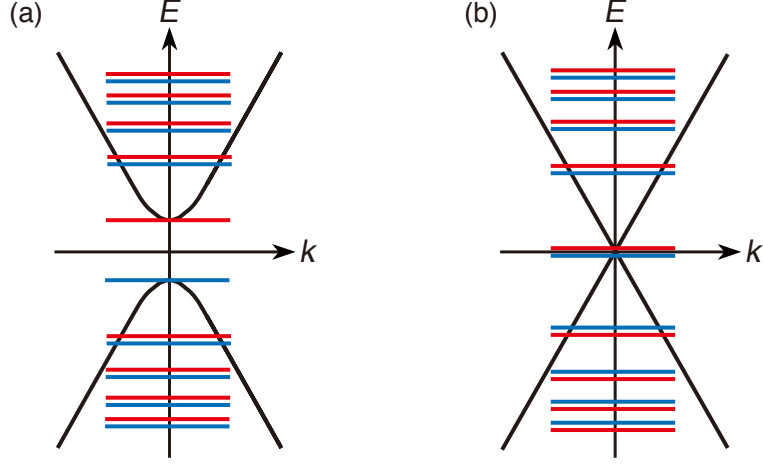\tag{1.38}
$$

Fig. 1.9. (a) and (b) Landau levels for massive and massless 3D Dirac electrons, respectively. The energy of Landau levels are scaled by a square root of the Landau index, which gives rise to the non-equal intervals. The energies of unusual zero modes are fixed at the band edges.

with $m_c^* = \Delta/v_F^2$. The first term of the left side has the same form as free electron gas in magnetic field, which leads to conventional eigenvalues $\hbar\omega_c^*(n + 1/2) + \hbar^2 k_z^2/2m_c^*$ with cyclotron frequency $\omega_c^* = eB/m_c^*$. The energy of LL for Dirac electron becomes

$$
E_{n,\sigma} = \begin{cases} \pm\sqrt{\Delta^2 + 2\Delta\left(\hbar\omega_c^*\left(n + \dfrac{1}{2} + \dfrac{\sigma}{2}\right)\right) + \dfrac{\hbar^2 k_z^2}{2m_c^*}} & (\Delta > 0) \\[4mm] \pm v_F\sqrt{2\hbar eB\left(n + \dfrac{1}{2} + \dfrac{\sigma}{2}\right) + \left(\hbar k_z\right)^2} & (\Delta = 0) \end{cases}
\tag{1.39}
$$

where $n = 0, \pm1, \pm2, \cdots$ and $\sigma = \pm1$ (Fig. 1.9). The energy of the LL in Eq.1.39 is approximately proportional to square root of the field B and the LL index n, which contrasts to conventional LLs for free electron gas $E_n = \hbar\omega_c(n + 1/2)$ linearly proportional to B and n. The energies of LLs in Eq.1.39 are quantized in terms of not half-integer $n + 1/2$ but integer $N = n + 1/2 + \sigma/2$. This offset gives rise to unconventional zero modes for $(n, \sigma) = (0, -1), (-1, 1)$, the energies of which are fixed at the edges of conduction or valence bands. The unconventional LLs of Dirac electrons can be understood by an intuitive picture. Since the energy dispersion of Dirac electrons is proportional to k, square root of conventional k^2, the energy of LL is also scaled by square root of B and n. The additional offset $\sigma/2$ is attributed to the nontrivial Berry phase π of massless Dirac electron in Eq.1.29. Considering contribution from Berry phase, Bohr-Sommerfeld quantum condition acquires an additional term β as

$$\oint \boldsymbol{p} \cdot d\boldsymbol{r} = 2\pi\hbar\left(n + \frac{1}{2} + \beta\right). \tag{1.40}$$

$\beta = 1/2$ for Dirac electrons changes the quantization condition from half-integer to integer. Although Berry phase of massive Dirac electrons deviates from π and depends on the Fermi energy as seen in Eq.1.29, the Fermi energy dependence of the Berry phase and contribution from pseudospin orbital magnetic moment are canceled out [81, 82].

1.4.5. Quantum Oscillation

Landau quantization induces modulation of DOS at Fermi energy, $D(E_F)$, which manifests itself in quantum oscillation. The quantum oscillation is observed in various physical quantities dependent on $D(E_F)$ such as resistivity and magnetic susceptibility. In particular, Shubnikov-de Haas (SdH) oscillation and de Haas-van Alphen effect are the quantum oscillations in resistance and magnetic moment respectively. Similar to Eq.1.40, Onsager's semiclassical quantization condition including contribution from Berry phase becomes

$$S(C) = 2\pi\left(n + \frac{1}{2} - \beta\right)\frac{eB}{\hbar} \tag{1.41}$$

where $S(C)$ is an area enclosed by a cyclotron orbit C. In addition, pseudospin orbital magnetic moment contributes to energy shifts of LLs. In particle-hole symmetric massive Dirac electron system, such contribution is canceled out by Fermi energy dependence of Berry phase. This gives rise to integer quantization of LLs independent of E_F [81, 82]. In general, Dirac Hamiltonian in real system usually violates the particle-hole symmetry due to higher order terms in Eq.1.14, which shifts the Landau level offset from $1/2$.

Since the quantum oscillation is associated with DOS at E_F, it involves a lot of information about FS. $D(E_F)$ takes a maximum when $S(C)$ corresponds to a maximal cross sectional area of the FS S_F normal to the field B. The magnetic field for maximal $D(E_F)$, B_n, is given by the field for the maximal S_F and n in Eq.1.41, yielding

$$\Delta\left(\frac{1}{B}\right) = \frac{1}{B_{n+1}} - \frac{1}{B_n} = \frac{2\pi e}{\hbar S_F}. \tag{1.42}$$

This indicates the quantum oscillation is periodic in $1/B$. The maximal cross section S_F can be experimentally derived from the frequency $F = \Delta(1/B)$. The shape of the FS can be determined by angular dependence of S_F which can be extracted from angular dependence of the quantum oscillations.

The nontrivial Berry phase can be captured by an extra phase offset in the quantum oscil-

lation [74]. The phase offset can be experimentally extracted from a Landau fan diagram by a linear fit of the maxima of the quantum oscillation with

$$n = F/B - 1/2 + \beta \mp 1/8. \tag{1.43}$$

The additional factor $\mp 1/8$ is attributed to three-dimensionality and a maximal/minimal cross-sectional area [83–85]. When n takes integer in Eq.1.43, the DOS is maximum. Therefore, carriers are easily scattered, yielding short scattering time τ. Let us consider the quantum oscillation of conductivity tensors under magnetic field along a z direction. The conductivity tensors are given by

$$\sigma_{xx} = \frac{1}{1 + \left(\omega_c^* \tau\right)^2} \sigma_0 \left(= \sigma_{yy}\right) \tag{1.44}$$

$$\sigma_{xy} = \frac{-\omega_c^* \tau}{1 + \left(\omega_c^* \tau\right)^2} \sigma_0 \left(= -\sigma_{yx}\right) \tag{1.45}$$

with $\sigma_0 = ne^2\tau/m_c^*$. Here, n and m_c^* are carrier density and cyclotron effective mass. The quantum oscillations are usually observed in the strong field limit, $\omega_c^* \tau \gg 1$, where the conductivity σ_{xx} is inversely proportional to τ. The maxima of σ_{xx} for short τ are assigned to the integer n in the Landau fan diagram Eq.1.43.

However, we should be careful about the assignment of LL index as discussed in [86, 87], because what we measured in experiments is not conductivity but resistivity. The resistivity tensor is inverse tensor of conductivity. The transformation for isotropic system is given by

$$\begin{pmatrix} \rho_{xx} & \rho_{xy} \\ \rho_{yx} & \rho_{xx} \end{pmatrix} = \frac{1}{\sigma_{xx}^2 + \sigma_{xy}^2} \begin{pmatrix} \sigma_{xx} & -\sigma_{xy} \\ \sigma_{xy} & \sigma_{xx} \end{pmatrix}. \tag{1.46}$$

When $\sigma_{xx} \ll \left|\sigma_{xy}\right|$ holds, the maxima of $\rho_{xx} \simeq \sigma_{xx}/\sigma_{xy}^2$ corresponds to maxima of σ_{xx}. On the other hand, when $\sigma_{xx} \gg \left|\sigma_{xy}\right|$ is satisfied, the minima of $\rho_{xx} \simeq 1/\sigma_{xx}$ is assigned to the maxima of σ_{xx}. The resistivity along the field direction, ρ_{zz} does not have contribution from Lorentz force. This means that ρ_{zz} does not couple with x or y components and is obtained by the Drude formula as

$$\rho_{zz} = \frac{1}{\sigma_{zz}} = \frac{m_c^*}{ne^2\tau} \tag{1.47}$$

which is inversely proportional to τ. The maxima of ρ_{zz} give the integer n in Eq.1.43.

In addition, the cyclotron effective mass can be derived from temperature dependence of
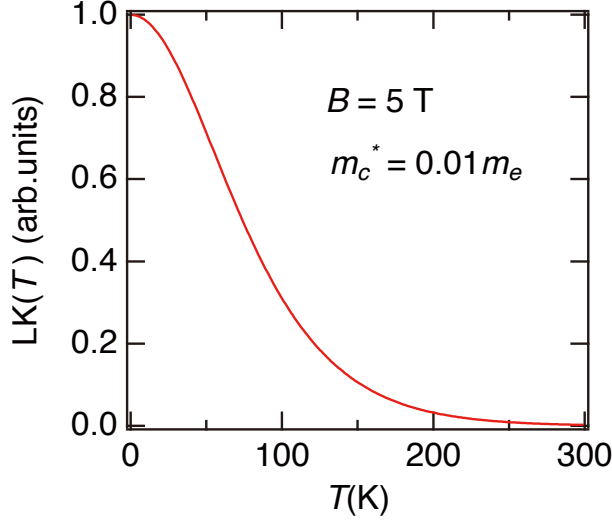
Fig. 1.10. Temperature dependence of LK formula in Eq.1.48 for magnetic field $B = 5$ T and cyclotron effective mass $m_c^* = 0.01m_e$.

the amplitude of the quantum oscillation. The amplitude diminishes with increasing temperature due to broadening of the LLs $\sim k_B T$ and finally fades out when the intervals of LLs are comparable to the thermal fluctuation, $\hbar\omega_c^* \sim k_B T$. According to Lifshitz-Kosevitch (LK) formula [88], the temperature dependence of the amplitude is wrriten by

$$LK(X,T) = \frac{XT}{\sinh(XT)} \quad \left(X = \frac{2\pi^2 k_B m_c^*}{\hbar e B}\right). \tag{1.48}$$

The cyclotron effective mass m_c^* can be experimentally determined by the LK formula fitting to the temperature dependence of the amplitude. The quantum oscillations are observed under the condition $\hbar\omega_c^* \gg k_B T$ which requires high magnetic field and low temperature. For example, in a simple metal with $m_c^* \sim m_e$, the SdH oscillation at 5 T can be observed only below several hundreds mK. In Dirac electron system with extremely light effective mass about 1% of free electron, however, the SdH oscillation at 5 T may be observed at relatively high temperature ~ 100 K and all amplitude of the oscillations can be obtained at 2 K (Fig. 1.10).

1.4.6. Quantum limit

In strong magnetic field, all carriers reside in the lowest LL, which is called quantum limit. In a usual metal with high carrier density $\sim 10^{22}$ cm^{-3}, ~ 500 T is necessary for the quantum limit, which is difficult to reach in experiments. In contrast, the quantum limit can be realized at feasible magnetic field in low carrier density system. Dirac electron system, where the Dirac point or the Dirac mass gap are located at the Fermi energy, is a (zero gap) semiconductor.

Samples synthesized in experiments are slightly doped due to defects or impurities and Fermi energy E_F deviates from zero. When the carrier density and hence Fermi energy E_F are low enough, the quantum limit can be achieved at a moderate magnetic field. For example, the energy gap between the zero mode and $N = n + 1/2 + \sigma/2 = \pm 1$ modes $\Delta_{0\to1}$ for Dirac electrons with Fermi velocity $v_F = 10^6$ m/s and $B = 5$ T is calculated as

$$\Delta_{0\to1} = v_F\sqrt{2\hbar eB} \sim 80\text{meV}. \tag{1.49}$$

Here, the presence of mass gap and the dispersion parallel to B are neglected for simplicity. Fermi energy E_F for $n \sim 10^{18}$ cm^{-3} is typically tens of meV which is comparable to or even smaller than $\Delta_{0\to1}$. For example, $E_F \sim 50$ meV is realized in Sr$_3$PbO with $n \sim 10^{18}$ cm^{-3}. Because the quantum limit can be accessed at a moderate magnetic field of a few T, 3D TDS provides a promising platform to explore unconventional magnetic responses such as giant linear MR [89] and chiral anomaly [76, 77, 79].

1.4.7. Linear MR

3D TDS often shows a large and non-saturating B-linear magnetoresistance (MR) typically over 1000% [22–27, 31, 89], which is distinct from the B^2-MR with saturation in a simple metal. Giant linear MR is widely observed for several 3D TDSs and can be regarded as one of the hallmarks of Dirac electrons. Two models are proposed to understand the unconventional linear MR, but its origin is still controversial. One is a quantum MR of linear dispersion [89] which is satisfied in 3D TDS under the quantum limit. In this scenario, the magnitude of linear MR is expected to be independent of temperature, which is consistent with the experimental observations of 3D TDSs [22, 90]. Linear MR, on the other hand, can be often recognized below the field which the quantum limit requires [22–24].

The other is classical disorder model discussed in doped silver chalcogenides [91–93], Cd$_3$As$_2$ [24] and GaAs quantum wells [94]. In this model, current inhomogeneity is induced by a mobility fluctuation due to the disorder, where the carriers can flow along a direction perpendicular to both current and magnetic field. MR picks up B-linear contribution from B-linear ρ_{xy}. Since the mobility usually depends on temperature, the linear MR is expected to depend on temperature.

1.4.8. Chiral anomaly

Historically, chiral anomaly was first discussed in the context of high energy physics [95, 96]. Chiral anomaly gives a leading contribution to pion decay $\pi^0 \to \gamma\gamma$ [97]. Neelsen and Ninomiya pointed out that chiral anomaly may be also anticipated in a crystal with 3D linear dispersion in the quantum limit [76]. Recently discovered 3D Dirac/Weyl semimetal provides a promising arena to explore the chiral anomaly in condensed matter physics.
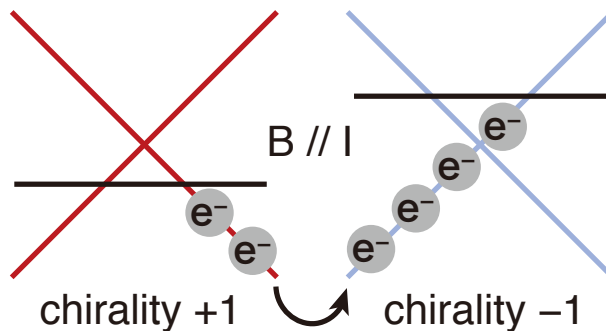
Fig. 1.11. In the presence of magnetic field parallel to the applied current, Berry curvature drives charge pump from the Dirac cone of chirality $+1$ to that of chirality -1.

In Weyl semimetal or Dirac semimetal under magnetic field, source and sink of Berry curvature with chirality ± 1 are separated in k space, forming flow of Berry curvature as shown in Fig. 1.8. Berry curvature contributes to Boltzmann equation of Eq.1.35. When magnetic field parallel to current is applied, contribution from Berry curvature, $(\boldsymbol{E} \cdot \boldsymbol{B})\boldsymbol{\Omega_k}$, drives charge pump from a chirality $+1$ band to a chirality -1 band (Fig. 1.11), which leads to an imbalance of the chirality called chiral anomaly [76, 77, 79]. The charge pump induces additional current which can be observed as negative longitudinal MR. According to theoretical calculations [77, 79], the longitudinal magnetoconductivity is predicted to be proportional to B^2 at low fields.

Chiral anomaly has been experimentally explored and negative longitudinal MR has been reported in several 3D Dirac/Weyl semimetals or related topological materials such as Na_3Bi [98], Cd_3As_2 [28, 29], $ZrTe_5$ [33], TaAs family [99–101] and GdPtBi [102]. However, the interpretation of the negative MR based on the chiral anomaly has been a subject of debate as the possibility of current jetting effects [103–105] cannot be excluded. When a sample has no anisotropy of resistivity, current flows homogeneously through the sample (Fig. 1.12 (a)). 3D Dirac/Weyl semimetals often show giant and non-saturating transverse MR as discussed above, which induces large anisotropy of resistivity under the magnetic field B. If B is applied parallel to the current, the current flows predominantly along the field direction with much smaller resistance. With increasing the anisotropy of resistivity under B, such focusing of the current density between current contacts may lead to substantially zero voltage between the two voltage contacts and hence zero resistance (Fig. 1.12 (b)). This is called current jetting effect, which proposed an alternative scenario for negative MR. To confirm chiral anomaly, we should take special care. One possible way is a cross-check between many independent voltage pairs [102].

Another approach to study chiral anomaly is angular dependent MR experiments. The charge pump term $(\boldsymbol{E} \cdot \boldsymbol{B})\boldsymbol{\Omega_k}$ can contribute to not only negative longitudinal MR but also planar Hall effect [106, 107]. In usual Hall effect, when the magnetic field B normal to the
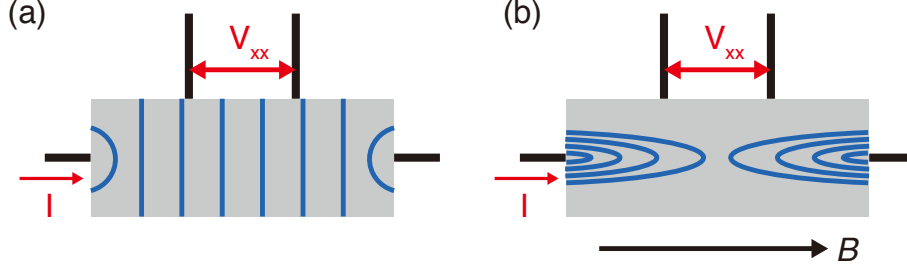
Fig. 1.12. Schematic pictures of equi-potential surface (blue lines) in samples without or with anisotropy of MR. (a) When a sample has no anisotropy of MR, correct resistivity can be obtained by almost homogeneous current. (b) In 3D Dirac/Weyl semimetals, the magnetic field B can induce strong anisotropy of MR, which gives rise to focusing of the current density between the current contacts. The voltage V_{xx} can be almost zero due to the absence of the current near the voltage pairs.
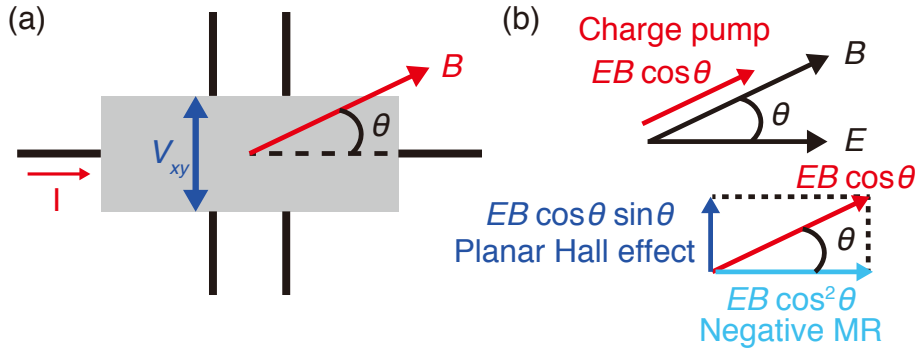

Fig. 1.13. (a) Planar Hall effect induces voltage normal to current I. The induced voltage V_{xy}, magnetic field B and I are in the same plane unlike usual Hall effect. (b) Negative longitudinal MR and planar Hall effect can be regarded as a projection of charge pump.

current I is applied, the Lorentz force induces Hall voltage V_H perpendicular to both I and B. In planar Hall effect, a voltage V_{xy} is induced normal to the applied current I similar to Hall voltage but not perpendicular to B. B is applied in the same plane as I and V_{xy} unlike usual Hall effect as seen in Fig. 1.13 (a). Magnetic field angle dependence of negative longitudinal MR and planar Hall effect are given by

$$\sigma_{xx} \propto \cos^2\theta \tag{1.50}$$

$$\sigma_{xy} \propto \cos\theta\sin\theta \tag{1.51}$$

where θ is defined as in Fig. 1.13 (a). σ_{xx} and σ_{xy} with phase difference can be a useful tool

to distinguish intrinsic contributions from artifacts by the current jetting effect. These angle dependences can be intuitively understood as a projection of the charge pumping effect. The charge pump term is proportional to $\boldsymbol{E} \cdot \boldsymbol{B} = EB\cos\theta$. Negative longitudinal MR or planar Hall effect corresponds to x or y components of the charge pump, yielding the angle dependences of Eq.1.50 or Eq.1.51, respectively (Fig. 1.13 (b)). As the planar Hall effect originates from the charge pump, the same origin as longitudinal MR, planar Hall effects should be even to the applied magnetic field B unlike normal Hall effect. So far, the planar Hall effect has been reported in only a few members of topological materials such as Na_3Bi, GdPtBi and Cd_3As_2 [107–109].

1.4.9. Giant orbital diamagnetism

The intra-band Berry curvature around the Dirac node gives rise to unconventional magnetic responses such as nontrivial Berry phase [23, 24] and chiral anomaly [33, 76, 77, 98] as discussed above. The research interest has so far been limited to the intra-band Berry curvature and its related physics. However, Dirac bands formed by the band crossing realize nontrivial topology of conduction and valence bands mixing, which gives rise to an inter-band Berry connection [110] between different bands. The inter-band Berry connection is defined as

$$\boldsymbol{A}_{nm}(\boldsymbol{k}) = i\langle u_n(\boldsymbol{k})|\nabla_{\boldsymbol{k}}|u_m(\boldsymbol{k})\rangle \tag{1.52}$$

similar to the intra-band Berry connection in Eq.1.26. Here, n and m $(n \neq m)$ are band indices.

The inter-band Berry connection gives rise to a giant orbital diamagnetism as discussed for Bi [80, 111]. The giant orbital diamagnetism of Dirac electrons shows unconventional chemical potential μ dependence. The orbital diamagnetism takes negative minimum when chemical potential μ is located within the Dirac mass gap where DOS, $D(\mu) = 0$ (Fig. 1.14). This contrasts to the conventional contributions such as the Pauli paramagnetism or the Landau diamagnetism which are proportional to $D(\mu)$. The exotic chemical potential μ-dependence originates from a topological character of orbital diamagnetism to which fully occupied states contribute via virtual inter-band excitations.

Large diamagnetism has been observed in bulk magnetic susceptibility of Bi and $Bi_{1-x}Sb_x$ [112–114], which has been attributed to the giant orbital diamagnetism of Dirac electrons. Recently discovered 3D TDS also shows a large diamagnetic susceptibility [115–117]. However, its microscopic origin has not been experimentally confirmed owing to the presence of hole pockets in Bi and/or other contributions. For example, core diamagnetism $\sim -10^{-4}$-10^{-5} emu/mol and Pauli paramagnetism enhanced by a large g factor, often observed in a topological semimetal, can be comparable to the giant orbital diamagnetism. NMR and μSR experiments may separate the spin and the orbital contributions, but ^{209}Bi NMR for $I = 9/2$
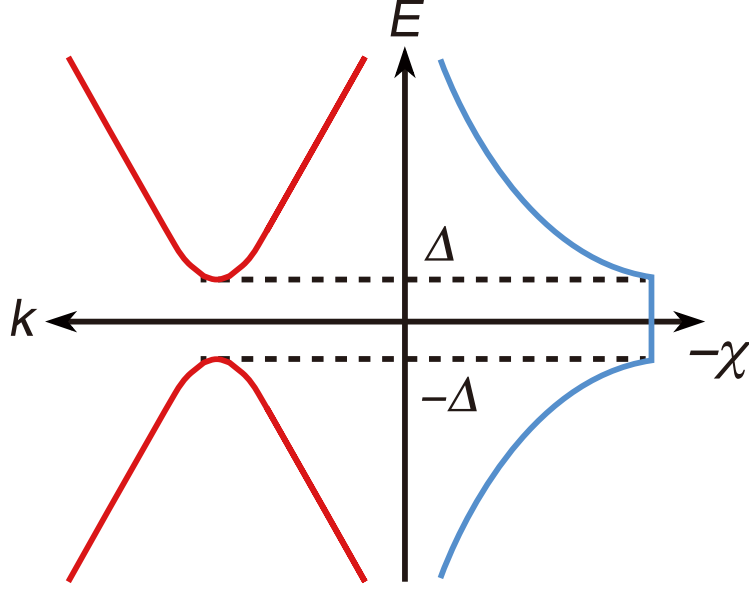
Fig. 1.14. Simplified picture of energy dispersion of massive Dirac electrons (left) and giant orbital diamagnetism (right). Δ is a Dirac mass gap. The orbital diamagnetism of Dirac electrons grows with approaching the gap and takes negative minimum within the mass gap.

nuclear spin is not a pure magnetic probe due to quadrupole interaction. Spin contribution cannot be estimated in the μSR measurement where Korringa relaxation is difficult to observe. NMR study on $I = 1/2$ nuclear spin without electric quadrupole interaction is a promising way to resolve spin and orbital contributions, though applicable nuclear species are limited.

1.4.10. Bulk susceptibility & NMR Knight shift

Bulk magnetic susceptibility χ is comprised of several contributions as

$$\chi(\mu, T) = \chi_{\text{spin}}(\mu, T) + \chi_{\text{orb}}(\mu, T) + \chi_{\text{core}} \tag{1.53}$$

where χ_{spin} and χ_{orb} are spin and orbital contributions respectively. A usual metal with carrier density $\sim 10^{22}$ cm^{-3} and with $g = 2$ shows a Pauli paramagnetism χ_{spin} of $\sim 10^{-4}$-10^{-5} emu/mol. χ_{core} is a core diamagnetism which is typically $\sim 10^{-4}$-10^{-5} emu/mol and independent of chemical potential μ and temperature T.

NMR Knight shift K has several contributions as

$$K = K_{\text{spin}}(\mu, T) + K_{\text{orb}}(\mu, T) + K_{\text{chem}}, \tag{1.54}$$

essentially the same as the bulk susceptibility in Eq.1.53. Here, K_{spin} and K_{orb} are spin and

orbital contributions respectively. These terms are written by

$$K_{\text{spin}} = \frac{A_{\text{spin}}\chi_{\text{spin}}}{N_A \mu_B} \tag{1.55}$$

$$K_{\text{orb}} = \frac{A_{\text{orb}}\chi_{\text{orb}}}{N_A \mu_B} \tag{1.56}$$

where N_A and μ_B are Avogadro constant and Bohr magneton respectively. Each term is proportional to χ_{spin} and χ_{orb} via respective hyperfine coupling constants A_{spin} and A_{orb}. The giant orbital diamagnetism of Dirac electrons should be observed as the orbital shift K_{orb}. The chemical shift K_{chem} is characterized by the interatomic distance and therefore insensitive to T and μ. K_{chem} acts as a constant offset of the Knight shift K.

To discuss hyperfine couplings, let us consider interaction between nuclear spin $\boldsymbol{I}$ and electron [118, 119]. Nuclear magnetic moment $\boldsymbol{\mu}_N = \gamma_N \hbar \boldsymbol{I}$ produces a vector potential

$$\boldsymbol{A}(\boldsymbol{r}) = \nabla \times \frac{\boldsymbol{\mu}_N}{r} \tag{1.57}$$

where r is a position from the nucleus. This leads to the interaction Hamiltonian

$$\begin{aligned} H &= \frac{1}{2m}\left(\boldsymbol{p} + \frac{e}{c}\boldsymbol{A}\right)^2 + g\mu_B \boldsymbol{S} \cdot (\nabla \times \boldsymbol{A}) \\ &= \frac{\boldsymbol{p}^2}{2m} + H_l + H_s + \frac{e^2}{2mc^2}\boldsymbol{A}^2 \end{aligned} \tag{1.58}$$

$$H_s = g\mu_B \boldsymbol{S} \cdot (\nabla \times \boldsymbol{A}) \tag{1.59}$$

$$H_l = \frac{e}{2mc}(\boldsymbol{p} \cdot \boldsymbol{A} + \boldsymbol{A} \cdot \boldsymbol{p}). \tag{1.60}$$

Here, using a formula

$$\nabla \times \nabla \times \frac{\boldsymbol{\mu}_N}{r} = \nabla\left(\nabla \cdot \frac{\boldsymbol{\mu}_N}{r}\right) - \nabla^2 \frac{\boldsymbol{\mu}_N}{r}, \tag{1.61}$$

a spin part H_s can be calculated as

$$H_s = \frac{8}{3}\pi g\mu_B \boldsymbol{s} \cdot \boldsymbol{\mu}_N \delta(\boldsymbol{r}) + g\mu_B\left(-\frac{\boldsymbol{s} \cdot \boldsymbol{\mu}_N}{r^3} + \frac{3(\boldsymbol{s} \cdot \boldsymbol{r})(\boldsymbol{\mu}_N \cdot \boldsymbol{r})}{r^5}\right). \tag{1.62}$$

The second term is dipole interaction for p, d and f electrons. The first term

$$H_{\mathrm{FC}} = \frac{8}{3}\pi g\mu_B \boldsymbol{s} \cdot \boldsymbol{\mu}_N \delta(\boldsymbol{r}) \tag{1.63}$$

is Fermi contact interaction to which s electrons contribute. K_{spin} by the Fermi contact interaction becomes

$$K_{\mathrm{spin}} = \frac{8}{3}\pi |\psi(0)|^2 \chi_{\mathrm{s}}. \tag{1.64}$$

Pauli paramagnetism χ_{s} is proportional to g^2, therefore $K_{\mathrm{s}} \propto g^2$. H_l is an orbital part and written by

$$\begin{aligned} H_l &= \frac{e}{2mc}\left(\boldsymbol{p} \cdot \frac{\boldsymbol{\mu}_N \times \boldsymbol{r}}{r^3} + \frac{\boldsymbol{\mu}_N \times \boldsymbol{r}}{r^3} \cdot \boldsymbol{p} \right) \\ &= 2\mu_B \frac{\boldsymbol{l} \cdot \boldsymbol{\mu}_N}{r^3} \end{aligned} \tag{1.65}$$

with $\hbar\boldsymbol{l} = \boldsymbol{r} \times \boldsymbol{p}$. When H_l is attributed to Van Vleck susceptibility, K_{orb} is given by

$$K_{\mathrm{orb}} = 2\left\langle \frac{1}{r^3} \right\rangle \chi_{\mathrm{orb}}. \tag{1.66}$$

The hyperfine coupling constants can be experimentally determined by T-dependence of a K versus χ diagram called K-χ plot. When only K_{spin} (K_{orb}) depends on temperature, the hyperfine coupling constant A_{spin} (A_{orb}) is given by a slope of the K-χ plot. In a conventional system, K_{orb} is attributed to T-independent Van Vleck susceptibility, and therefore the slope yields A_{spin}. A_{orb} cannot be obtained experimentally and the theoretical value of $A_{\mathrm{orb}} = 2\langle r^{-3} \rangle$ for the Van Vleck susceptibility in Eq.1.66 is employed to estimate K_{orb}. Diamagnetism from orbital motion of conduction electrons, which corresponds to Landau diamagnetism for free electron gas, is also independent of T. A_{orb} for the orbital motion is hard to be estimated by the K-χ plot and has not been discussed in experiments. However, the unconventional T-dependence is predicted for the giant orbital diamagnetism of Dirac electrons [120–122], which suggests A_{orb} for itinerant orbital motion of Dirac electrons can be experimentally extracted from the K-χ plot.

1.4.11. NMR spin lattice relaxation rate

Spin contribution of magnetic susceptibility can be captured by NMR spin lattice relaxation rate T_1^{-1}. T_1^{-1} can be written by

$$T_1^{-1} \propto \int d\varepsilon D(\varepsilon)^2 f(\varepsilon)\big(1 - f(\varepsilon)\big) \tag{1.67}$$

which is proportional to thermal average of square of DOS. Here, $f(\varepsilon) = 1/(1 + e^{(\varepsilon-\mu)/k_B T})$ and $D(\varepsilon)$ are Fermi distribution function and the DOS respectively. In a simple metal, the almost constant $D(\varepsilon)$ as a function of T leads to T-independent $(T_1 T)^{-1}$, known as the Korringa law.

DOS of 3D Dirac electrons in Eq.1.20 is not constant, which gives rise to unconventional temperature dependence of T_1^{-1}. When $\Delta = 0$, Sommerfeld expansion [123], applied to the integration in Eq.1.67, yields

$$T_1^{-1} \propto \left(\mu^4 k_B T + 2\pi^2 \mu^2 \big(k_B T\big)^3 + \frac{7}{15}\pi^4\big(k_B T\big)^5\right). \tag{1.68}$$

Here, the following formula

$$\int_{-\infty}^{\infty} \frac{x^n e^x}{(e^x + 1)^2} dx = \begin{cases} 0 & (n = \text{odd}) \\ 2n!\big(1 - 2^{1-n}\big)\zeta(n) & (n = \text{even}) \end{cases} \tag{1.69}$$

is used with zeta function $\zeta(n) = \Sigma_{l=1}^{\infty} 1/l^n$ such as $\zeta(2) = \pi^2/6$ and $\zeta(4) = \pi^4/90$. T_1^{-1} shows a crossover from T-linear to T^3- and T^5- behavior with increasing T. Note that the mass gap Δ can be neglected in the above calculation when $\mu^2 \gg \Delta^2$ is satisfied.

Because T_1^{-1} is scaled with the square of DOS, T_1^{-1} is associated with $K_{\text{spin}} \propto D(\varepsilon)$ via Korringa relation

$$T_1 T K_{\text{spin}}^2 = \frac{\hbar}{4\pi k_B}\left(\frac{\gamma_e}{\gamma_n}\right)^2 = S. \tag{1.70}$$

Here, γ_e and γ_n are gyromagnetic ratios of a electron and a nucleus, respectively. Eq.1.70 indicates a Korringa value S depends only on a kind of nuclei. Note S is often modified by a factor of 2 even in a simple metal [124].

In general, the Korringa value S may be scaled by g factor. Let us consider T_1^{-1} in non-magnetic and $I = 1/2$ system with the Fermi contact interaction in Eq.1.63. A transition rate w between spin up and down states is given by Fermi's Golden rule as

$$w \sim \frac{2\pi}{\hbar}\big|\langle i|H_{\text{FC}}|f\rangle\big|^2 \delta\big(E_i - E_f\big) \propto g^2 \tag{1.71}$$

where i and f represent initial and final states, respectively. T_1^{-1} is the summation of w over

the vicinity of FS and $T_1^{-1} \propto g^2$ holds. Beucase $K_\mathrm{s} \propto g^2$, the Korringa value S in Eq.1.70 is proportional to g^2.

Chapter 2

Antiperovskite A_3TtO ($A=$ Ca,Sr,Ba; $Tt=$ Sn,Pb)

As discussed in the previous chapter, 3D Dirac electrons can provide playground for unconventional magnetic responses such as chiral anomaly in the quantum limit and giant orbital diamagnetism. 3D TDS can be also driven into topologically distinct phases such as a Weyl semimetal or a topological insulator by breaking the symmetries or controlling the band gap. To explore unusual physics and the exotic phases derived from 3D TDS further, controllable systems with 3D Dirac electrons are highly desirable.

In this chapter, the antiperovskite family A_3TtO (A=Ca,Sr,Ba; Tt=Sn,Pb), theoretically proposed as a 3D massive Dirac electron system [35, 120], is introduced as an arena for the present study. The antiperovskite with certain chemical flexibility is a promising material family for band engineering of 3D Dirac electrons. The uniqueness of the antiperovskites as compared with other 3D TDSs is discussed.

2.1. Crystal structure

The antiperovskite A_3TtO has a cubic perovskite structure as shown in Fig. 2.1 (a). The O atom is surrounded octahedrally by the alkaline earth metals (A atoms) and forms an OA_6 octahedron. The Tt atom fills the space between OA_6 octahedra. The positions of metal atoms and O atoms are swapped as compared to those of normal cubic perovskite oxides as seen in Fig. 2.1 (b). The name of 'anti' perovskite originates from such exchange of the elements.

2.2. Band structure

In the ionic limit, the valence state of the antiperovskites can be written by $A_3^{2+}Tt^{4-}O^{2-}$. According to band calculation [35, 120, 125], the fully occupied $5p$ ($6p$) orbitals of Tt^{4-} ions and the empty $3d$ ($4d$ or $5d$) orbitals of A^{2+} ions form the valence bands and the conduction bands respectively. The p valence bands and the d conduction bands marginally overlap at Fermi energy (Fig. 2.2 (a)), and an energy gap opens at the band crossing due to the d-p hybridization. C$_4$ rotational symmetry of the crystals protects the band crossing against gap formation at the only six equivalent points on Γ-X lines which are C$_4$ rotational axes of the first Brillouin zone (BZ) (Fig. 2.2 (b)). This gives rise to six Dirac points around which anisotropic
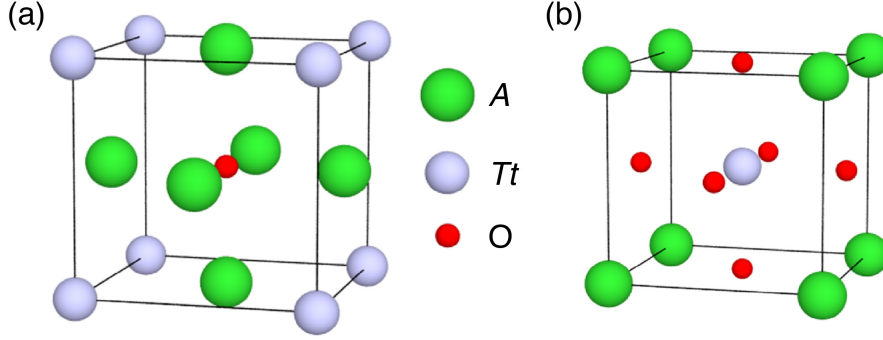
Fig. 2.1. (a) and (b) Crystal structures of antiperovskite A_3TtO and normal perovskite $ATtO_3$ (A=Ca,Sr,Ba; Tt=Sn,Pb). The O atom is surrounded by A atoms and forms an OA_6 octahedron in the antiperovskite A_3TtO, which contrasts to the normal perovskite $ATtO_3$.
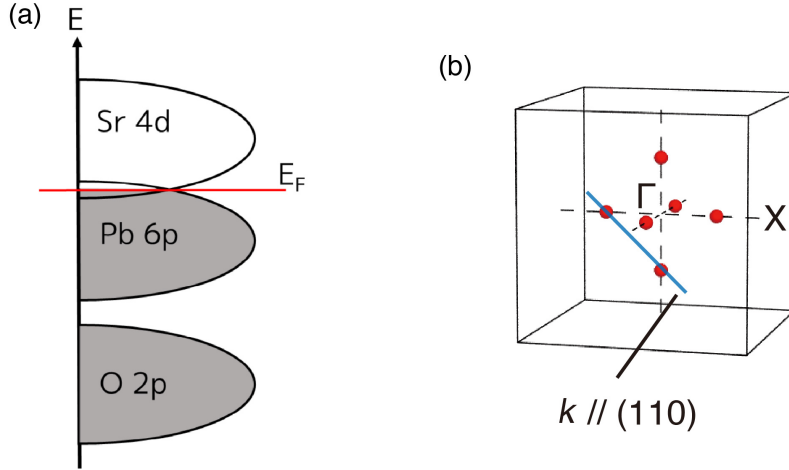

Fig. 2.2. (a) In Sr_3PbO antiperovskite, the fully occupied $6p$ orbitals of Pb^{4-} ions and the empty $4d$ orbitals of Sr^{2+} ions slightly overlap at the Fermi energy E_F. (b) The Dirac points of the antiperovskites are located at the red points on Γ-X lines which are C_4 rotational axes of the first BZ. The blue line parallel to the (110) direction connects the two Dirac points.

Dirac bands are found as seen in Fig. 2.3. The 3D Dirac bands are free from other parabolic bands, which indicates the antiperovskites are ideal platform to study 3D Dirac electrons. The band calculation predicts Fermi velocity v_F = 2-4 $\times 10^5$ m/s. High mobility carriers with extremely light effective mass can be expected. When the Fermi energy E_F shifts from the mass gap towards the valence bands, the 3D Dirac bands of Sr_3PbO merge together at a saddle point (SP) of $E_F \sim -125$ meV (Fig. 2.4) and finally form multi-bands FS. As shown in Fig. 2.4, the character of the band structure around E_F can be classified into three regimes: Dirac bands, SP and multi-bands.
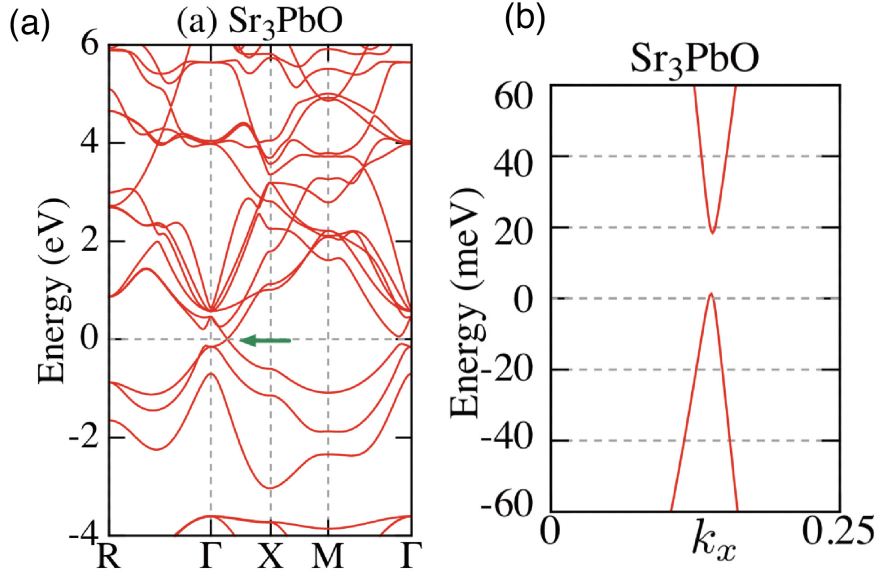
Fig. 2.3. The band structure of Sr_3PbO antiperovskite from [120] with permission from the author. The Dirac band denoted by the arrow in (a) is enlarged in (b). The Dirac band has a small mass gap of ~ 20 meV.
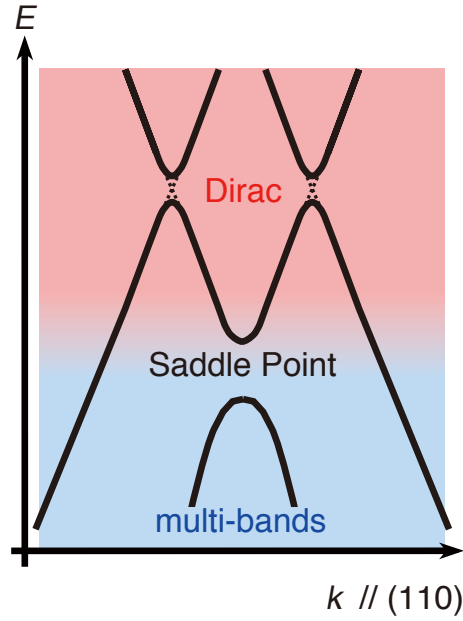

Fig. 2.4. The simplified band structure of Sr_3PbO antiperovskite for a k axis along (110) (blue line in Fig. 2.2 (b)). By moving the chemical potential μ from the Dirac mass gap to the valence band, the character of the band structure at the Fermi energy E_F can be classified into three regimes; Dirac bands (red area), a saddle point (SP) and multi-bands (blue area).

The 3D Dirac band has a small mass gap of ~ 10 meV, which means antiperovskites family is a 3D massive Dirac electron system. According to a tight binding model of the antiperovskites [120, 125], the mass gap opens perturbatively due to a small but finite hybridization of the higher energy orbital states to the Dirac bands via spin-orbit coupling. The magnitude of mass gap therefore depends on A and Tt elements. The presence of tunable mass gap opens up a possibility to design a richer variety of topological states. Ca_3PbO and Sr_3PbO were proposed as a candidate for TCI [126], where type-II Dirac surface states were recently predicted [127]. Ca_3PbO and Sr_3PbO can exhibit both the 3D Dirac states in bulk and 2D Dirac states on the surface similar to $Pb_{1-x}Sn_xSe$ [128, 129]. The TCI phase is characterized by the mirror Chern number $n_M = \pm 2$ on a (100) mirror plane. This implies the presence of nontrivial hinge states between (100) and (010) planes [130] though the nontrivial surface states are also protected by mirror symmetry. A higher order topological insulator phase, which does not possess gapless surface states but hosts nontrivial hinge states, may be realized by applying uniaxial pressure or strain which breaks mirror symmetry as discussed for SnTe [130].

A recent experiment shows unconventional magnetotransport properties by light mass carriers in Sr_3PbO [90], which supports the presence of 3D Dirac electrons. These results were reported in the master thesis of the author [132] and will be again presented in Chapter 4. ARPES study on Ca_3PbO was also consistent with the band calculation though the observation of the bands was limited below the Dirac points because of hole doping [131] (Fig. 2.5).

While band calculations from several groups [35, 120, 133–135] predicted 3D Dirac bands free from parabolic bands in Sr_3SnO, band calculation by T.H. Hsieh *et.al.* [126] shows the presence of hole pockets at R points in Sr_3SnO. Note E_F-dependence of weak localization observed in magnetotransport experiments on thin films of Sr_3SnO [134] was consistent with the band calculation without the hole pockets.

2.3. Band engineering

Temperature and a tolerance factor dependences of the crystal structure were previously reported [136], which indicates that the cubic perovskite structure is stable over a wide range of A and Tt atoms; $A = $ Ca, Sr, Ba and magnetic Eu and $Tt = $ Pb and Sn. The antiperovskites with chemical flexibility can provide a platform to control 3D Dirac electrons. The replacement of Sr with Ca shifts the Dirac points towards the Γ point [35, 120], which increases anisotropy of Fermi velocity and leads to more tilted Dirac bands in Ca_3PbO. Ba compounds undergo a structural phase transition at ~ 150 K, from cubic to orthorhombic upon cooling [136]. The orthorhombic structure breaks C_4 rotational symmetry and hence 3D Dirac electrons are no longer protected. Because spin orbit coupling determines the mass gap, the gap can be tuned by a Pb/Sn ratio as $Sr_3Pb_xSn_{1-x}O$ [137]. Band filling may be controlled by La or F doping as $Sr_{3-x}La_xPbO$ or $Sr_3PbO_{1-x}F_x$.
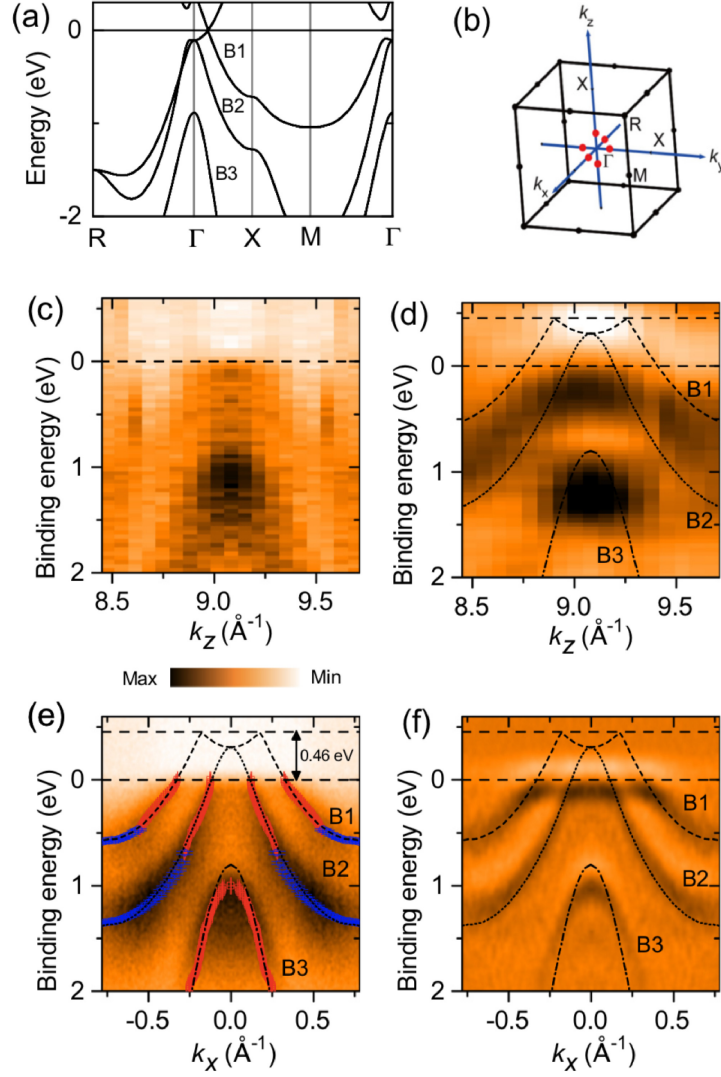
Fig. 2.5. Band structure and ARPES intensity plots of Ca_3PbO from Phys. Rev. B **96**, 155109 (2017) [131]. Copyright 2017, American Physical Society. (a) Band structure of Ca_3PbO. (b) The first BZ of Ca_3PbO. The Dirac points are located at the six red points on Γ-X lines. (c) and (e) ARPES intensity plots on the Γ-X line along k_z or k_x directions, respectively. The peak positions of momentum distribution curves and energy distribution curves are represented by red and blue respectively, which is in good agreement with the band calculation (black dashed lines). (d) and (f) The second-derivative of ARPES spectrum on the Γ-X line along k_z or k_x directions, respectively.

In addition, magnetism can be introduced to the antiperovskites by replacing alkaline earth metals with magnetic Eu as $Sr_{3-x}Eu_xPbO$ or Eu_3PbO where interplay between 3D Dirac electrons and magnetism may be expected. In fact, Eu_3PbO (Eu_3SnO) undergoes an antiferro-

magnetic (AFM) transition at $T_N = 42.9\,\mathrm{K}$ (33.2K) [137]. A series of metamagnetic transitions was observed in magnetization as a function of magnetic field, which reveals the complicated phase diagram. Because TRS is broken at the AFM phase where Kramers degeneracy is lifted, a magnetic Weyl semimetal phase may be realized in these compounds.

2.4. Comparison with other 3D Dirac semimetals

Na_3Bi was first theoretically proposed as a candidate for 3D TDS [15] and experimentally confirmed by ARPES measurements [17]. Na $3s$ orbitals and Bi $6p$ orbitals form conduction and valence bands, respectively. C_3 rotational symmetry protects 3D massless Dirac electrons with a strong anisotropy of a factor of 4. Magnetotransport measurements show negative longitudinal MR and planar Hall effects [105], consistent with the expected angle dependence. Because Na_3Bi with an unusual valence state of Bi^{3-} is air-sensitive similar to the antiperovskites, few experiments has been reported [17, 18, 98, 105] so far. Cd_3As_2 was predicted to be 3D TDS protected by C_4 rotational symmetry [16] and confirmed by ARPES experiments [20] similar to Na_3Bi. Cd_3As_2 is air-stable, which provides easy access to 3D Dirac electrons by many kinds of probes such as transport [22–30] and scanning tunnelling microscopy (STM) [138] experiments. Magnetotransport measurements on $Pb_{1-x}Sn_xSe$ [129] support the presence of bulk massive 3D Dirac electrons. Above the critical value of Sn content x, $Pb_{1-x}Sn_xSe$ undergoes a temperature driven topological phase transition by a gap inversion, leading to a TCI phase [128] with massive Dirac electrons in the bulk. Na_3Bi, Cd_3As_2 and $Pb_{1-x}Sn_xSe$ from PbSe or SnSe have only two kinds of elements to tune the chemical composition. The antiperovskites A_3EO with three kinds of elements would be easier to control 3D Dirac electrons.

TlBiSSe has been studied in the context of TI to observe a topological phase transition from trivial insulator $TlBiS_2$ to TI $TlBiSe_2$ [139, 140]. TlBiSSe is located at the topological transition point and hosts gapless states in bulk explained by 3D Dirac electrons. Large linear MR was observed [31] though the origin is not clear. $ZrTe_5$ was first theoretically proposed as a candidate for a TI [141] but experimental study is still controversial because of possibility of bulk 3D Dirac electrons [32–34]. According to band calculation [142], $ZrTe_5$ is located near a topological phase transition point between a weak TI and a strong TI, at which a 3D Dirac semimetal phase can be realized without symmetry protection. When $ZrTe_5$ is sufficiently close to the transition point, the band dispersion of $ZrTe_5$ can be regarded as a 3D Dirac dispersion and signatures of 3D Dirac electrons should be able to be captured. Because fine tuning is required to realize 3D Dirac semimetal phases in these materials, they have difficulty in controlling further the 3D Dirac electrons.

Bi has electron pockets described by massive 3D Dirac electrons with strong anisotropy [143]. Large diamagnetism was observed in bulk susceptibility of Bi and $Bi_{1-x}Sb_x$ [112–114], which is consistent with chemical potential dependence of the giant orbital diamagnetism of

Dirac electrons. Microscopic magnetism has been explored by NMR [144], muon spin rotation (μSR) [145, 146], perturbed angular distribution [147, 148] and β-NMR [149] to identify the orbital origin of the large diamagnetism. However, the attempts have not been successful owing to the presence of normal hole pockets and/or other contributions. For example, NMR experiments on $I = 9/2$ nuclear spin at ^{209}Bi involve large quadrupole interaction in Knight shift and phonon contribution in spin lattice relaxation rate, which obscure spin and orbital magnetic susceptibility of Dirac electrons.

To explore unconventional physics of 3D Dirac electrons mentioned in Chapter 1, chemical flexible 3D TDS, in which it is easy to break symmetries, to introduce magnetism, and to control band filling and spin-orbit coupling, is highly desirable. The antiperovskites A_3TtO with chemical flexibility is a unique and promising material family for band engineering of 3D Dirac electrons as discussed in Section 2.3. In addition, the antiperovskite family with $I = 1/2$ nuclear spin at ^{207}Pb and $^{117, 119}$Sn provides an ideal platform for NMR study of the giant orbital diamagnetism of Dirac electrons. Because of the cubic structure of the antiperovskites, the anisotropy of MR is induced by only magnetic field unlike non-cubic systems, for example TaAs family [104]. The antiperovskites is suitable to investigate chiral anomaly including the effect of current jetting.

2.5. Purpose of this research

The antiperovskites family can be a model system in which to design exotic topological phases and to explore unconventional magnetic responses. In this thesis, we focus on one of the antiperovskite family, Sr$_3$PbO. 3D Dirac electron in the antiperovskites was predicted by the band calculation [35, 120]. The first step of this study is experimental verification of 3D Dirac electrons in Sr$_3$PbO. As reported in the master thesis of the author [132] and [90], giant linear MR and high mobility were observed in magnetotransport measurements. An extremely light cyclotron effective mass of carriers was derived from SdH oscillations. These results strongly support the presence of 3D Dirac electrons in Sr$_3$PbO. To make the thesis self-contained, they are again presented in this thesis.

A next step is the investigation of unconventional physics anticipated in 3D Dirac electrons. The purposes of this study are shown in the following.

(1) Giant orbital diamagnetism of Dirac electrons in Sr$_3$PbO.

Although large diamagnetism has been observed in bulk susceptibility of Bi and Bi$_{1-x}$Sb$_x$, its microscopic origin has not been confirmed experimentally. We report bulk magnetic susceptibility and ^{207}Pb NMR experiments on Sr$_3$PbO antiperovskite samples with different carrier density from 10^{18} to 10^{20} cm^{-3}. Because of $I = 1/2$ nuclear spin species ^{207}Pb without electric quadrupole and phonon interactions, spin and orbital contributions of NMR Knight shift can be separated with the help of a Korringa relation.

(2) Unconventional transport induced by chiral anomaly in Sr_3PbO.

Chiral anomaly has been experimentally explored and expected negative longitudinal MR has been reported in several 3D TDSs. However, current jetting effects have raised ongoing discussion about these experiments. Angular dependent measurements of longitudinal MR and planar Hall effect have been reported in a limited number of materials. Considering the difficulty arising from strong anisotropy of MR, a suitable platform to study chiral anomaly including the current jetting effects is highly desirable. We report angular dependent magnetotransport experiments on cubic Sr_3PbO antiperovskite in which the anisotropy of MR is induced only by magnetic field. This helps us to discuss the effect of the current jetting in the transport measurements.

Chapter 3
Method

Because Sr_3PbO crystals are air-sensitive due to an extremely reduced valence state of Pb^{4-}, all processes of preparations and measurements were conducted without exposing the samples to air, for example, inside an Ar-filled glove box.

3.1. Single crystal growth

Single crystals of Sr_3PbO were grown by Sr-self flux method by the following reaction as reported by our collaborators [136].

$$xSr + PbO \rightarrow Sr_3PbO \tag{3.1}$$

Sr was distilled in order to remove oxides or hydrides impurity. The distilled Sr and PbO were sealed in a tantalum ampule which was further sealed in a niobium ampule to keep the sample away from oxygen and moisture. A 3-5% excess of Sr from a stoichiometric ratio, $x = 3.09$-3.15, increases crystal size and quality, which gives single crystals of ~ 500 μm with carrier density $n \sim 10^{18}$-10^{20} cm^{-3}. These samples were used for magnetotransport, bulk susceptibility and NMR experiments which will be reported in Chapter 4.

The extremely reduced ionic state of Pb^{4-} strongly favors an oxidation of the sample, and the crystals obtained at the early stages often had a high hole concentration of $n \gg 10^{18}$ cm^{-3}. However, the band calculation suggests 3D Dirac bands of Sr_3PbO can be accessed only for Fermi energy $|E_F| \leq 100$ meV [35, 120] which requires a very low carrier density of $n \leq\sim 10^{18}$ cm^{-3} or less. The condition of the synthesis was further optimized to grow cleaner and larger crystals with $n \leq\sim 10^{18}$ cm^{-3} and > 1 mm.

The distilled Sr and high purity PbO (Alfa Aesar, 99.9995%) were sealed in the same way as the previous report [136]. Typical temperature sequence is shown in Fig. 3.1. We controlled two parameters, the amount of Sr flux $x = 3.15$-4.5 and the highest temperature $T_{high} = 1350$, 1400 and 1450 °C. Large single crystals seem to be grown by large amount of Sr flux of $x \geq 3.6$ as seen in Fig. 3.2. The quality of the samples can be roughly characterized by the magnetization which strongly depends on the carrier density of the samples (see Appendix A). These characterizations suggest that lower carrier density samples can be obtained by the growth at high temperature of 1450 °C and large amount of Sr flux. The thresholds of
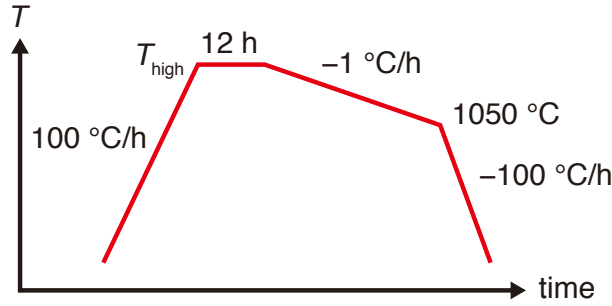
Fig. 3.1. Typical temperature sequence for single crystal growth for Sr_3PbO. The highest temperature T_{high} of 1350, 1400 and 1450 °C were used.
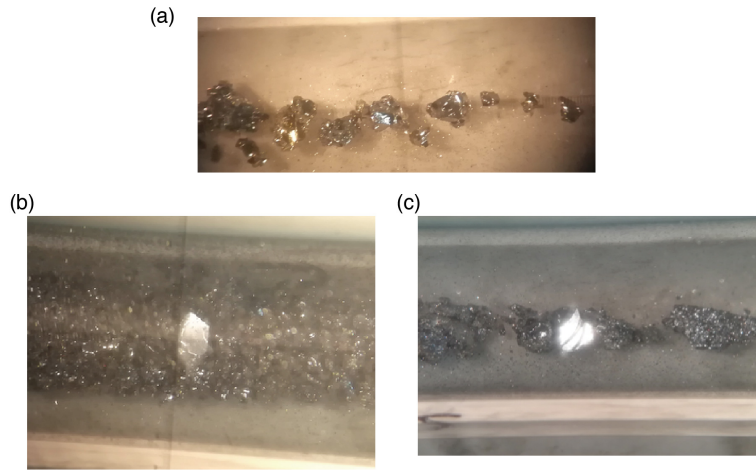

Fig. 3.2. Pictures of single crystals of Sr_3PbO synthesized by the temperature sequence in Fig. 3.1 with T_{high} = 1450 °C. (a) Single crystals of 0.5-1 mm were obtained by the Sr flux of $x = 3.45$. (b) and (c) Larger amount of Sr flux of $x = 3.6$ gives larger single crystals of 1-2 mm with shiny and flat surfaces.

the largest Sr/PbO ratio and the highest temperature were determined as following. Large amount of Sr at high temperature produces high pressure due to the evaporation of Sr, which can break the tantalum ampules when $x \geq 4.5$. Sr starts to react the tantalum ampule at $\sim$ 1450 °C, which involves tantalum impurity. We attempted a single crystal growth by placing Sr and PbO in BN or alumina crucibles. The crucibles was placed in a sealed tantalum ampule in order to avoid the contamination from tantalum impurity. However, sizable single crystals had not been obtained by the tantalum-tube technique.
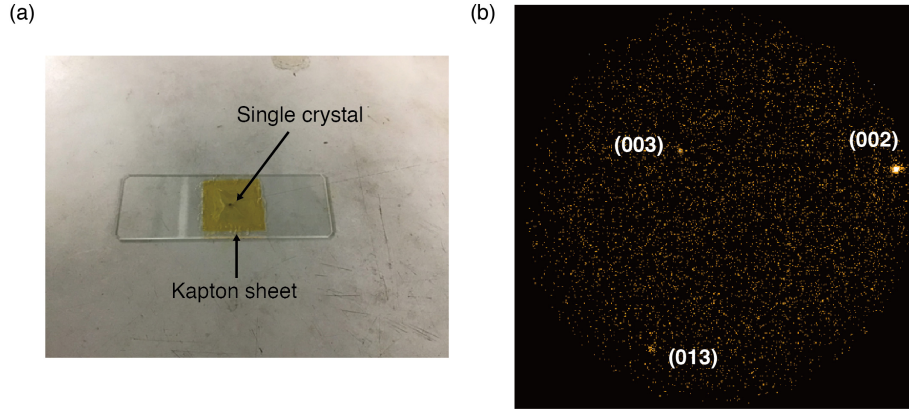
Fig. 3.3. (a) A single crystal of Sr_3PbO was sealed by a thin kapton film of 12.5 μm with Apiezon N Grease in the glove box, and then X-ray diffraction measurements were performed. (b) One of the diffraction patterns of a single crystal Sr_3PbO obtained by a 2D detector is shown. Three spots of (200), (300) and (103) can be identified.

3.2. X-ray diffraction

Because of the air-sensitivity of Sr_3PbO, it is difficult to take out a single crystal from the glove box for a single crystal X-ray diffraction. We have not determine a direction of a single crystal in early magnetotransport experiments, as reported in the master thesis [132]. Recently to conduct the angular dependent magnetotransport measurements, single crystal X-ray diffraction experiments were performed as following.

A single crystal was fixed on a slide glass by a double-sided kapton tape and sealed by a thin kapton film (12.5 μm) with Apiezon N Grease as shown in (Fig. 3.3 (a)). Additional getters Sr_3PbO or Sr_3SnO crystals were put together inside the sealing to catch possible oxygen and moisture. X-ray diffraction data were collected by D8 DISCOVER (Bruker AXS). The diffraction patterns with several spots from Sr_3PbO such as (200), (300), (102), (103), (113) and so on were obtained by a 2D detector (Fig. 3.3 (b)), which enables us to determine the crystal axes. The surface of the sample is gradually oxidized even in the sealing, which can be observed as continuous ring patterns. After several hours, the diffraction spots from the Sr_3PbO single crystal completely fades out. The X-ray measurements had to be finished in $\sim$ 1 hour.

3.3. Transverse magnetotransport

Single crystals were polished into a rectangular shape by alumina sandpapers using electron wax (Quickstick 135 Temporary Mounting Wax) which was removed by dehydrated acetone. Because the surface of the crystals may react with the acetone, the surface was scraped by tweezers to obtain the fresh and shiny surface. To ensure good electrical contacts, a gold film
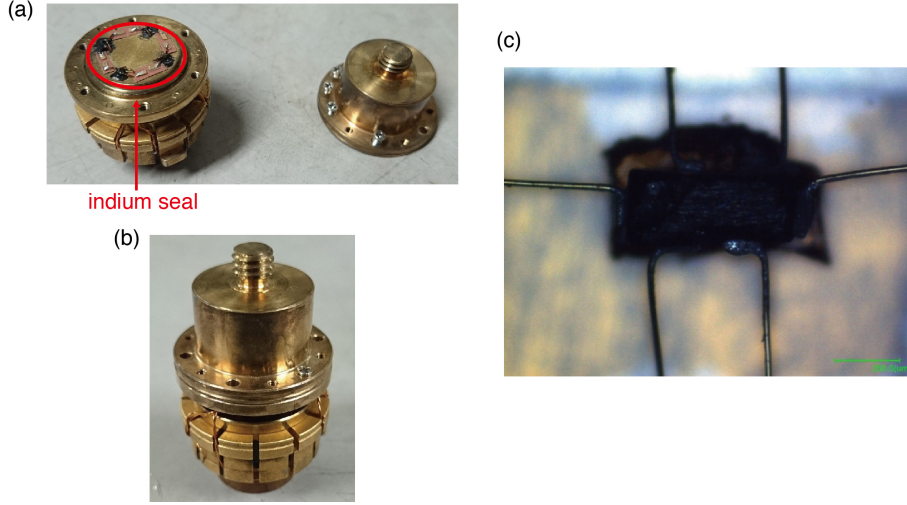
Fig. 3.4. (a) and (b) A sample holder with an air tight indium seal is used for the magnetotransport experiments by PPMS 14 T. (c) Six gold wires were attached to a single crystal of Sr_3PbO to measure the resistivity and the Hall resistivity.

as an electrode was made by a sputter coater (JEOL Smart Coater). A gold wire was attached there by conductive epoxy CW2400 (Circuit Works) with the help of a micromanipulator. The sample was fixed on a sapphire plate by a double-sided kapton tape, and then placed in a sample holder with an air tight indium seal (Fig. 3.4 (a-b)).

The magnetotransport measurements were performed by PPMS 14 T (Quantum Design) with magnetic fields normal to the applied current. A six probe configuration was used to measure the resistivity $\rho_{xx}(B)$ and the Hall resistivity $\rho_{xy}(B)$ (Fig. 3.4 (c)). We confirmed that the results for the two independent voltage pairs were consistent with each other, which eliminated any artifact arising from spatial inhomogeneity of the sample. To exclude the contributions to $\rho_{xx}(B)$ ($\rho_{xy}(B)$) from $\rho_{xy}(B)$ ($\rho_{xx}(B)$) due to the misalignment of electrodes, B-symmetric (B-asymmetric) parts of the raw data were extracted and presented as $\rho_{xx}(B)$ ($\rho_{xy}(B)$).

3.4. Angular dependent magnetotransport

The angular dependent magnetotransport experiments were performed by a two-axis rotation insert for PPMS 14 T with an air tight sample holder by an indium seal (Fig. 3.5 (a)). The sample holder can be rotated along two directions by two worm gears as shown in Fig. 3.5 (b), which enables us to realize exact alignment and to measure in-plane and out-of-plane angular dependences in the same setup. Two worm gears were attached to a rotational shaft which is connected to a rotational rod with a magnetic fluid seal at the top of the insert. Each rotational axis was controlled by a motor outside the vacuum chamber. As seen in Fig. 3.5 (b), a cernox
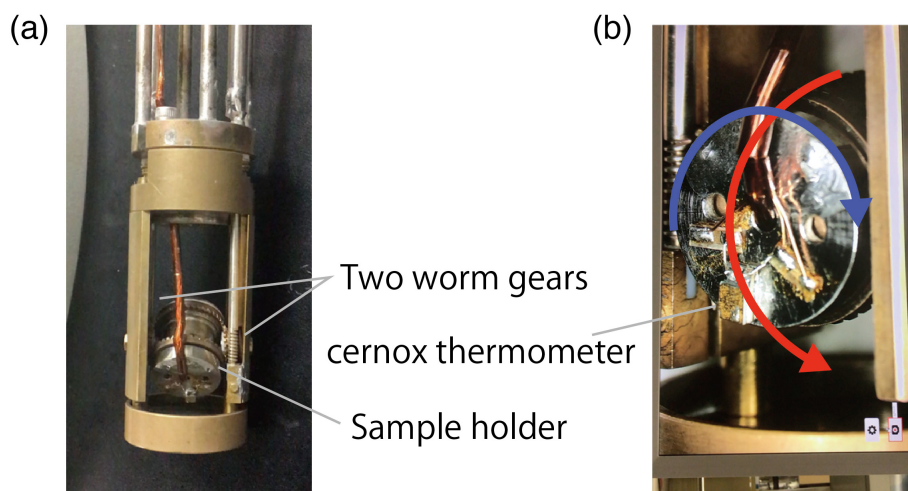
Fig. 3.5. (a) and (b) Angular dependent magnetotransport experiments were performed by a two-axis rotation insert for PPMS 14 T. An air tight sample holder can be rotated along two directions (red and blue arrows) by two worm gears. A cernox thermometer was attached to the sample holder.

thermometer was fixed on the sample holder by an indium soldering to measure temperature at the sample. Electrodes were prepared in a similar way to the transverse magnetotransport measurements in Section 3.3.

3.5. Bulk magnetic susceptibility

Powder samples of Sr_3PbO were sealed in glass tubes under helium gas as seen in Fig. 3.6 (a). The glass tubes with and without the samples were measured separately by a superconducting quantum interference device (SQUID) at a magnetic field 7 T. The SQUID signal only with the glass tube was subtracted from that with both the tube and the sample, yielding a resultant SQUID signal only from the sample (Fig. 3.6 (b)). The bulk susceptibility was derived from a fit to the resultant signal.

3.6. NMR

Powder samples from five batches of Sr_3PbO A-E were immersed in high-quality mineral oil (Daphne 7373) sealed in straws with epoxy resin inside the glove box. The samples in straws were mounted in an NMR coil. A magnetic field $B \sim 7$ T was applied, which was calibrated by [63]Cu NMR spectrum of the coil using gyromagnetic ratio $\gamma/2\pi = 11.2893305$ MHz/T and Knight shift $K = 0.200\%$. [207]Pb NMR experiments were conducted using Carr-Purcell-Meiboom-Gill multi-echo sequence with 10 echoes for the samples A-C or conventional spin-echo sequence for the samples D and E respectively. NMR spectra were obtained by a combina-
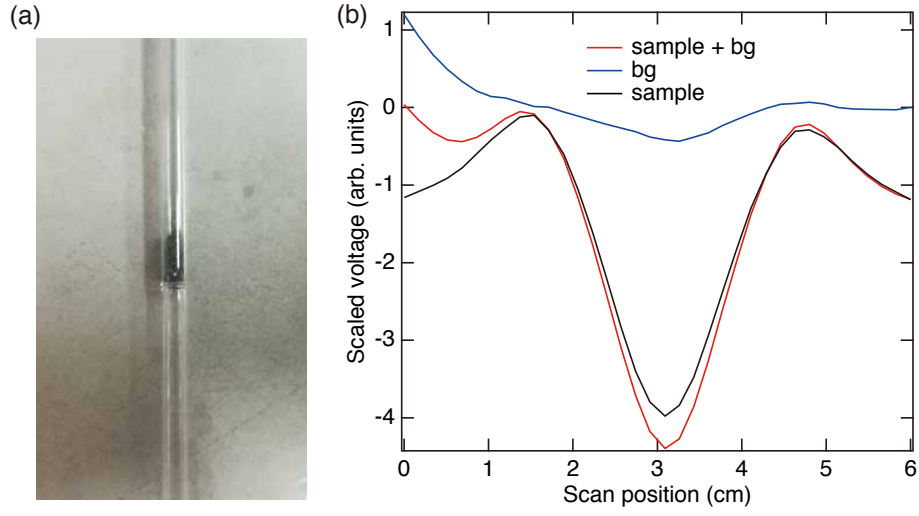
Fig. 3.6. (a) A powder sample of Sr_3PbO was sealed in a glass tube for bulk magnetic susceptibility measurements. (b) A resultant SQUID signal only from the sample (black line) was obtained by SQUID signals from the both the sample and the glass tube (red line) and from the glass tube (blue line).

tion of Fourier transformation and frequency sweep (Fourier-Step-Sum technique). The origin of peak shift Δf was defined as γB with gyromagnetic ratio of ^{207}Pb $\gamma/2\pi = 8.9072353\,\mathrm{MHz/T}$. NMR Knight shift $K = \Delta f/\gamma B$ is simply determined by the NMR frequency shift for $I = 1/2$ nucleus. Spin lattice relaxation rate T_1^{-1} was extracted from a single-exponential fit to the relaxation curves collected by a standard inverse saturation recovery method.

Chapter 4

Result & Discussion

4.1. Characterization

4.1.1. Carrier density

The carrier densities are characterized by the Hall resistivity $\rho_{xy}(B)$ measurements for single crystals from different batches as reported previously [90, 132]. $\rho_{xy}(B)$ in Fig. 4.1 for batches A and C-E in the zero field limit gives positive Hall coefficients $R_H = +3.8$, 0.13, 0.032 and 0.029 cm^3/C, yielding densities of holes $n = 1.6 \times 10^{18}$, 5.0×10^{19}, 2.0×10^{20} and 2.2×10^{20} cm^{-3} respectively. $\rho_{xy}(B)$ observed in the sample A shows nonlinear behavior in B, which can be attributed to the coexistence of high and low mobility carriers due to the mass anisotropy of six hole pockets as will be discussed in Section 4.2. This suggests $\rho_{xy}(B)$ in A seems to be dominated by the highly mobile hole pockets and the hole density of the sample A may be underestimated. All samples investigated in this study are hole doped, which is consistent with the previous reports [90, 131] and naturally expected from the viewpoint of chemistry. The valence states of Pb usually takes 2+ or 4+. The extremely reduced and anionic state Pb^{4-} should prefer an oxidation of the sample, for example through cation defects or excess of oxygens, which should lead to hole doping. Note that the sample quality can be also estimated by the bulk magnetic susceptibility which strongly depends on n (see Appendix A).

4.1.2. Fermi surface

As the chemical potential μ moves from the Dirac gap to the valence band, the character of the band structure near the chemical potential μ can be classified into three regimes; Dirac bands, a saddle point (SP) and multi-bands as shown in Fig. 4.2 (a). By comparing the carrier concentrations n and its energy dependence derived from the band calculation as Fig. 4.2 (b), Fermi energy E_F, chemical potential at 0 K, for the samples A, C, D and E are estimated to be $-45, -125, -235$ and -250 meV respectively. The sample A with $E_F = -45$ meV resides in the Dirac-bands. With increasing carrier densities n, E_F reaches the SP near the $E_F \sim -125$ meV of the sample C, and finally falls well below the Dirac bands, as the samples D and E seem to have multi-bands Fermi surfaces.
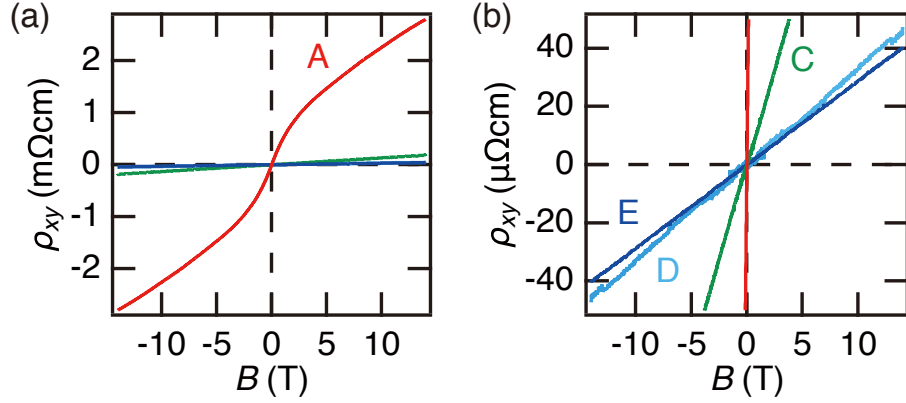
Fig. 4.1. (a) Field dependence of Hall resistivity $\rho_{xy}(B)$ in the zero field limit gives the hole densities of $n = 1.6 \times 10^{18}$, 5.0×10^{19}, 2.0×10^{20} and 2.2×10^{20} cm^{-3} for the samples A, C, D and E respectively. Small $\rho_{xy}(B)$ for the samples C-E is enlarged in (b).
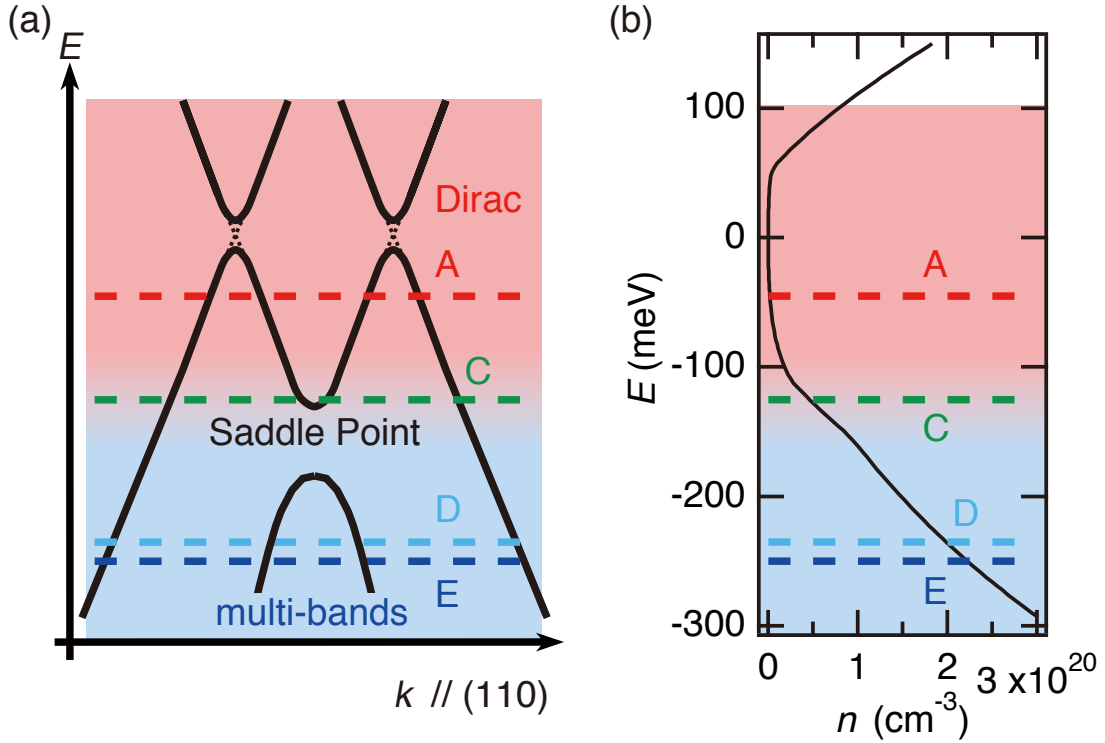

Fig. 4.2. (a) Simplified band structure of antiperovskite Sr$_3$PbO is again presented. The sample A belongs to the Dirac bands (red area) and the sample C is located near the SP. The samples D and E reside in the multi-bands (blue area). (b) Energy dependence of carrier concentration n was derived from the band calculation. Fermi energies E_F for the samples A, C, D and E was determined by carrier density n from Hall resistivity. The corresponding E_F is denoted by dashed lines in (a) and (b).

4.2. Presence of 3D Dirac electrons

As discussed in 4.1.2, a signature of 3D Dirac electrons is anticipated in a sample with low carrier density of $n \sim 10^{18}$ cm^{-3}. In this section, the transverse magnetotransport measurements and NMR spin lattice relaxation rate for samples with similar carrier density to the sample A in Fig. 4.2 are reported, which provides the evidence for the presence of 3D Dirac electrons in Sr$_3$PbO. The results for the magnetotransport measurements has been already reported in part in the master thesis [132] and published in [90]. Those already reported in the master thesis are again presented to make the thesis self-contained. Note the orientation of the single crystal for the magnetotransport experiments was not determined. However, the observed SdH oscillations, in conjunction with the result of magnetic torque measurements [137, 150], suggest that magnetic field is applied to a direction close to a (100) axis of the crystal. Bulk superconductivity, as reported in polycrystalline Sr$_{3-x}$SnO [133], was not observed in our single crystals down to 2 K (See also Appendix B).

4.2.1. Hall resistivity & Magnetoresistance

Temperature dependence of resistivity $\rho_{xx}(T)$ for a single crystal of Sr$_3$PbO shows metallic behavior with a residual resistivity $\rho_{xx}(0) = 90~\mu\Omega$cm and a residual resistance ratio (RRR) of ~ 10 (Fig. 4.3 (a)). The Hall resistivity $\rho_{xy}(B)$ in the zero field limit gives a positive and T-independent Hall coefficients $R_H = +3.8$ cm^3/C, yielding a low density of holes $n = 1.6 \times 10^{18}$ cm^{-3} (Fig. 4.4 (a)). $\rho_{xy}(B)$ in Fig. 4.4 (a) is nonlinear in magnetic field B similar to a two carrier model. The mass anisotropy of six hole-pockets, which will be discussed later, may give rise to the coexistence of high and low mobility carriers. Within the two carrier model, the T-independent R_H in the inset to Fig. 4.3 (a) suggests that only the highly mobile holes dominate $\rho_{xy}(B)$ in the low field limit. The Hall mobility is estimated to be 4.4×10^4 cm^2/Vs in the low temperature limit, comparable to those reported for other 3D Dirac systems such as Cd$_3$As$_2$ [23, 24] and ZrTe$_5$ [34]. The high mobility of carries is consistent with the presence of 3D Dirac electrons.

A giant MR ratio $\Delta\rho_{xx}(B)/\rho_{xx}(0)$ of over 10 at $B = 14$ T was observed at the lowest temperature measured, $T = 2$ K as seen in the inset to Fig. 4.4 (c). $\rho_{xx}(B)$ shows B-linear behavior over a wide range of magnetic field B from 1 T up to 14 T, where no trace of saturation is recognized (Fig. 4.4 (c)). Similar results has been reported in other 3D TDSs [22–24, 26, 27, 31, 98] and other topological semimetals [151–153]. The close similarity to other 3D TDSs is indicative of the presence of 3D Dirac electrons in Sr$_3$PbO.

While $\Delta\rho_{xx}(B)/\rho_{xx}(0)$ shows a decrease with increasing T, the B-linear contribution in $\Delta\rho_{xx}(B)$ at high fields is independent of T at least up to 200 K. This is demonstrated by
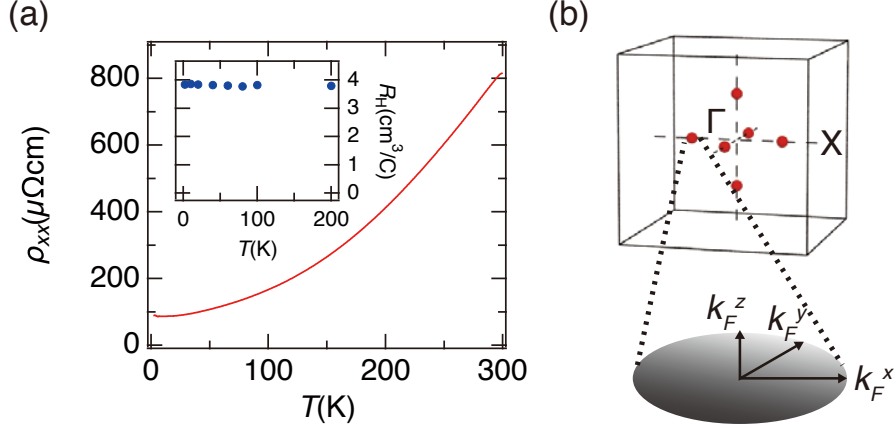
Fig. 4.3. (a) Temperature dependence of resistivity $\rho_{xx}(T)$ from 300 K to 2 K decreases upon cooling. The inset shows temperature independent Hall coefficients $R_H = +3.8$ cm^3/C. (b) The first BZ and the Fermi surface for the Dirac bands. k_F^i for $i = x, y, z$ are Fermi wave vectors.

the T- and B- independent derivative of resistivity $d\rho_{xx}/dB$ in Fig. 4.4 (d). $\Delta\rho_{xx}(B)/\rho_{xx}(0)$ in the B-linear region is therefore scaled by $B/\rho_{xx}(0,T)$, where a Kohler's rule,

$$\Delta\rho_{xx}(B,T)/\rho_{xx}(0,T) = f\big(B/\rho_{xx}(0,T)\big) \tag{4.1}$$

is satisfied.

In the low field limit, $\Delta\rho_{xx}(B)$ shows B^2-behavior as seen in almost B-linear behavior of $d\rho_{xx}/dB$. The slopes of $d\rho_{xx}/dB$ for different temperatures overlie each other as seen in Fig. 4.4 (d), which indicates that the magnitude of the B^2 contribution of $\Delta\rho_{xx}(B)$ in the zero field limit is almost independent of T. In contrast to B-linear contribution at high fields, the low field B^2 contribution apparently violates the Kohler's rule of Eq.4.1, which cannot be explained by a classical B^2 MR.

A crossover from the low-field B^2 to the high field B-linear behaviors can be recognized in $d\rho_{xx}/dB$ in Fig. 4.4 (d). A crossover field B_c^{MR} can be represented by the magnetic field at which $d\rho_{xx}/dB$ shows a peak (inset to Fig. 4.4 (d)). B_c^{MR} increases with T and is scaled by T-dependent resistivity $\rho_{xx}(T)$ as seen in Fig. 4.4 (e).

The nonlinear B dependence of $\rho_{xy}(B)$ in Fig. 4.4 (a) reflects the crossover from B^2 to B-linear behavior observed in $\Delta\rho_{xx}(B)$. The nonlinear behavior is better visualized in the derivative $d\rho_{xy}/dB$ in Fig. 4.4 (b). A crossover of $d\rho_{xy}/dB$ is observed from a B-linear and T-independent decrease well below 1 T to a weak and again T-independent decrease at high
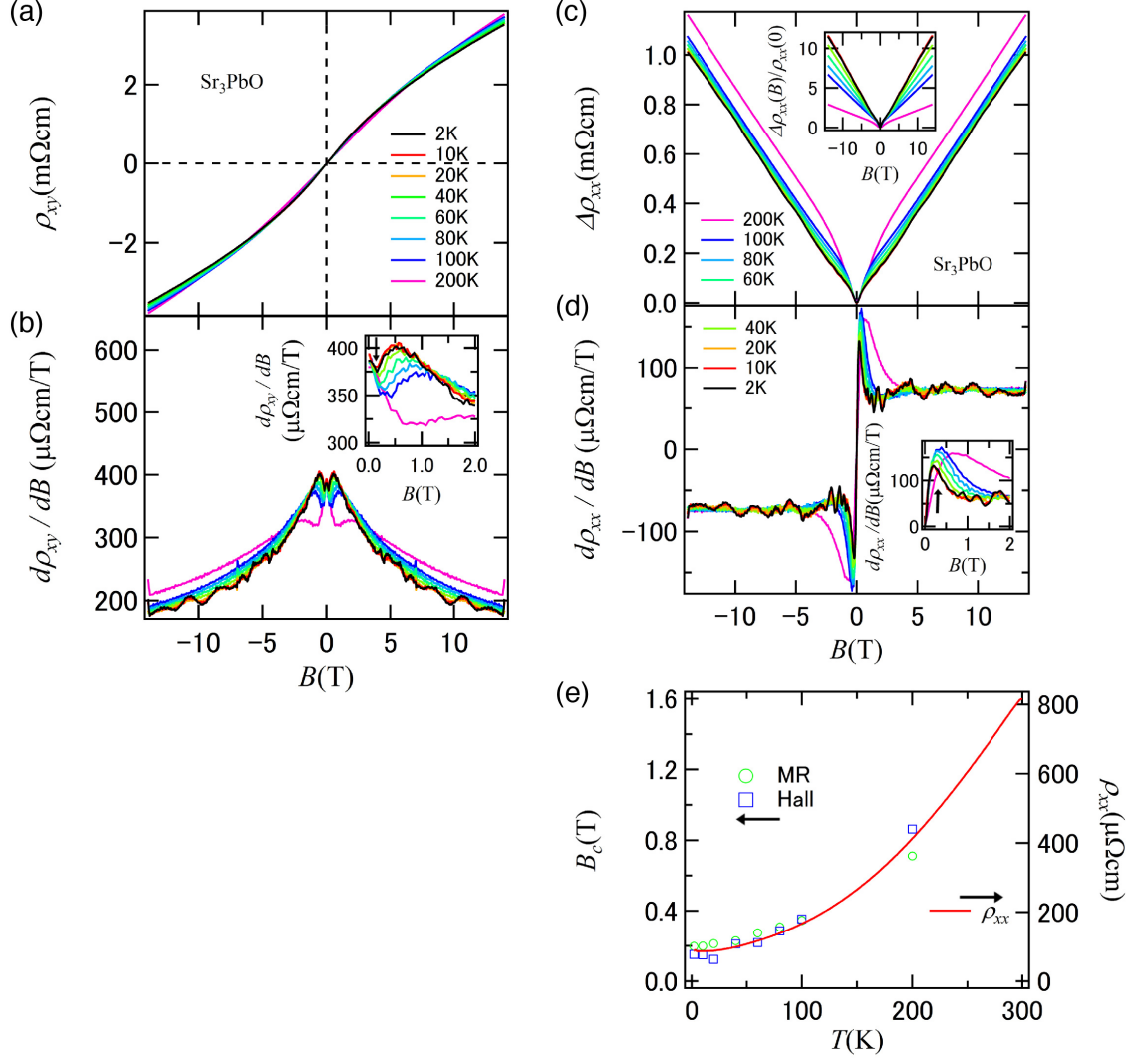
Fig. 4.4. Hall resistivity and magnetoresistance of the single crystal of Sr_3PbO. (a) Magnetic field B dependence of $\rho_{xy}(B)$ is nonlinear in B and independent of T up to 200 K. $\rho_{xy}(B)$ in the zero field limit gives a low density of holes $n = 1.6 \times 10^{18}$ cm^{-3}. (b) The nonlinear behavior of $\rho_{xy}(B)$ is more clearly distinguished in the derivative $d\rho_{xy}/dB$. A crossover field from low field T-independent to high field T-independent behavior is denoted by the black arrow in the inset. (c) A large MR ratio $\Delta\rho_{xx}(B)/\rho_{xx}(0)$ over 10 at $B = 14$ T was observed at $T = 2$ K as seen in the inset. Magnetic field dependence of $\Delta\rho_{xx}(B) = \rho_{xx}(B) - \rho_{xx}(0)$ shows B-linear and T-independent behavior, which is better recognized in the T-independent and constant derivative $d\rho_{xx}/dB$ at high fields in (d). A crossover field from B^2 to B-linear behavior in $\Delta\rho_{xx}(B)$ is indicated by the black arrow in the inset. (e) The crossover field B_c defined by the peak of $d\rho_{xx}/dB$ (circle) and by the dip of $d\rho_{xy}/dB$ (square) seems scaled by $\rho_{xx}(T)$ (line).

fields, as seen in (Fig. 4.4 (b)). The crossover magnetic field B_c^{Hall} may be represented by the

field of the dip in $d\rho_{xy}/dB$ (black arrow in the inset to Fig. 4.4 (b)), which well agrees with the corresponding crossover field B_c^{MR} as shown in Fig. 4.4 (e). The crossover B_c between the two T-independent magnetotransport regions commonly observed in $\Delta\rho_{xx}(B)$ and $\rho_{xy}(B)$ is scaled with $\rho_{xx}(T)$ and hence the T-dependent scattering rate $1/\tau$, which means the crossover is controlled by $B\tau(T)$.

4.2.2. SdH oscillations

SdH oscillations are superposed at least up to 40 K as clearly seen in $d\rho_{xx}/dB$. The observation of the SdH oscillations up to high temperature suggests an extremely light cyclotron effective mass, which supports the presence of 3D Dirac electrons. The SdH oscillations were derived from $\rho_{xx}(B)$ by subtracting a polynomial background (Fig. 4.5 (a)). The oscillations are composed of two different traces with frequencies of 4.98 ± 0.30 and 31.5 ± 2.4 T hereinafter referred as 5 and 32 T respectively. The 5 T oscillations cannot be recognized above $B \sim 5$ T. This indicates the quantum limit is reached above $B \sim 5$ T for the 5 T oscillations, which is lower than or comparable to those reported for other 3D TDSs [27, 34, 98, 129]. This means that the antiperovskite Sr_3PbO provides a promising platform to explore the physics of the quantum limit. The 32 T oscillations persist up to higher fields than 14 T and the quantum limit cannot be realized in the experiments. In angle-dependent torque magnetometry experiments on Sr_3PbO [137, 150], quantum oscillations with similar frequencies were observed when magnetic field is applied along the (100) axis. This suggests that the magnetic field orientation is along a direction close to the (100) axis of the sample in this magnetotransport measurement.

The cyclotron effective masses m_c^* for the two oscillations are derived from the fit to the temperature dependence of the magnitude of the oscillations using the Lifshitz-Kosevich formula [88] (inset to Fig. 4.5 (b)). The clear oscillation peaks at 0.64 T^{-1} (black arrow in Fig. 4.5 (b)) and 0.11 T^{-1} (black arrow in the inset to Fig. 4.5 (b)) were selected for the fitting. The fits to these peaks yield m_c^* of $0.011 m_e$ and $0.057 m_e$ for the 5 T and 32 T oscillations respectively. The extremely light effective mass of $\sim 1\%$ of the free electron mass is consistent with the presence of 3D Dirac electrons in Sr_3PbO. The difference in m_c^* between two oscillations may be attributed to the anisotropy of six hole pockets, which will be discussed later.

The nontrivial Berry phase of Dirac electrons can be captured by an extra phase offset of SdH oscillations. This offset β can be extracted from the Landau fan diagram for the position of maxima in SdH oscillations of σ_{xx},

$$n = \frac{F}{B} - \frac{1}{2} + \beta - \frac{1}{8} \tag{4.2}$$

where n, F and B are the maximum index, the frequency of SdH oscillations and magnetic

field, respectively. In an ideal Dirac electron system, the extra offset phase β corresponds to the Berry phase π associated with the cyclotron motion [2, 3, 23]. Indeed, $\beta = 0.5$ is expected for the ideal Dirac dispersion and $\beta = 0$ for a trivial k^2 dispersion [74]. The additional factor $-1/8$ reflects the three dimensionality and the maximal cross-sectional area [83–85]. Note $\sigma_{xx} > \left| \sigma_{xy} \right|$ and hence $\rho_{xx} \simeq \sigma_{xx}/\sigma_{xy}^2$ holds in the field range where the SdH oscillations are observed. Therefore, we assigned the maxima of σ_{xx} to the maxima of ρ_{xx} as discussed in [86].

Such fits to Eq.4.2 for the two frequencies are presented in Fig. 4.5 (b). In order to avoid deviations arising from the quantum limit [154], the fit for the 5 T oscillations was limited to $n \geq 1.5$. $\beta = 0.76 \pm 0.16$ and $\beta = 0.44 \pm 0.26$ were obtained for the 5 T and the 32 T oscillations, respectively. These values are incompatible with the trivial value 0, although they deviate from 0.5 expected for the ideal Dirac dispersion. Such deviations have also been seen in, for example, Cd_3As_2 [25] and can be attributed to the quadratic terms not considered in the ideal Dirac dispersion as well as to the significance of spin splitting at high magnetic fields [82, 154, 155]. However, large errors involving the determination of peak positions make it difficult to draw clear conclusion about the offset in Landau levels. A more detailed analysis of the phase will be left for future work.

Let us discuss the FS geometry and the relevant physical parameters of Sr_3PbO from the SdH oscillations with two different frequencies. Here, we assume that the FS has an ellipsoidal shape and the magnetic field is applied to the direction close to the (100) axis. The three principal Fermi momenta k_F^i ($i = x, y, z$) are defined for the FS on the (100) axis as in Fig. 4.3 (b). $k_F^y = k_F^z$ is satisfied due to C_4 rotational symmetry of the (100) axis. There should be two different cross-sectional areas normal to the field, $\pi k_F^y k_F^z$ for two FSs on the (100) axis and $\pi k_F^x k_F^y = \pi k_F^x k_F^z$ for the other FSs on (010) and (001) axes. The frequencies for 5 T and 32 T oscillations correspond to the cross-sectional areas 5.0×10^{-4} and 2.8×10^{-3} Å, respectively. If we assign the small (5 T) and the large (32 T) cross sections to $\pi k_F^y k_F^z$ and $\pi k_F^x k_F^y$ respectively, we obtain $k_F^x = 5.6 k_F^y = 0.073$ Å. These k_F values give a carrier density of $n_{\mathrm{SdH}} = 6 \times k_F^x k_F^y k_F^z/3\pi^2 = 2.5 \times 10^{18}$ cm^{-3}, where a factor of 6 comes from six hole-pockets. Note that if we consider a compressed FS instead of one elongated along the (100) axis, $5.6 k_F^x = k_F^y = 0.030$ Å and $n_{\mathrm{SdH}} = 1.0 \times 10^{18}$ cm^{-3} result. We cannot rule out at this stage the possibility of oblate FS as the agreement between n_{SdH} and n_{Hall} for oblate FS is not entirely unreasonable given the uncertainty of the relevant parameters.

Using $E_F = m_c^* v_F^y v_F^z = m_c^* E_F/\hbar k_F^y \times E_F/\hbar k_F^z$, we obtain a Fermi energy of $E_F = 117$ meV and Fermi velocities of $5.6 v_F^x = v_F^y = v_F^z = 1.4 \times 10^6$ m/s from the cyclotron effective mass $0.011 m_e$ for the 5 T oscillations. The same analysis applies for 32 T oscillations and gives consistent values, $E_F = 127$ meV and $5.6 v_F^x = v_F^y = v_F^z = 1.5 \times 10^6$ m/s. Using $E_n = \sqrt{2 v_F^y v_F^z \hbar eBn}$, the energy of $n = 1$ LL mode E_1 for 5 T oscillations is estimated to be 114 meV at 5 T. $E_1 \sim E_F$ at 5 T is consistent with the realization of the quantum limit at 5 T. If we consider the case for
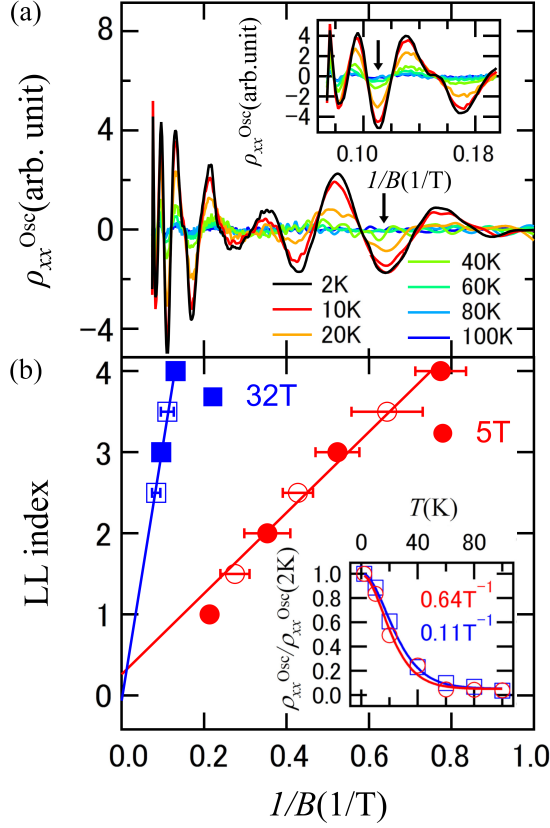
Fig. 4.5. SdH oscillations of Sr_3PbO. (a) SdH oscillations $\rho_{xx}^{\text{Osc}}(B)$ were obtained by subtracting a polynomial background from $\rho_{xx}(B)$. Two sets of oscillations with frequencies of 4.98 ± 0.30 and 31.5 ± 2.4 T were observed. The 32 T oscillations above ~ 6 T is emphasized in the inset. (b) The phase offset associated with the nontrivial Berry phase can be captured by Landau fan diagram. Both peaks (closed symbols) and dips (open symbols) of SdH oscillations with two different frequencies 5 T and 32 T are plotted. Extrema of SdH oscillations and their errors were determined by Gaussian fitting of SdH oscillation peaks. $\beta = 0.76 \pm 0.16$ and $\beta = 0.44 \pm 0.26$ were extracted from the linear fit to the 5 T and 32 T oscillations, respectively. The cyclotron effective mass m_c^* can be derived from the fit to the temperature dependence of the oscillations amplitude by a Lifshitz-Kosevitch formula. The amplitude for clear oscillation peaks at 0.64 T^{-1} (black arrow in (a)) and 0.11 T^{-1} (black arrow in the inset of (a)) are plotted as a function of temperature in the inset, representing 5 T and 32 T oscillations. The fits yield extremely light m_c^* of $0.011 m_e$ and $0.057 m_e$ for the 5 T and 32 T oscillations.

compressed FS, the same analysis yields $E_F = 111$ meV, $v_F^x/5.6 = v_F^y = v_F^z = 0.6 \times 10^6$ m/s and $E_1 = 111$ meV at 5 T. This is also consistent with the quantum limit at ~ 5 T. Note a mass gap of $\Delta \sim 10$ meV predicted in the band calculations [35, 120] is negligible in the calculation of E_F and E_1, as Δ is much smaller than derived E_F and E_1. The two cross sectional areas in

the SdH oscillations give an almost the same E_F values, which supports the assumption that they originate from the equivalent FSs. The angular dependence of de Haas-van Alphen effect around (100) observed in torque magnetometry experiments [137, 150] on single crystals with smaller carrier density than that of the present crystal gives an "extrapolated" anisotropy of 2-3, a factor of 2 smaller than the present estimate. In the band calculation, the anisotropy was predicted to be 2-3 [120] . The difference may suggest the presence of a more complicated FS shape than ellipsoid for a higher carrier concentration, which should be clarified in the future.

The above estimate of the Fermi energy $E_F \sim -100$ meV is a factor of 2 larger than $E_F \sim -50$ meV derived from the carrier density n in Fig. 4.2. The latter, $E_F \sim -50$ meV, is fully consistent with the magnitude of $(T_1 T)^{-1/2}$ as will be discussed in 4.4.3, which implies that $E_F \sim -100$ meV is overestimated. The limited number of oscillations and the beating pattern from two different frequencies, in conjunction with the suggested complicated FS shape, may involve the large errors of m_c^* and hence E_F by a factor of ~ 2. Note that, in the above discussion, both calculated E_F and E_1 are scaled with $1/m_c^*$. This gives the good agreement between E_F and E_1 even if m_c^* deviates from the above estimate.

4.2.3. Origin of linear MR

Let us turn our attention to an origin of linear MR. To understand B-linear profile of MR in Dirac electron systems, two models are often employed. However, at least in their original forms, they do not provide a full account for the experimental observations. One is the classical disorder model discussed in doped silver chalcogenides [91–93], Cd_3As_2 [24] and GaAs quantum wells [94], where B-linear $\rho_{xx}(B)$ is attributed to $\rho_{xy}(B)$. The observed relation between $\Delta\rho_{xx}(B)$ and $\rho_{xy}(B)$ via mobility supports this scenario. However, it is not obvious at all in this scenario why there is T-independence of $\Delta\rho_{xx}(B)$ and $\rho_{xy}(B)$ in conjunction with T-dependence of $\rho_{xx}(B)$ and the absence of nonlinearity in $\Delta\rho_{xx}(B)$ out of nonlinear $\rho_{xy}(B)$. The other scenario is quantum magnetoresistance for Dirac electrons in the quantum limit [89]. This may account for the T-independent and B-linear $\Delta\rho_{xx}(B)$. However, the crossover from B^2 to B-linear behavior seems to be controlled by $B\tau$ rather than the realization of the quantum limit at $B = 5$ T. When magnetic field is applied to the (100) axis, the originally equivalent six hole pockets may split into the two groups because of the anisotropy. These two contributions can have different mobilities under the field, but the very weak temperature dependence of $\Delta\rho_{xx}(B)$ and $\rho_{xy}(B)$ makes the analysis in terms of the naïve two-carrier model and hence the interpretation of $\Delta\rho_{xx}(B)$ and $\rho_{xy}(B)$ very difficult. We cannot exclude the possibility that FS anisotropy can explain the difficulties of the two scenarios at this stage. Measurements with the field parallel to the (111) direction, where six hole pockets remain equivalent, can eliminate the complication from the FS anisotropy, which may discriminate between the two scenarios.
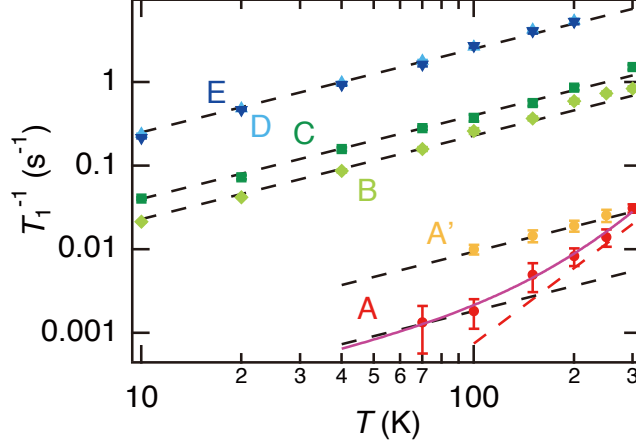
Fig. 4.6. Temperature dependence of NMR spin lattice relaxation rate T_1^{-1}. T_1^{-1} of the sample A shows crossover from T-linear (black dashed line) to T^3 behavior (red dashed line) with increasing T, which reflects the DOS of 3D Dirac electrons $D(E) \propto E^2$. The numerical calculation of T_1^{-1} by Eq.1.68 (solid line) is consistent with the experimental results for the sample A.

4.2.4. Spin lattice relaxation rate

Here, we briefly discuss the temperature dependence of NMR spin lattice relaxation rate T_1^{-1} observed in the ^{207}Pb NMR experiments on the powder sample from the same batch as the sample A with low carrier concentrations $n = 1.6 \times 10^{18}$ cm^{-3}, which supports the presence of 3D Dirac electrons in Sr$_3$PbO. NMR experiments including the sample dependence of T_1^{-1} will be discussed in Section 4.4 in more detail.

The energy dependence of DOS can be captured by spin lattice relaxation rate

$$T_1^{-1} = \int D(E)^2 f(E)(1 - f(E)). \tag{4.3}$$

In a simple metal with a constant $D(E)$ as a function of T, constant $(T_1 T)^{-1}$ is expected, known as the Korringa law. T_1^{-1} in all the samples shows T-linear behavior in the low temperature limit as seen in Fig. 4.6. At higher temperature, T^3 behavior of T_1^{-1} was observed in the sample A, which can be attributed to strongly E-dependent DOS of 3D Dirac electrons, $D(E) \sim E^2$. Similar results were reported and discussed in T^3 behavior in organic quasi 2D Dirac system [71] and Weyl semimetal TaP [72] or T^2-behavior in Sr$_{3-x}$SnO [73]. Note the relaxation of $I = 1/2$ nuclear spin at ^{207}Pb does not have the direct phonon process which gives rise to T^7 or T^9 dependence. Indirect phonon contribution via spin-orbit coupling is negligible [118].

Numerical calculation of T_1^{-1} supports the presence of 3D Dirac electrons in Sr$_3$PbO. Using Sommerfeld expansion for DOS of massless 3D Dirac electrons $D(E) \propto E^2$, T_1^{-1} can be given by Eq.1.68, where the competition between chemical potential μ and temperature T leads to a crossover from T-linear to T^3 and then T^5 behavior with increasing T. T-linear T_1^{-1} is expected at low temperature where $k_B T \ll \mu$ is satisfied. At higher temperature where $k_B T$ is not negligibly small as compared with μ and therefore thermal excitation can significantly contribute to T_1^{-1}, T_1^{-1} shows T^3- and then T^5- behavior reflecting the E^2 dependence of $D(E)$. As seen in Fig. 4.6, Eq.1.68 with $\mu = -60$ meV gives good agreement with the experimentally observed T_1^{-1}, which provides microscopic evidence for the presence of 3D Dirac electrons in Sr$_3$PbO. Note mass gap $\Delta \sim 10$ meV can be neglected in the calculation of T_1^{-1} for $\mu = -60$ meV as μ^2 is much larger than Δ^2 in $D(\mu)$ of Eq.1.20.

In summary, Sr$_3$PbO shows unconventional magnetotransport properties by extremely light mass carriers. The DOS of 3D Dirac electrons is reflected in unconventional temperature dependence of T_1^{-1}. These results provide the evidence for the presence of 3D Dirac electrons in Sr$_3$PbO. In the following sections, we will report angular dependent magnetotransport, bulk magnetic susceptibility and NMR experiments on Sr$_3$PbO and discuss unconventional physics anticipated in 3D Dirac electrons, chiral anomaly and giant orbital diamagnetism, though the angular dependent measurements have difficulty owing to the current jetting effects.

4.3. Chiral anomaly & current jetting effect

As reported in the master thesis [132], the single crystal of Sr_3PbO shows negative longitudinal MR, while the results indicate the presence of the current jetting effects. As seen in Fig. 4.4 (c), Sr_3PbO exhibits a large transverse MR ratio $\Delta\rho_{xx}(B)/\rho_{xx}(0)$ of over ~ 10 at 14 T, which can induce anisotropy of MR and hence the focusing of the current density.
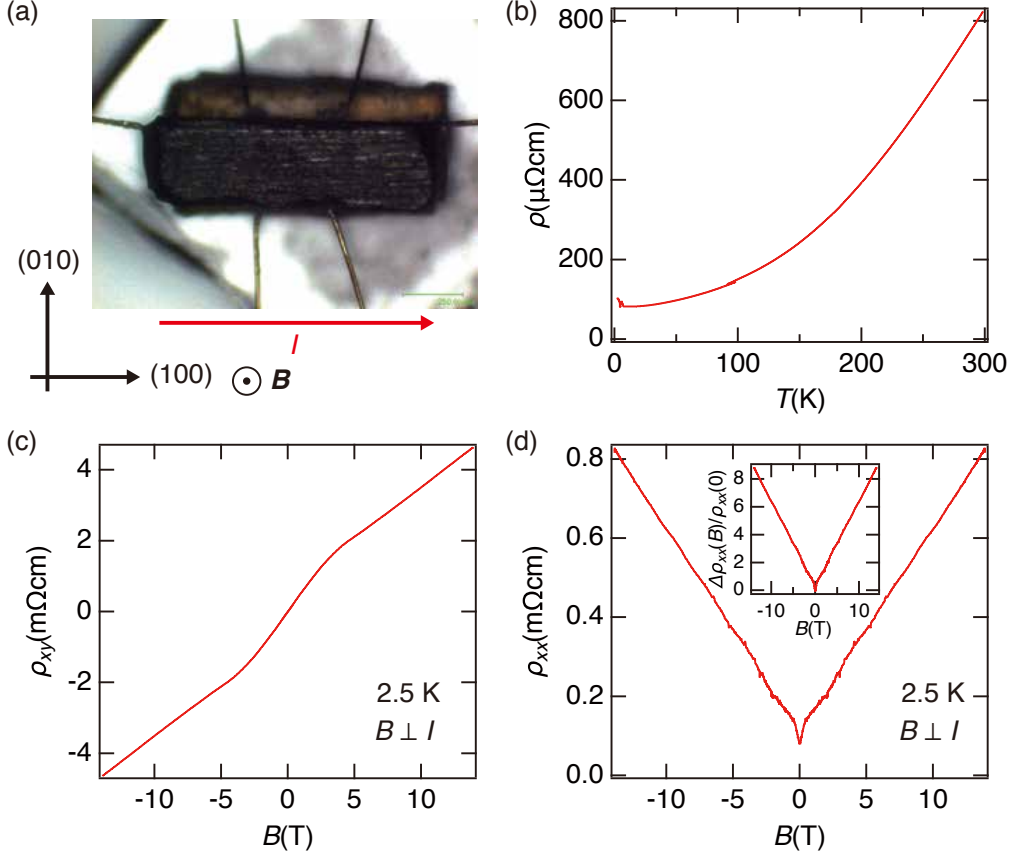

Fig. 4.7. (a) The geometry of a Sr_3PbO single crystal for resistivity, Hall resistivity and transverse MR experiments. The applied current along the (100) axis is normal to magnetic field along the (001) axis. (b) Temperature dependence of the resistivity shows metallic behavior with RRR of ~ 10. Small anomaly at low temperature indicates filamentary superconductivity (see Appendix B). (c) Field dependence of the Hall resistivity $\rho_{xy}(B)$ at 2.5 K in the zero field limit gives a positive Hall coefficient $R_H = 5.2$ cm^3/C, yielding a low hole density $n = 1.2 \times 10^{18}$ cm^{-3}. (d) Field dependence of the resistivity $\rho_{xx}(B)$ at 2.5 K shows B-linear behavior, where a large MR ratio $\Delta\rho_{xx}(B)/\rho_{xx}(0)$ of ~ 9 at $B = 14$ T was observed as seen in the inset.
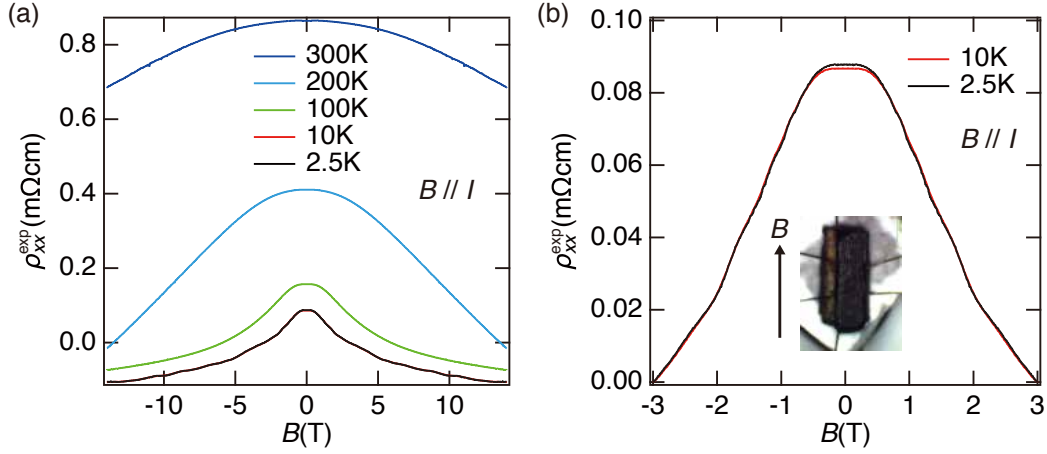
Fig. 4.8. (a) Field dependence of longitudinal MR ($B//I$). $\rho_{xx}^{\mathrm{exp}}(B)$ decreases with increasing B and shows 'negative resistance' at high field and at low temperature. $\rho_{xx}^{\mathrm{exp}}(B)$ at low field and at low temperature is emphasized in (b).

In this section, we report angle dependent magnetotransport measurements to discuss the effect of current jetting. In these experiments, crystallographic axis was determined by a single crystal X-ray diffraction experiment, and then a single crystal was polished into a rectangular shape the surfaces of which are (100) or equivalent planes as shown in Fig. 4.7 (a). Broad current contacts were attached to the sample in order to diminish the artifacts from the current jetting effects. Current is applied along (100) axis of the single crystal. Although a six probe configuration was prepared, one voltage contact was broken probably because of chemical instability of Sr$_3$PbO. We could not cross-check results using two independent voltage pairs.

4.3.1. Hall resistivity & Transverse MR

The single crystal was characterized by the resistivity, the Hall resistivity and the transverse MR with applied field along the (001) axis normal to the current (Fig. 4.7), all of which are similar to the previous results. The resistivity ρ_{xx} shows metallic behavior with RRR of ~ 10. The Hall resistivity $\rho_{xy}(B)$ at 2.5 K in the zero field limit gives a positive Hall coefficient $R_H = 5.18$ cm^3/C, yielding a low density of holes $n = 1.2 \times 10^{18}$ cm^{-3}. A large MR ratio $\Delta\rho_{xx}(B)/\rho_{xx}(0)$ of ~ 9 was observed at $T = 2.5$ K and $B = 14$ T as seen in the inset to Fig. 4.7 (d).

4.3.2. Longitudinal MR

Longitudinal MR with the applied field parallel to the current decreases with increasing field
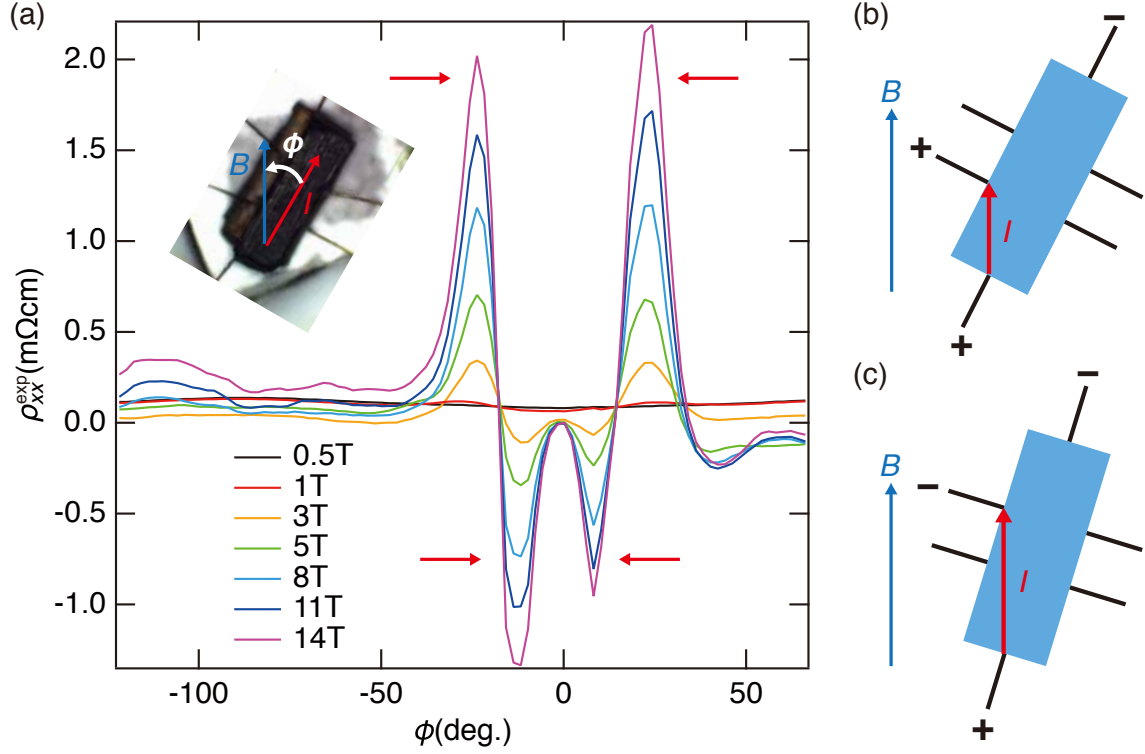
Fig. 4.9. (a) φ-dependence of ρ_{xx}^{exp} at 2.5 K by in-plane rotation shows anomalous peak structure with two peaks and two dips (red arrows), which indicates the presence of the current jetting effects. The angle φ is defined as in the inset. (b) and (c) The peaks or the dips observed in ρ_{xx}^{exp} can be intuitively explained by the alignment of a current contact and a voltage contact along B. The current density concentrates on the voltage contacts because of the anisotropy of MR.

B (Fig. 4.8), consistent with the expected negative longitudinal MR induced by chiral anomaly. However, 'negative resistance' was observed at low temperature and at high field, for example, at 2.5 K and $B > 3$ T. Since a B-symmetric part is presented as $\rho_{xx}^{\mathrm{exp}}(B)$ in Fig. 4.8, the observed 'negative resistance' is not simply explained by contribution from $\rho_{xy}(B)$. These results indicate that current jetting effects play important role in the longitudinal MR [103, 104].

4.3.3. Angular dependence of MR

In order to study the possible chiral anomaly and the current jetting effects further, we measured φ-dependence of ρ_{xx}^{exp} by in-plane rotation where the angle φ is defined as in the inset to Fig. 4.9 (a). The angle dependence of MR exhibits anomalous peak structure with two peaks and two dips (red arrows in Fig. 4.9 (a)). The peaks structure develops with increasing B, namely with increasing the anisotropy of MR. The current jetting effects induced by such
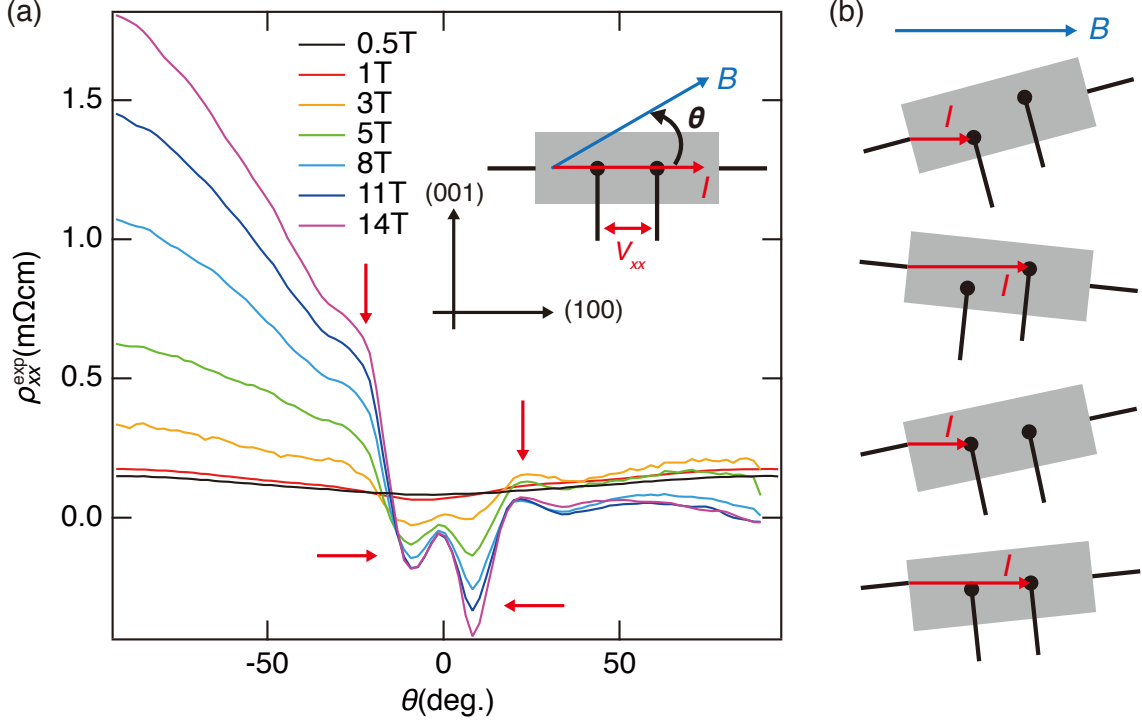
Fig. 4.10. (a) θ-dependence of ρ_{xx}^{exp} at 2.5 K by out-of-plane rotation has two peaks and two dips indicated by the red arrows. The inset is a side view of the sample with the tilt angle θ. (b) The peaks and the dips may be ascribed to misalignment of current and voltage contacts which can give rise to the focusing of the current density on the voltage contacts at finite θ.

enhanced anisotropy of MR can reasonably explain the experimentally observed negative MR if the field is slightly misaligned from the current direction, as discussed in a previous report [104]. When the positive current contact and the positive voltage contact are aligned along the magnetic field direction, focusing of the current density on the voltage contact gives rise to the peak of ρ_{xx}^{exp} (Fig. 4.9 (b)). The dips can be also explained by a similar arrangement of current and voltage contacts with opposite signs as shown in Fig. 4.9 (c). The magnitude of the peaks are larger than that of the dips, which can be described by the shorter distance between the aligned current and voltage contacts. These current jet angles are expected to be dependent on geometry of the attached contacts rather than the field intensity. Indeed, the peak (dip) positions φ_{peak} (φ_{dip}) are almost independent of B and consistent with the contacts geometry where $\varphi_{\text{peak}} \sim \pm 25°$ and $\varphi_{\text{dip}} \sim \pm 12.5°$ are estimated. Similar peaks were also observed in out-of-plane rotation measurements at high field where the angle θ is defined as in the inset to Fig. 4.10 (a). This can be ascribed to small misalignment of the contacts along (001) axis (Fig. 4.10 (b)) as discussed in a previous report [104].

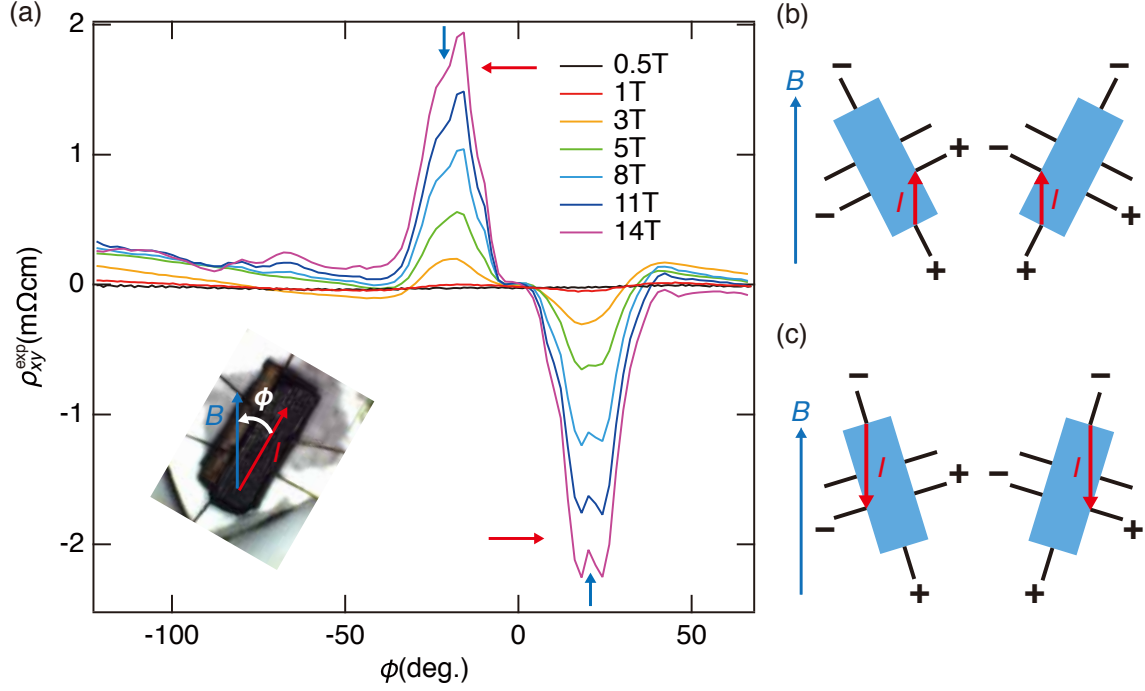The current jetting effects, in conjunction with small misalignment of magnetic field, can

Fig. 4.11. (a) φ-dependence of ρ_{xy}^{exp} at 2.5 K shows a large positive peak and a large negative peak (red arrows), each of which has a small dip (blue arrows). The angle φ is defined as in the inset. (b) The peaks observed in ρ_{xy}^{exp} can be attributed to the focusing of the current density, similar to the φ-dependence of ρ_{xx}^{exp}. The anti-symmetric pattern of the peaks can be explained by the geometry of the electrodes. (c) The alignment of the current and voltage contacts with longer distance may give rise to the small dips in the peaks.

decrease ρ_{xx}^{exp} as seen in Fig. 4.9 (a), which can be observed as the negative longitudinal MR. This suggests that special care is necessary for the longitudinal MR experiments as discussed in previous reports [103, 104]. The focusing of the current density can be recognized as peak structure in angular dependence of ρ_{xx}^{exp}, which helps us to distinguish intrinsic contribution from the artifacts caused by the current jetting effects.

4.3.4. Angular dependence of planar Hall effect

Field angle φ-dependence of planar Hall effect is expected to show $\cos\varphi\sin\varphi \propto \sin 2\varphi$ variation [106, 107] as discussed in 1.4.8. Because the planar Hall effect is even in magnetic field B unlike usual Hall effect, experimentally obtained $\rho_{xy}^{\text{exp}}(B)$ in Fig. 4.11 (a) was inferred from a B-symmetric part of Hall voltage $\left(V_{xy}(B) + V_{xy}(-B)\right)/2$. The field angle φ-dependence of $\rho_{xy}^{\text{exp}}(B)$ at 2.5 K shows a large positive peak and a large negative peak (red arrow in Fig. 4.11 (a)), which is different from the theoretical $\sin 2\varphi$ variation. The magnitude of the peaks increases with increasing B, and the peak positions are almost independent of B. Those can be

Data	l_{tot}(µm)	l_{c}(µm)	w(µm)	t(µm)
Fig. 4.3-Fig. 4.5	652	271	236	225
Fig. 4.7-Fig. 4.13 (a)	1144	226	293	286
Fig. 4.13 (b)	1137	333	224	279

Table 4.1. The dimensions of the crystals investigated in Section 4.2 and Section 4.3. l_{tot}, l_{c}, w and t are the total length, the distance between voltage contacts, the width and the thickness, respectively. The sample in Fig. 4.7-Fig. 4.13 (a) was again used for a remeasurement (Fig. 4.13 (b)) after polishing the surfaces and preparing contacts.
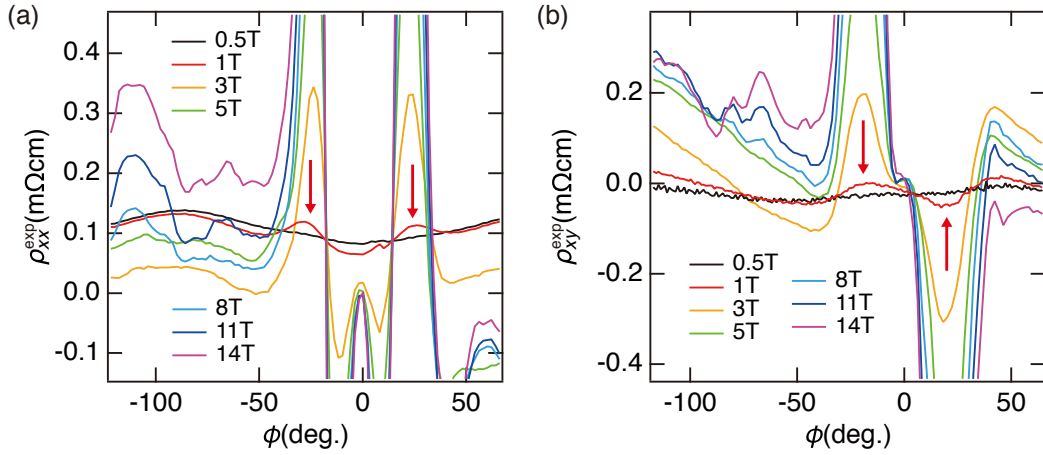

Fig. 4.12. (a) and (b) φ-dependence of ρ_{xx}^{exp} and ρ_{xy}^{exp} shown in Fig. 4.9 (a) and Fig. 4.11 (a) are enlarged to emphasize the low field behavior. The peaks can be recognized at least $B = 1$ T as denoted by the red arrows.

explained by the current jetting effects, similar to the peak structure in ρ_{xx}^{exp}. The anti-symmetric pattern of the peaks is consistent with the geometry of voltage contacts with opposite signs as shown in Fig. 4.11 (b). Each peak has a small dip (blue arrows in Fig. 4.11 (a)) which may be attributed to the alignment of the electrodes with longer distance (Fig. 4.11 (c)).

4.3.5. Possibility of chiral anomaly

Although a small anisotropy of MR $A \sim 2$ is expected at $B = 1$ T in the absence of the negative longitudinal MR, the current jetting effects are clearly recognized in $\rho_{xx}^{\text{exp}}(B)$ and $\rho_{xy}^{\text{exp}}(B)$ at 1 T as seen in Fig. 4.12. The MR anisotropy of A effectively shortens the sample by a factor of $\sqrt{A}$ in the direction of B [104], which modifies a suitable aspect ratio l_{tot}/w (l_{tot}/t) for homogeneous current density by a factor of $\sqrt{A}$. An effective aspect ratio of the sample used in these measurements for $A = 2$ is $l_{\text{tot}}/(w\sqrt{A}) \sim 2.8$ (Table 4.1). This is comparable
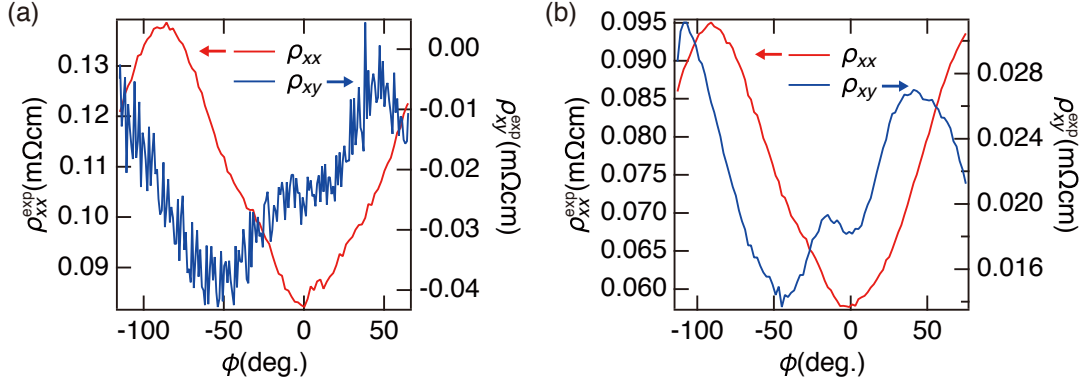
Fig. 4.13. (a) The phase difference between ρ_{xx}^{exp} and ρ_{xy}^{exp} at 0.5 T is $\sim -45°$, which is incompatible with the angular dependences of negative longitudinal MR and planar Hall effect. (b) After the sample surfaces were polished and electrodes were prepared again, similar φ-dependence with lower noise was obtained. However, the magnitudes of $\rho_{xx}^{\mathrm{exp}}(B)$ and $\rho_{xy}^{\mathrm{exp}}(B)$ are different in spite of the measurement for the same sample.

to an aspect ratio of ~ 2.9 for the sample investigated in Section 4.2, where the results for the two independent voltage pairs were consistent with each other and therefore a homogeneous current distribution was expected. These results imply that the anisotropy of MR may be further enhanced by negative longitudinal MR.

The intrinsic contribution may be captured by $\rho_{xx}^{\mathrm{exp}}(B)$ at a low field of $B = 0.5$ T. In Fig. 4.13 (a), clear peaks cannot be recognized at the current jet angles seen at higher fields. We observe $-\cos\bigl(2(\varphi + \alpha)\bigr)$ dependence of $\rho_{xy}^{\mathrm{exp}}(B)$ except for the dip structure at $\varphi = 0°$. This should be compared with $-\cos 2\varphi$ dependence of $\rho_{xx}^{\mathrm{exp}}(B)$. Similar results with lower noise were obtained in a remeasurement for the same sample as shown in Fig. 4.13 (b). The observed period of $\sim 180°$ in $\rho_{xy}^{\mathrm{exp}}(B)$ cannot be explained by the period of 360° for usual Hall effect. The phase difference $\alpha \sim -45°$ between $\rho_{xx}^{\mathrm{exp}}(B)$ and $\rho_{xy}^{\mathrm{exp}}(B)$ is, however, incompatible with 45° expected for the angular dependences of negative longitudinal MR and planar Hall effect, which suggests that the observed angular variation of $\rho_{xy}^{\mathrm{exp}}(B)$ is related to current jetting or other effects. $B = 0.5$ T seems too small for the quantum limit where chiral anomaly is expected. The magnitudes of $\rho_{xx}^{\mathrm{exp}}(B)$ and $\rho_{xy}^{\mathrm{exp}}(B)$ from the same samples in Fig. 4.13 (a) and (b) are different, which may be caused by the current jetting effects. Considering these difficulties, cross-check between two independent voltage pairs and reproducibility in other samples are necessary to discuss the angular dependences of negative longitudinal MR and planar Hall effect in more detail. Further experiments are left for future study to extract clear conclusion.

4.4. Giant orbital diamagnetism of Dirac electrons

 In this section, we report bulk magnetic susceptibility and ^{207}Pb NMR study on the five Sr$_3$PbO samples A-E with different carrier densities from $\sim 10^{18}$ cm^{-3} to $\sim 10^{20}$ cm^{-3} as shown in Fig. 4.1. Band structure, carrier density, DOS and bulk magnetic susceptibility χ_{calc} were calculated by our collaborators, T. Kariyado and M. Ogata. The magnitude of T_1^{-1} is well scaled by the DOS obtained by the band calculation. This enables us to resolve NMR Knight shift K into spin and orbital contributions with the help of a Korringa relation, which demonstrated the orbital character of the giant diamagnetism of Dirac electrons in Sr$_3$PbO.

4.4.1. Bulk magnetic susceptibility

The bulk magnetic susceptibilities χ_{exp} for the three samples A, C and E are found to be diamagnetic as shown in Fig. 4.14 (a). The magnitude of diamagnetic susceptibility is increased on going from the sample E to A, namely approaching the Dirac mass gap. The increase is particularly significant from C to A, as large as of the order of 10^{-4} emu/mol.

The increase is hard to be ascribed to a suppression of spin susceptibility with decreasing hole concentration. The observed increases seems to be comparable to or even larger than typical Pauli paramagnetism χ_{spin} of $\sim 10^{-4}$-10^{-5} emu/mol assuming carrier density $\sim 10^{22}$ cm^{-3} and with $g = 2$ for a conventional metal. The spin susceptibility for low carrier density $\sim 10^{20}$ cm^{-3} is expected to be much smaller than typical χ_{spin} for the conventional metal. We can easily exclude the variation of core diamagnetism. $\sim 1\%$ of cation defects or excess oxygens gives a variation of diamagnetism of $\sim 10^{-6}$ emu/mol as the core diamagnetism is of the order of only 10^{-4} emu/mol for Sr$_3$PbO. The large diamagnetism of the sample A can be attributed to the orbital diamagnetism of Dirac electrons.

Indeed, the theoretical calculation of bulk susceptibility based on a tight binding model supports the emergence of large orbital diamagnetism near the Dirac mass gap. In the Dirac bands regime in Fig. 4.2 (a), the diamagnetism grows and reaches a negative minimum with approaching the Dirac mass gap (Fig. 4.14 (b)). At the chemical potential of ~ -50 meV for the sample A, clear diamagnetic contribution of -1×10^{-4} emu/mol is expected. The diamagnetic susceptibility χ_{exp} is increased upon cooling, consistent with a downward trend of χ_{calc} for $n = 1.6 \times 10^{18}$ cm^{-3} down to 200 K (Fig. 4.14 (c)). An upturn at ~ 200 K is attributed to T-dependence of chemical potential μ (Fig. 4.15), which cannot be recognized in χ_{exp} except for that from impurity. This suggests the chemical potential seems to be less dependent on T than in the calculation. The unconventional μ- and T- dependences are dominated by the orbital diamagnetism as seen in Fig. 4.14 (d) and (e), which display each contribution inχ_{calc}, Pauli paramagnetism (Zeeman), orbital diamagnetism from itinerant motion (orbital), their coupling (cross) and atomic diamagnetism (atomic) as a function of chemical potential or
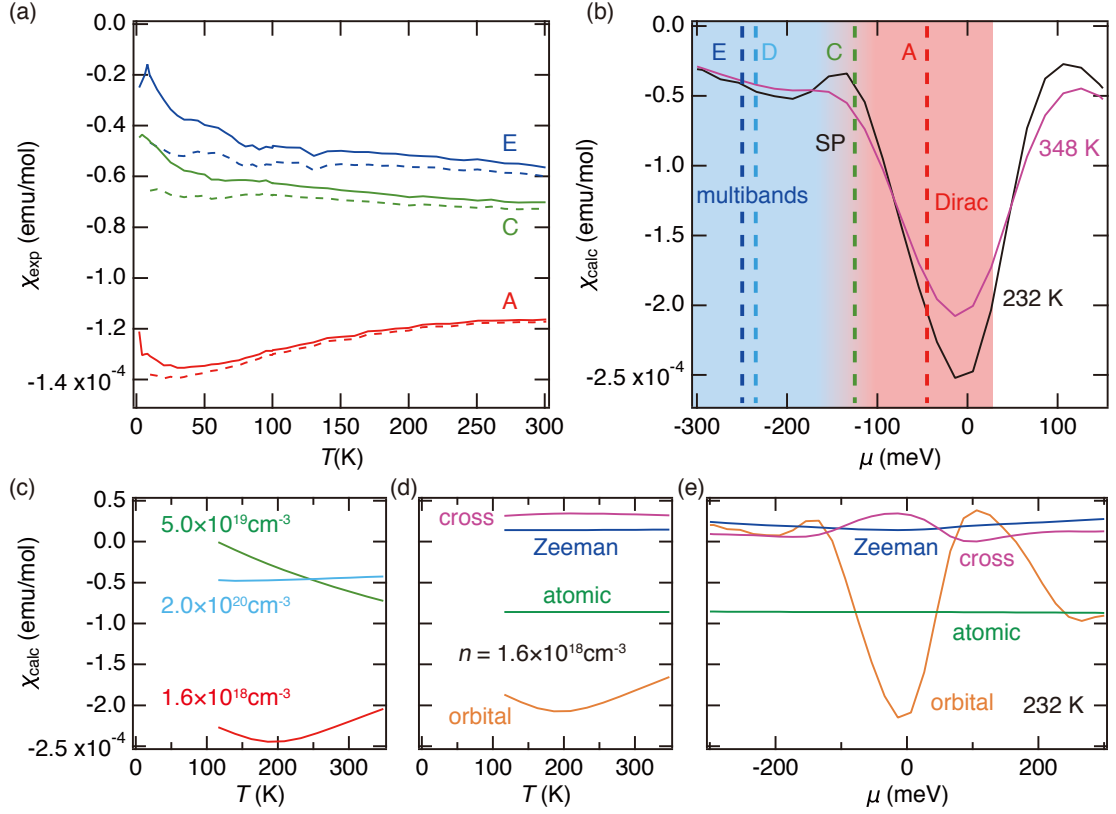
Fig. 4.14. Bulk magnetic susceptibility of Sr_3PbO antiperovskite. (a) Temperature dependence of experimental bulk magnetic susceptibility χ_{exp} for the samples A, C and E (solid lines). All are found to be diamagnetic. The magnitude of diamagnetic susceptibility increases with approaching the Dirac mass gap, consistent with the giant orbital diamagnetism of Dirac electrons. By subtracting Curie-like contributions derived from the fit to χ_{exp} at low temperature, the intrinsic contributions of χ_{exp} were obtained (dotted lines). (b) In response to the band structure near the chemical potential μ in Fig. 4.2 (a), theoretical calculation of chemical potential μ-dependence of bulk magnetic susceptibility χ_{calc} at 232 K and 348 K can be classified into three regimes: giant orbital diamagnetism in the Dirac bands, paramagnetic peak at the SP, temperature independent susceptibility for multi-bands. The corresponding μ for the samples A and C-E are indicated by the dashed lines. (c) Temperature dependence of χ_{calc} for the carrier density $n = 1.6 \times 10^{18}$, 5.0×10^{19} and 2.0×10^{20} cm^{-3}. (d) and (e) Each contribution to χ_{calc} from Pauli paramagnetism (Zeeman), orbital diamagnetism from itinerant motion (orbital), their coupling (cross) and atomic diamagnetism (atomic) as a function of T and μ. T-dependence of χ_{calc} for $n = 1.6 \times 10^{18}$ cm^{-3} and μ-dependence of χ_{calc} at 232 K are dominated by the orbital contribution.

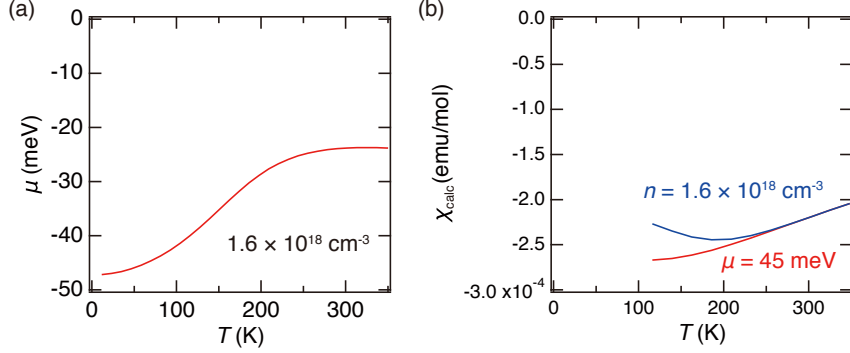temperature. The T-dependence of the orbital diamagnetism allows us to estimate a hyperfine

Fig. 4.15. (a) The chemical potential μ for carrier density $n = 1.6 \times 10^{18}$ cm^{-3} is expected to be dependent on T. (b) The calculated magnetic susceptibility χ_{calc} for fixed $\mu = -45$ meV (red line) monotonically decreases upon cooling and does not show the upturn unlike χ_{calc} for $n = 1.6 \times 10^{18}$ cm^{-3} with T-dependent μ (blue line). The upturn was not observed in χ_{exp} for the sample A, which suggests μ seems to be less dependent on T than the calculation in (a).

coupling constant for orbital Knight shift. Note the atomic diamagnetism in χ_{calc} does not include contribution from core states, which are not taken into account in the tight binding model.

As the chemical potential moves towards the valence band, the calculated magnetic susceptibility χ_{calc} can be classified into three regimes, in response to the character of the band structure near the chemical potential μ as discussed in 4.1.2. The most prominent feature is the giant orbital diamagnetism in the Dirac bands regime as discussed above. At the SP, magnetic breakdown of classical electronic orbits gives rise to quantum tunneling paths enclosed the SP [156], yielding a paramagnetic peak as in Fig. 4.14 (b). Such paramagnetic behavior in χ_{calc} for $n = 5.0 \times 10^{19}$ cm^{-3} (Fig. 4.14 (c)) cannot be found in χ_{exp} of the sample C, which suggests its chemical potential μ shifts from the SP. As will be discussed later, the good agreement between the estimated chemical potential in 4.1.2 and the magnitude of T_1^{-1} indicates such deviation is limited to only the vicinity of the SP. In the multi-bands regime where the orbital contribution is diminishingly small, χ_{calc} for $n = 2.0 \times 10^{20}$ cm^{-3} is almost independent of T as expected for a usual metal, which may explain weakly T-dependent χ_{exp} for the sample E.

4.4.2. Giant diamagnetism in NMR Knight shift

In order to identify the origin of the large diamagnetism observed in χ_{exp}, ^{207}Pb NMR experiments for the samples A-E with different carrier concentrations $\sim 10^{18}$-10^{20} cm^{-3} were conducted. As seen in NMR spectra at 150 K shown in Fig. 4.16 (a), the peak positions systematically shift as a function of chemical potential μ, which suggests these NMR peaks originate
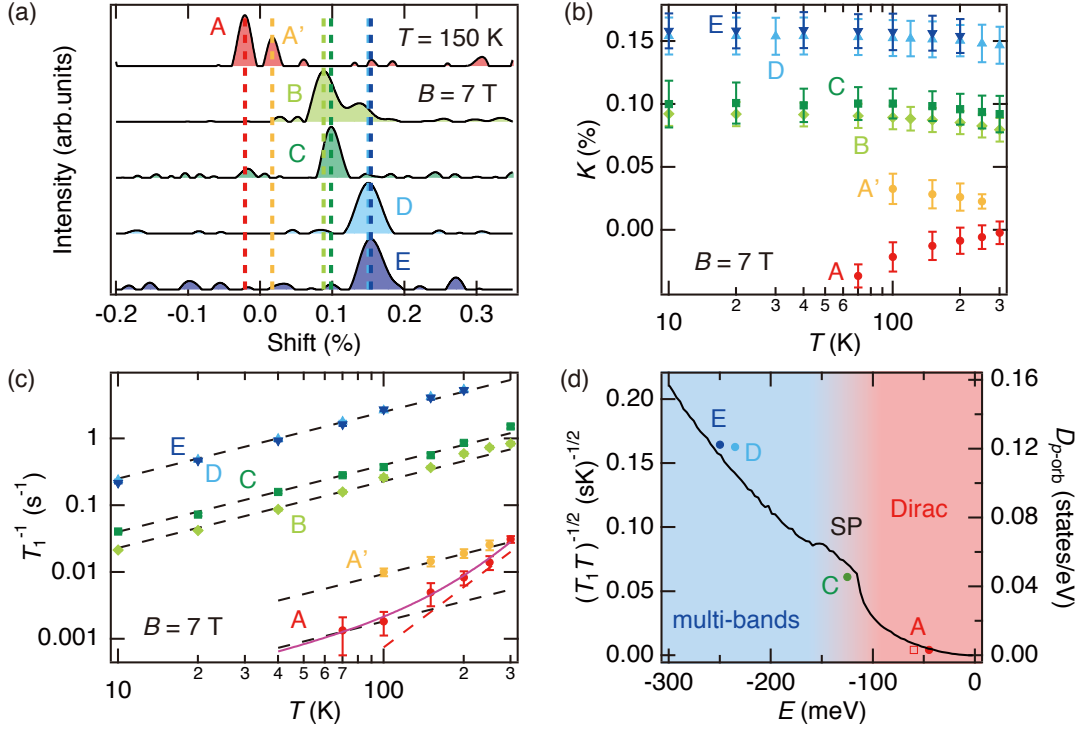
Fig. 4.16. NMR spectra, Knight shift and spin lattice relaxation rate of Sr_3PbO antiperovs-kite. (a) The peak position of NMR spectra for the samples A-E at 150 K systematically shifts toward a negative side with decreasing chemical potential μ. (b) NMR Knight shift K shows similar T- and μ- dependence to χ_{exp}. (c) T-dependence of T_1^{-1} for the sample A-E in Fig. 4.6 is again presented. The T-linear Korringa behavior (black dashed lines) was observed in all the samples in the low temperature limit. The magnitude of T_1^{-1} systematically increases with increasing carrier density. (d) $(T_1 T)^{-1/2}$ for the samples A-E at 100 K (closed circles) are well scaled by the calculated partial DOS for p orbital of Pb (line), which indicates that $(T_1 T)^{-1/2}$ is regarded as the DOS and therefore the spin contribution K_{spin}. The $\mu = -60$ meV inferred from the T-dependence of T_1^{-1} for the sample A is also consistent with the calculated DOS.

from the bulk Sr_3PbO. We note that the observed shift values are different from those of possible impurity phases such as $1.081\%, -0.034\%$ and 0.444% for metallic Pb, PbO and PbO_2 [124] respectively. The presence of more than one peak in samples A and B with low carrier density may be attributed to an inhomogeneity/phase separation where the region(s) with a slightly different hole density from the main phase coexists.

NMR Knight shift K for the samples A-E shows similar behavior to the bulk susceptibility χ_{exp} as seen in Fig. 4.16 (b), where the Knight shift K decreases on going from the sample E to A, namely with approaching the Dirac mass gap. Upon cooling, the sample A shows

a decrease of K while the samples B-E show an increase. The scaling of K with χ_{exp} indicates that the chemical potential and temperature dependence of χ_{exp} are understood by K with a positive hyperfine coupling constant.

The NMR Knight shift K is comprised of several contributions as

$$K(T,n) = K_{\text{chem}} + K_{\text{spin}}(T,n) + K_{\text{orb}}(T,n), \tag{4.4}$$

essentially the same as the bulk magnetic susceptibility. The chemical shift K_{chem} is characterized by the interatomic distance and hence insensitive to T and μ, which acts as a constant offset in K. K_{spin} and K_{orb} are spin and orbital contributions respectively. Each term is proportional to respective susceptibilities χ_{spin} and χ_{orb} via respective hyperfine coupling constants A_{spin} and A_{orb} as discussed in 1.4.10. A_{spin} and A_{orb} are in principle different. In a conventional system where the orbital contribution is independent of T, the theoretical value of $A_{\text{orb}} = 2\langle r^{-3} \rangle$ for Van Vleck susceptibility is usually used and A_{spin} can be determined by T-dependence of a K versus χ diagram. However, unconventional A_{orb} and temperature dependence are expected for the orbital diamagnetism of Dirac electrons, and therefore we separate spin and orbital contributions by analyzing T- and μ- dependences of χ_{exp}, K and T_1^{-1} with the help of a Korringa relation.

4.4.3. Estimate of the spin contribution from T_1^{-1}

The spin contribution can be captured by the spin lattice relaxation rate T_1^{-1} which is determined by a thermal average of DOS as

$$T_1^{-1} \propto \int D(E)^2 f(E)(1 - f(E)). \tag{4.5}$$

In a simple metal with a constant $D(E)$ as a function of T, T-independent $(T_1 T)^{-1}$ is expected, known as the Korringa law. The T-linear Korringa behavior of T_1^{-1} was observed in all the samples in the low temperature limit (Fig. 4.16 (c)). The magnitude of the T-linear T_1^{-1} systematically increases with increasing hole density from the sample A to E, which can be naturally explained by the increase of the DOS at the chemical potential. Indeed, $(T_1 T)^{-1/2}$ of ^{207}Pb NMR for different carrier density at 100 K are well scaled with the calculated partial DOS of p orbitals of Pb (Fig. 4.16 (d)), which evidences that $(T_1 T)^{-1/2}$ is regarded as the DOS and therefore the spin contribution K_{spin}. The good agreement ensures that the deviation of chemical potential of the sample C mentioned above is very likely limited to the vicinity of the SP at ~ -125 meV. The orbital contribution to T_1^{-1} was theoretically studied [157], which predicted to be 10 times less than observed T_1^{-1} and can be neglected in our results.

An upward deviation from the T-linear Korringa behavior with increasing T was observed in the lowest carrier density sample A above 100 K, while the other samples hold T-linear behavior all the way up to room temperature. The distinct crossover behavior of the sample A can be attributed to the strongly E-dependent DOS of 3D Dirac electrons, which is well reproduced by the numerical calculation for Eq.1.68 with $\mu = -60$ meV as discussed in 4.2.4. Considering the nonlinear behavior of ρ_{xy} and the uncertainty of the band calculation in incorporating various interaction effects, the estimate of $\mu = -60$ meV is very close to the estimate of $\mu = -45$ meV from the hole density. Note $\mu = -60$ meV is still consistent with the energy dependence of the calculated DOS in Fig. 4.16 (d) (open square).

4.4.4. Presence of giant orbital diamagnetism

By establishing $(T_1 T)^{-1}$ as a measure of the DOS and the spin contribution, we can separate the K_{spin} component from the observed K with the help of the Korringa relation. $K_{\text{spin}} \propto D(E)$ is roughly estimated by $(T_1 T)^{-1/2}$ using the Korringa relation $T_1 T K_{\text{spin}}^2 = S$. The Korringa value S depends only on a kind of nuclei in a simple metal and is expressed as $\hbar/(4\pi k_B)(\gamma_e/\gamma_n)^2$ for an isotropic Fermi surface. The separation of NMR peaks in the low carrier density samples A and B (Fig. 4.16 (a)) allows us to measure K and T_1^{-1} for each peak and to avoid the issue of inhomogeneity.

The observed K as a function of $(T_1 T)^{-1/2}$ (Fig. 4.17 (a)) provides evidence for the presence of the giant orbital diamagnetism. K decreases with decreasing $(T_1 T)^{-1/2}$ from the sample E with the highest hole density, much more rapidly than the linear relationship between K_{spin} and $(T_1 T)^{-1/2}$ expected from the Korringa relation (gray dashed line). The rapid decrease beyond the estimated K_{spin} by the Korringa relation can be naturally ascribed to the orbital contribution K_{orb} which grows with approaching the Dirac mass gap and gives dominant contribution for the sample A. Experimental Korringa values S_{exp} are quite often modified by a factor of 2 even in simple metals [124]. $S_{\text{exp}} \sim 6.3S$ (black dashed line in Fig. 4.17 (a)) is not large enough to change our conclusion above. The strongly nonlinear behavior near the Dirac mass gap cannot be explained even if we assume much larger S_{exp}. In general, K_{spin} and $(T_1 T)^{-1}$ are scaled by g factor as $K_{\text{spin}} \propto g^2$ and $T_1^{-1} \propto g^2$, and hence $S \propto g^2$ as discussed in 1.4.11. The good agreement between $(T_1 T)^{-1/2}$ and the calculated DOS $D(E)$ in Fig. 4.16 (d) implies the g factor is insensitive to the hole concentration and therefore very likely not significantly enhanced for the samples investigated.

The unconventional temperature dependence is expected for the giant orbital diamagnetism of Dirac electrons, which enables us to extract the orbital hyperfine coupling constant A_{orb} from K and χ_{exp} with both orbital and spin contributions. After subtracting Curie-like contributions from impurity as shown in Fig. 4.14 (a) (dotted lines), $A_{\text{orb}} = 88 \pm 14$ kOe/μ_{B}
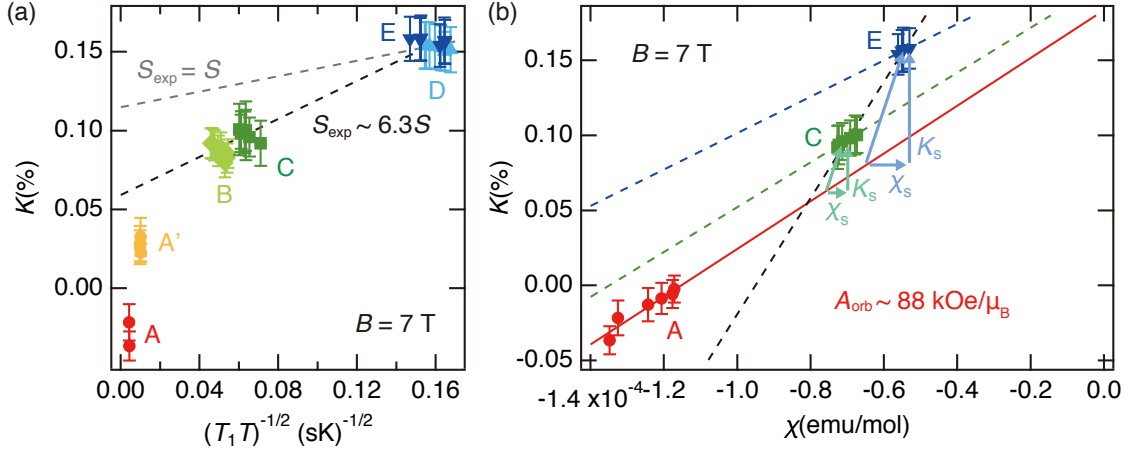
Fig. 4.17. Giant orbital diamagnetism of Dirac electrons in Sr_3PbO antiperovskite. (a) The observed K decreases with decreasing $(T_1T)^{-1/2}$, from the sample E to the sample A, much more rapidly than the linear relationship expected for the Korringa relation (gray dashed line). The nonlinear behavior of K as a function of $(T_1T)^{-1/2}$ cannot be explained by the modified Korringa value of $S_{\mathrm{exp}} \sim 6.3S$ (black dashed line), which provides the evidence for the giant orbital diamagnetism. (b) After subtracting Curie-like contributions from impurity as dotted lines in Fig. 4.14 (a), the orbital hyperfine coupling constant $A_{\mathrm{orb}} = 88 \pm 14$ kOe/μ_B can be extracted from a linear fit to K versus χ_{exp} for the sample A in which the orbital contribution is dominant (red line). An upward deviation of the samples C and E from the red line can be attributed to the spin contributions K_{spin} and χ_{spin}, which can be subtracted, for example, as denoted by the arrows. Here, $A_{\mathrm{spin}} = 450$ kOe/μ_B was used as an example though A_{spin} cannot be determined from our results. The data for $T > 50$ K were presented in the plot because the Curie-like contributions for low temperature cannot be completely removed.

can be derived from a linear fit to a K versus χ_{exp} diagram for the sample A in which the spin contribution is negligibly small (red line in Fig. 4.17 (b)). Here the main peak A was used for the Knight shift K. The slopes obtained by linear fits to K versus χ_{exp} for the sample C and E (green and blue dashed lines in Fig. 4.17 (b)) are similar values to that of the sample A, which suggests the T-dependence even in these samples originates from the orbital contribution. An upward deviation of the samples C and E from the red line can be attributed to the superposition of positive K_{spin}. This requires a positive A_{spin} larger than the A_{orb}. Almost T-independent $K_{\mathrm{spin}} = A_{\mathrm{spin}}\chi_{\mathrm{spin}}$ can be subtracted from the samples C and E, for example, as shown by the arrows in Fig. 4.17 (b). Here, $A_{\mathrm{spin}} = 450$ kOe/μ_B was used as an example though A_{spin} cannot be uniquely determined from our results. K and χ_{exp} for the samples A-E can be reasonably explained by $K_{\mathrm{orb}}(T, \mu) + K_{\mathrm{spin}}(\mu)$ and $\chi_{\mathrm{orb}}(T, \mu) + \chi_{\mathrm{spin}}(\mu)$ including both T- and μ- dependences except for constant offsets K_{chem} and χ_{core}.
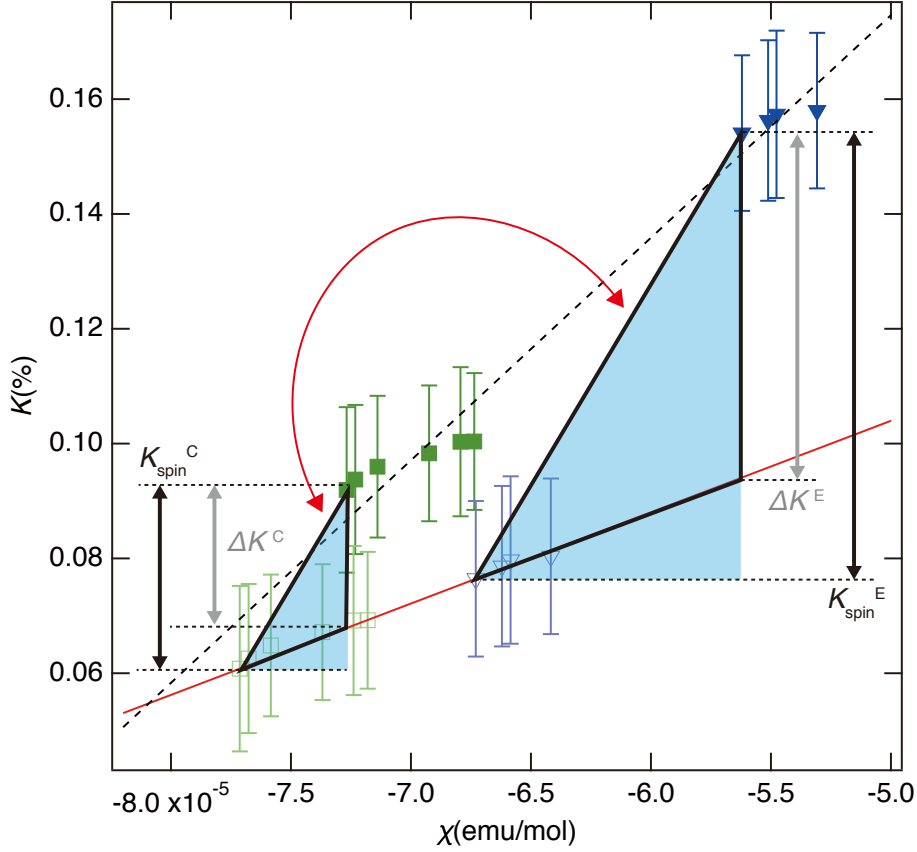
Fig. 4.18. The K versus χ_{exp} diagram for the sample C and E in Fig. 4.17 (b) is enlarged. The open symbols represent K as a function of χ_{exp} after subtracting spin contributions K_{spin} and χ_{spin}, where $A_{\mathrm{spin}} = 450$ kOe/μ_{B} was used as an example. A slope of two parallel lines indicated by red arrows depends on A_{spin}. Because two triangles enclosed by black line and two filled triangles are similar figures for the arbitrary slope, $K_{\mathrm{spin}}^{\mathrm{E}}/K_{\mathrm{spin}}^{\mathrm{C}}$ takes $\Delta K^{\mathrm{E}}/\Delta K^{\mathrm{C}}$ $= 2.4 \pm 0.1$ independent of A_{spin}. This is consistent with the ratio of $(T_1^{\mathrm{E}}T)^{-1/2}/(T_1^{\mathrm{C}}T)^{-1/2}$ $= 2.6 \pm 0.1$, which supports the extracted $A_{\mathrm{orb}} \sim 88$ kOe/μ_{B} in Fig. 4.17 (b).

A_{spin} and hence K_{spin} and χ_{spin} cannot be determined from the above discussion. The ratio of estimated K_{spin}, which is an offset from the red line, between the samples C and E depends on the slope of the red line and therefore A_{orb}. The ratio, however, takes a constant independent of A_{spin} when A_{orb} is fixed (Fig. 4.18). $K_{\mathrm{spin}}^{\mathrm{E}}/K_{\mathrm{spin}}^{\mathrm{C}} = 2.4 \pm 0.1$ was obtained for $A_{\mathrm{orb}} = 88$ kOe/μ_{B}. This is in good agreement with the ratio of $(T_1^{\mathrm{E}}T)^{-1/2}/(T_1^{\mathrm{C}}T)^{-1/2}$ $= 2.6 \pm 0.1$, which is entirely consistent with the Korringa relation and confirms the validity of the extracted $A_{\mathrm{orb}} \sim 88$ kOe/μ_{B} though A_{spin} cannot be determined. Note the parameter ranges of A_{spin} and S_{exp} can be restricted. Assuming the spin contribution dominates the μ-dependence of total K and χ_{spin} in the samples B-E, A_{spin}, K_{spin} and hence S_{exp} can be derived

from a linear fit of these samples (black dashed line in Fig. 4.17 (b)), which yields $A_{\rm spin} \sim 210$ kOe/$\mu_{\rm B}$ and $S_{\rm exp} \sim 6.3S$. If $A_{\rm spin}$ is much larger, $S_{\rm exp}$ approaches $\sim 2.3S$ in the large $A_{\rm spin}$ limit. Those impose the constraints on the parameter ranges as $A_{\rm spin} > \sim 210$ kOe/$\mu_{\rm B}$ and $2.3 < S_{\rm exp}/S < 6.3$.

The estimated $A_{\rm orb} \sim 88$ kOe/$\mu_{\rm B}$ reflects unconventional character of the orbital diamagnetism of Dirac electrons. $A_{\rm orb}$ is scaled by a factor of $2r^{-3}$ and therefore $K_{\rm orb}$ is dominated by electrons close to nuclei. $A_{\rm orb} = 2\langle r^{-3}\rangle$ for conventional Van Vleck susceptibility by localized electrons is estimated to be ~ 2000 kOe/$\mu_{\rm B}$ for $6p$ orbitals of Pb [158, 159]. ^{207}Pb NMR can see only half of total $\chi_{\rm orb}$ as the Dirac bands are formed by $6p$ electrons of Pb^{4-} and $4d$ electrons of Sr^{2+}. $A_{\rm orb} \sim 88$ kOe/$\mu_{\rm B}$ for Sr$_3$PbO is ~ 10 times smalled than that expected from $2\langle r^{-3}\rangle$. This appears to suggest that $6p$ electrons of Pb in charge of the giant orbital diamagnetism is not localized but itinerant and therefore only $\sim 10\%$ of the $6p$ electrons would be close to the nuclei. $K_{\rm orb}$ for the orbital diamagnetism of Dirac electrons was theoretically discussed, which yields $A_{\rm orb} < 1$ kOe/$\mu_{\rm B}$ for uniform orbital current of Dirac electron gas [122]. The much larger $A_{\rm orb} \sim 88$ kOe/$\mu_{\rm B}$ for Sr$_3$PbO suggests the orbital diamagnetism can be attributed to hopping of conduction electrons between the atomic orbitals rather than uniform orbital current.

Note the positive $A_{\rm spin}$ suggests the hyperfine couplings are governed by s electron-like Fermi contact interaction. Although the Dirac bands in Sr$_3$PbO is comprised of p orbitals of Pb^{4-} and d orbitals of Sr^{2+}, sp hybridization or strong spin orbit coupling of Pb [160] can induce s-like character from electrons of p bands as discussed in ^{209}Bi NMR on half-Heusler compounds [161].

Chapter 5
Conclusion

5.1. Summary

In summary, we report the magnetotransport, the bulk magnetic susceptibility and the ^{207}Pb NMR study on the cubic Sr_3PbO antiperovskite, theoretically proposed as a candidate for 3D Dirac electron system. The unconventional magnetotransport properties by extremely light mass carriers and the crossover in NMR spin lattice relaxation rate T_1^{-1} provide the evidence for the presence of 3D Dirac electrons in Sr_3PbO. Those results established Sr_3PbO with $I = 1/2$ nuclear spin at ^{207}Pb as a unique and promising platform for NMR study of giant diamagnetism of Dirac electrons.

The microscopic origin of the giant diamagnetism of Dirac electrons was revealed by the bulk susceptibility and the NMR experiments on the five Sr_3PbO samples with different carrier density of 10^{18}-10^{20} cm^{-3}. The bulk susceptibility χ_{exp} and the NMR Knight shift K show unconventional chemical potential and temperature dependences, consistent with the giant orbital diamagnetism of Dirac electrons. By analyzing χ_{exp}, K and T_1^{-1}, spin and orbital contributions in χ_{exp} and K are successfully separated with the help of the Korringa relation. These results demonstrated the orbital character of the giant diamagnetism of Dirac electrons for the first time.

The field angle dependences of ρ_{xx}^{exp} and ρ_{xy}^{exp} shows anomalous peak structure, which can be attributed to the current jetting effects. Although the intrinsic contribution induced by chiral anomaly may be captured by the negative longitudinal MR and the planar Hall effect at low magnetic field, more detailed experiments will be left for future study to extract clear conclusion.

5.2. Future work

The current jetting effects make the angular dependent magnetotransport experiments difficult. In order to extract clear conclusion, further experiments on Sr_3PbO are necessary. Because the peak (dip) positions in ρ_{xx}^{exp} and ρ_{xy}^{exp} are expected to be dependent on the geometry of the attached contacts, cross-check between independent voltage pairs is useful to distinguish intrinsic contribution from artifacts by the current jetting effects. We are working on

the magnetotransport measurements on different single crystals by a six probe configuration.

Our results provide the evidence for the presence of 3D Dirac electrons in Sr_3PbO, which opens up a material family to control 3D Dirac electrons, to design exotic phases and to explore unconventional physics anticipated in the quantum limit. The anisotropy or mass gap of 3D Dirac electrons can be tuned by other compounds such as Ca_3PbO and Sr_3SnO. Magnetism can be introduced into the antiperovskites by Eu_3PbO and Eu_3SnO, where a magnetic Weyl semimetal phase may be realized.

Appendix A
Characterization by magnetization

In this appendix, results of magnetization measurements for Sr_3PbO synthesized by different conditions are summarized. The sample quality can be roughly characterized by the magnetization which strongly depends on the carrier density as discussed in Section 4.4. The single crystals were grown as written in Section 3.1, which is again presented here.

$$x Sr + PbO \rightarrow Sr_3PbO$$
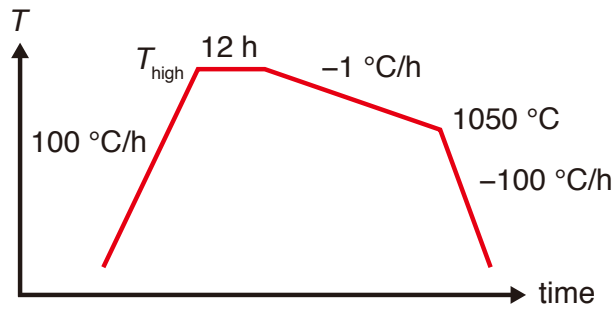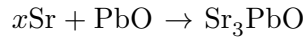
Fig. A.1. Typical temperature sequence for single crystal growth for Sr_3PbO. The highest temperature T_{high} of 1350, 1400 and 1450 °C was used.

Here, a Sr/PbO ratio $x = 3.15$-4.5 and the highest temperature $T_{high} = 1350$-1450 °C were controlled.

A.1. Sr/PbO ratio dependence

The magnetizations M are found to be diamagnetic as shown in Fig. A.2, consistent with χ_{exp} in Section 4.4. The observed diamagnetism basically increases with increasing the Sr/PbO ratio x. The magnitude of diamagnetism grows with decreasing the carrier density, namely approaching the Dirac mass gap. This suggests that low carrier density samples can be obtained by the larger Sr/PbO ratio x.
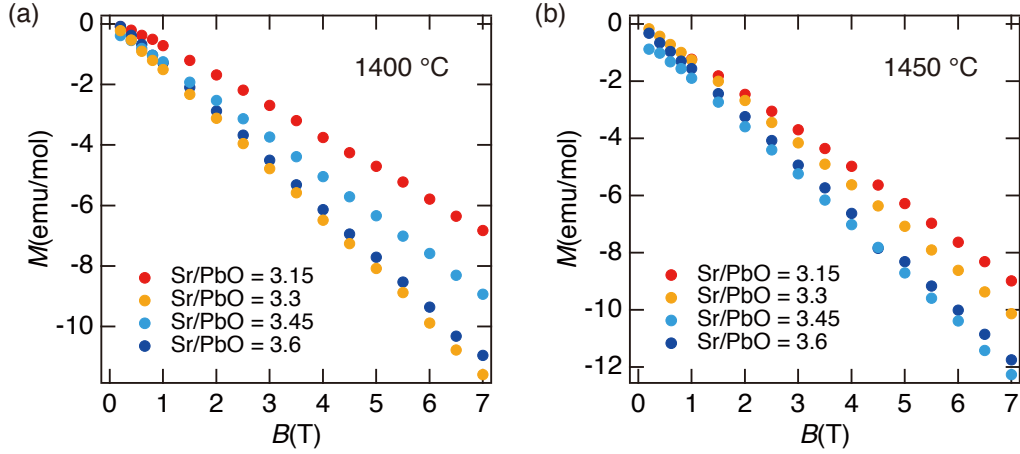
Fig. A.2. Sr/PbO ratio x dependence of magnetization for powder samples of Sr_3PbO. (a) and (b) The magnetization of the powder samples for $T_{high} = 1400$ °C and 1450 °C, respectively. The magnitude of the observed diamagnetism basically increases with increasing x.

A.2. Temperature sequence dependence

The magnitude of the observed diamagnetism for the Sr/PbO ratios $x = 3.15$, 3.3, 3.45 and 3.6 increases with increasing T_{high} as seen in Fig. A.3, which suggests that the higher T_{high} gives samples with lower carrier density.

In summary, the sample quality can be roughly characterized by the magnetization experiments on the samples synthesized by the different conditions. The larger Sr/PbO ratio x and the higher T_{high} are suitable to grow samples with low carrier density. However, there are thresholds for x and T_{high} as mentioned in Section 3.1.
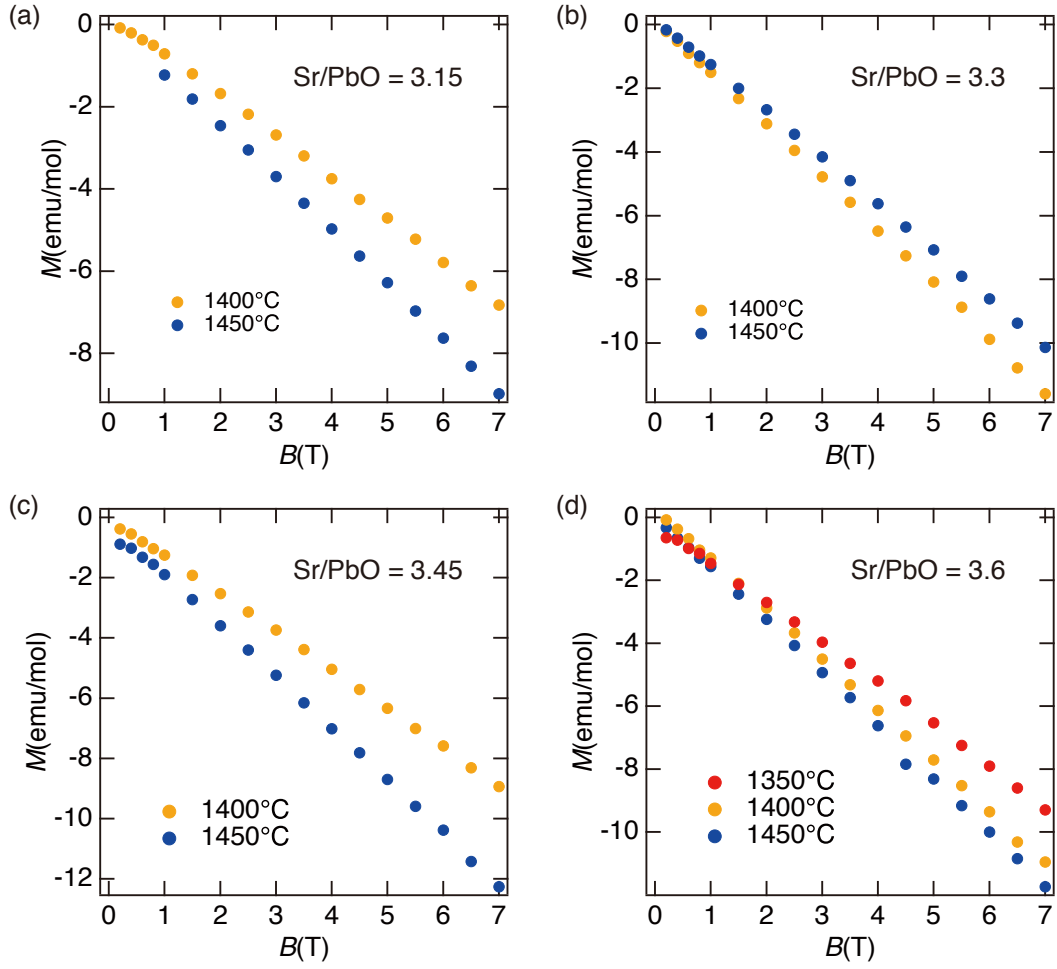
Fig. A.3. The highest temperature T_{high} dependence of magnetization for powder samples of Sr_3PbO. (a-d) The magnetization of the powder samples for the Sr/PbO ratios $x = 3.15$, 3.3, 3.45 and 3.6, respectively. The magnitude of the observed diamagnetism increases with increasing T_{high}.

Appendix B
Absence of bulk superconductivity

In this appendix, superconducting behaviors in the antiperovskites A_3TtO (A = Ca, Sr, Ba; Tt = Sn, Pb) observed in resistivity and bulk magnetic susceptibility experiments are presented. Although bulk superconductivity with the transition temperature $T_c \sim 4$ K in polycrystalline $Sr_{3-x}SnO$ was previously reported [133], bulk superconductivity was never realized in our samples of Sr_3PbO, Sr_3SnO and Ca_3PbO. We conclude that the superconducting behavior observed in the antiperovskites A_3TtO does not relate to the Dirac electrons.

B.1. Filamentary superconductivity in resistivity

The single crystals of Sr_3PbO often showed a resistance drop of $\sim 10\%$ at low temperature, which indicates the filamentary superconductivity. Zero resistance was never observed down to 2 K, which indicates the absence of the bulk superconductivity.
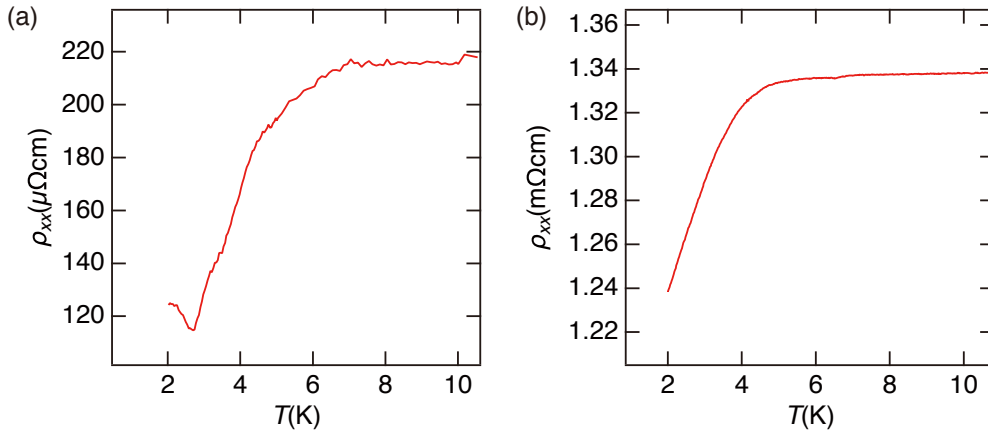
Fig. B.1. Filamentary superconductivity of Sr_3PbO. The sample in (a) was grown as reported previously [136]. The sample in (b) was synthesized inside a BN crucible sealed in a stainless steel tube.

The sample in Fig. B.1 (b) was synthesized as following. Sr and PbO with the ratio of $x = 9$ were put into a BN crucible and then sealed in a stainless steel tube which was further sealed
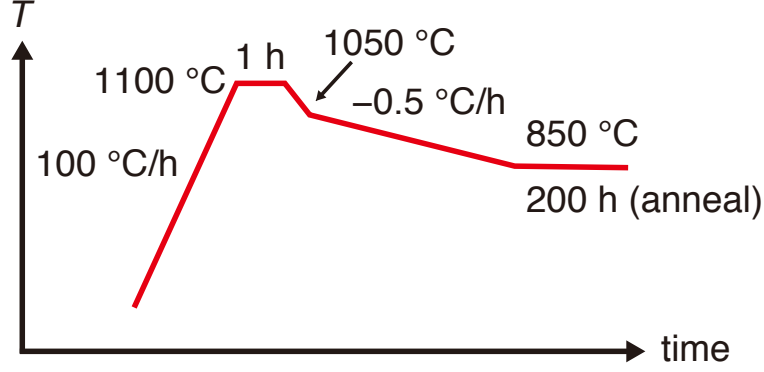
Fig. B.2. Temperature sequence for the sample used in Fig. B.1 (b).

in a quartz tube. Temperature sequence in Fig. B.2 was used. This excludes the possibility of filamentary superconductivity from tantalum impurity ($T_c = 4.5$ K).

B.2. Small diamagnetic volume fraction

Powder samples of Sr_3PbO often showed diamagnetic shielding with transition temperature of ~ 4 K, where small diamagnetic volume fractions at most $\sim 1\%$ were observed (Fig. B.3). The large volume fractions were never obtained in the samples for the carrier density n of 10^{18}-10^{20} cm^{-3} which corresponds to $E_F \sim$ from -50 to -200 meV. Bulk superconductivity was never realized in a wide range of the band structure from the Dirac bands to the multi-bands region in Fig. 4.2 and therefore does not related to the bulk band structure in these regions.

Powder samples of other antiperovskites, Sr_3SnO and Ca_3PbO also showed small diamagnetic shielding as seen in Fig. B.4, indicative of the absence of the bulk superconductivity. Because these antiperovskites do not have common atoms except for O atom, the superconductivity with small volume fraction would not be attributed to metallic Sn or Pb impurities. All Sr_3PbO, Sr_3SnO and Ca_3PbO shows the transition at $T_c \sim 4$ K, which is consistent with the previous report for $Sr_{3-x}SnO$ [133]. This suggests that the small diamagnetic shielding observed in our Sr_3PbO, Sr_3SnO and Ca_3PbO samples has the same origin as $Sr_{3-x}SnO$. Our systematic study including the carrier density dependence of Sr_3PbO demonstrates the absence of the bulk superconductivity E_F down to ~ -200 meV which is well below the Dirac bands. We conclude that the superconducting behavior in the antiperovskites does not relate to the Dirac electrons.
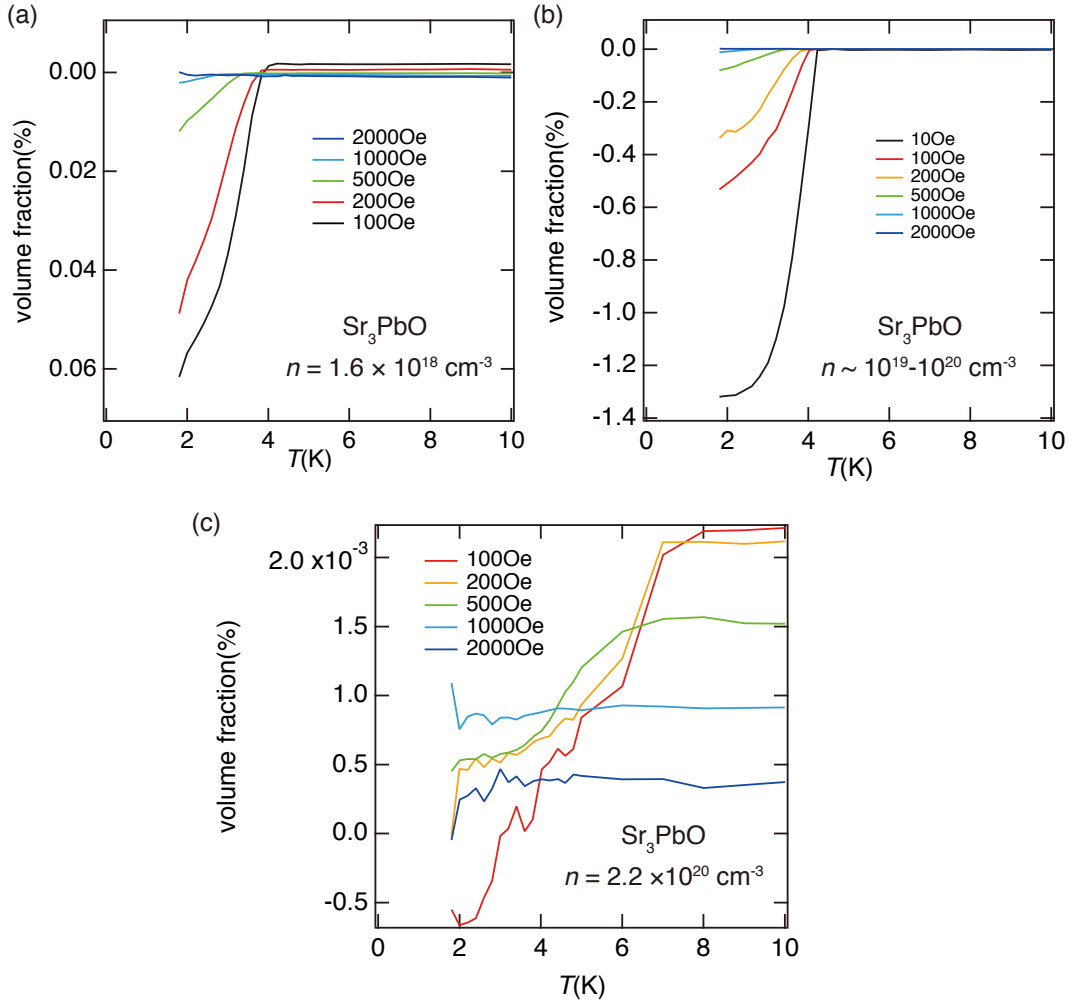
Fig. B.3. (a-c) Diamagnetic volume fractions under zero field cooling for powder samples of Sr_3PbO with carrier density n of 10^{18}-10^{20} cm^{-3}. The carrier density n was determined by Hall resistivity measurements of the single crystals from the same batch as the powder sample. The Hall resistivity measurements for two single crystals from the batch of (b) give $n \sim 10^{19}$ and 10^{20} cm^{-3} respectively, which suggests the inhomogeneity of the carrier density. The observed diamagnetic volume fractions are at most $\sim 1\%$, which indicates the absence of bulk superconductivity.
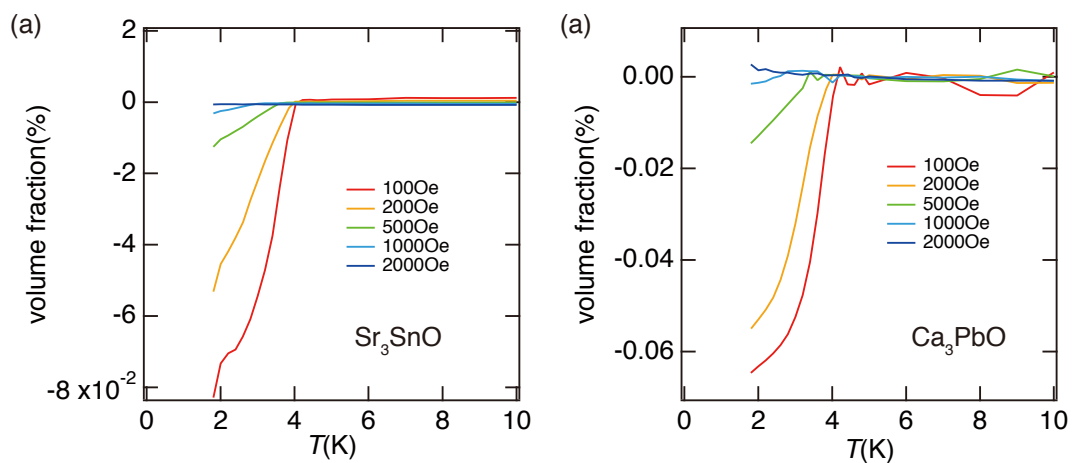
Fig. B.4. (a) and (b) Diamagnetic volume fractions under zero field cooling for powder samples of Sr_3SnO and Ca_3PbO. The observed diamagnetic volume fractions are at most $\sim 0.1\%$ similar to the results for Sr_3PbO, which indicates the absence of bulk superconductivity.

Appendix C
Additional data for angular dependences

In this appendix, the additional data for the angular dependent magnetotransport experiments on Sr_3PbO in Section 4.3 are presented.

C.1. Raw data for angular dependence

Raw data of the φ-dependence of ρ_{xx} in Fig. 4.9 (a) has a large B-antisymmetric part as shown in Fig. C.1, which may be attributed to misalignment of the contacts in conjunction with the focusing of the current density.
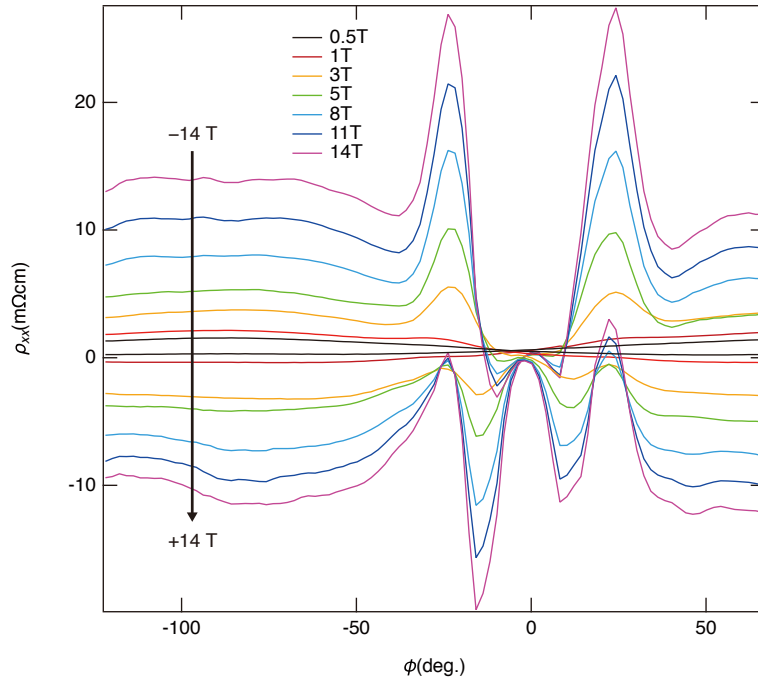
Fig. C.1. Raw data of the φ-dependence of ρ_{xx} in Fig. 4.9 (a).

Raw data of θ-dependence of ρ_{xx} in Fig. 4.10 (a) also has a large B-antisymmetric part as

shown in Fig. C.2. The ρ_{xx} for $\theta = 90°$ at $B = B_0$ and $\theta = -90°$ at $B = -B_0$ is expected to the same. However, large difference for the $\theta = 90°$ at 14 T and $\theta = -90°$ at -14 T is recognized. This may be attributed to the current jetting effects and should be clarified in the future.
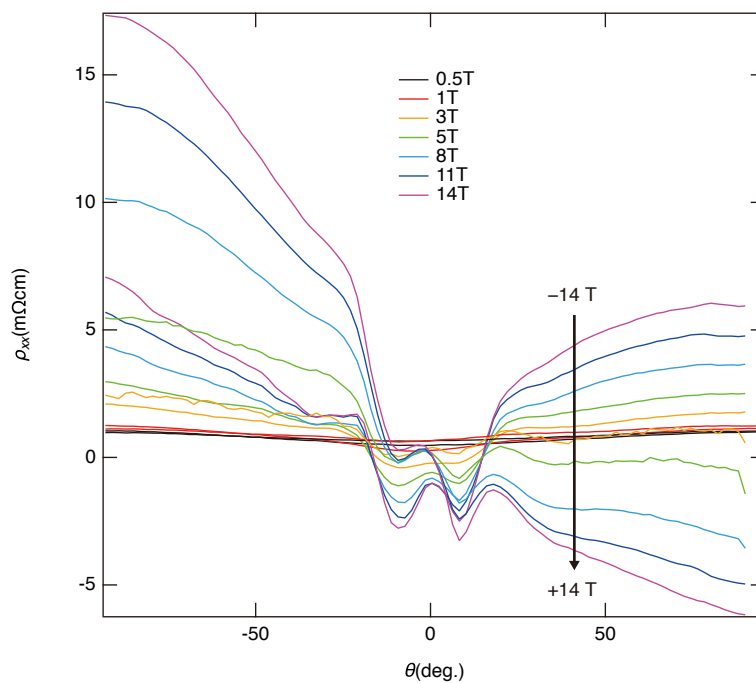
Fig. C.2. Raw data of the θ-dependence of ρ_{xx} in Fig. 4.10 (a).

Appendix D

Additional data for K, T_1^{-1} and χ

In this appendix, the additional data for bulk magnetic susceptibility and NMR experiments on Sr_3PbO in Section 4.4 are presented.

D.1. Field dependence of bulk susceptibility

Bulk magnetic susceptibility χ of the sample A does not show appreciable field dependence from 1 T to 7 T (Fig. D.1) except for a Curie-like increase very likely associated with magnetic impurities at low temperatures below 100 K. A constant offset at 1 T may be attributed to a small amount of magnetic impurity which should give rise to negligibly small contributions at high fields.
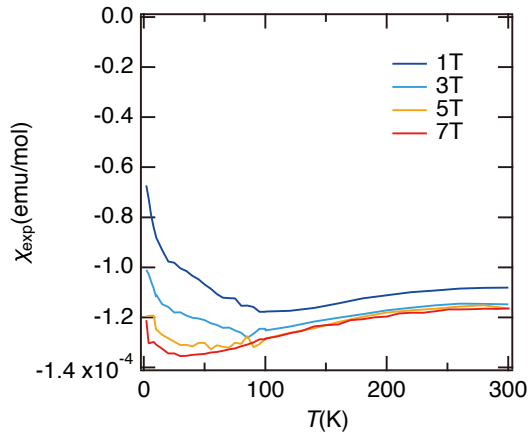
Fig. D.1. Temperature dependence of bulk magnetic susceptibility of the sample A in Fig. 4.14 (a) at 7, 5, 3 and 1 T.

The B-independent χ for the sample A is consistent with B-linear behavior of magnetization M for the several samples in Fig. A.2 and Fig. A.3. M for a sample F, one of these samples, is again presented in Fig. D.2 (a). The sample F shows a large diamagnetism of $\sim -1 \times 10^{-4}$ as
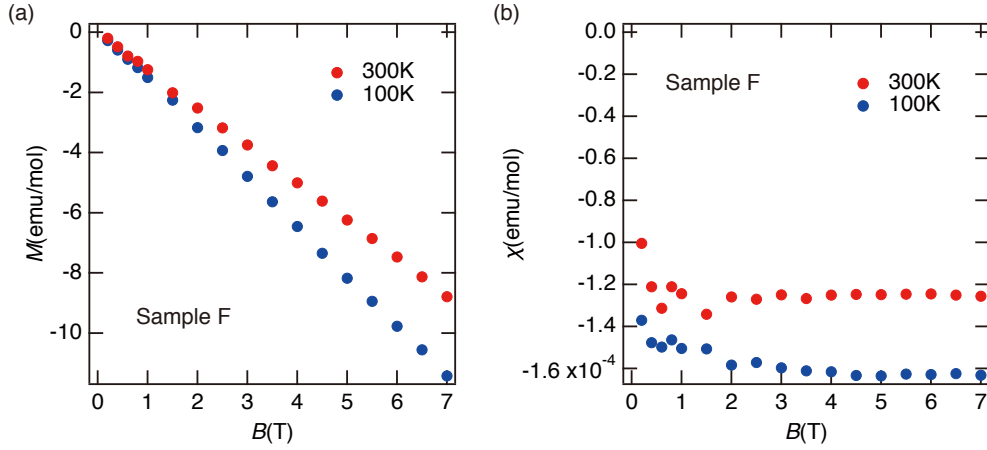
Fig. D.2. Field dependence of magnetization M and magnetic susceptibility χ of a sample F at 100 and 300 K. (a) The magnetization of the sample F shows B-linear behavior. (b) A large diamagnetism of $\sim -1 \times 10^{-4}$ emu/mol was observed in the sample F. The bulk susceptibility χ is almost constant as a function of field, consistent with Fig. D.1.

seen in Fig. D.2 (b), which is indicative of the giant orbital diamagnetism of Dirac electrons. Field independence of bulk susceptibility is better visualized in almost constant χ as a function of field.

D.2. NMR data for other samples

NMR Knight shift K and spin lattice relaxation rate T_1^{-1} observed in the sample A was well reproduced by other samples A-2 and G. The sample A-2 was prepared from the same batch as the sample A. The temperature dependence of K for the sample A-2 and G is in good agreement with that for the sample A (Fig. D.3 (a)). T_1^{-1} for the samples A-2 and G shows T^3-behavior (Fig. D.3 (b)), which is fully consistent with the sample A. These results support our conclusion in the Section 4.4.
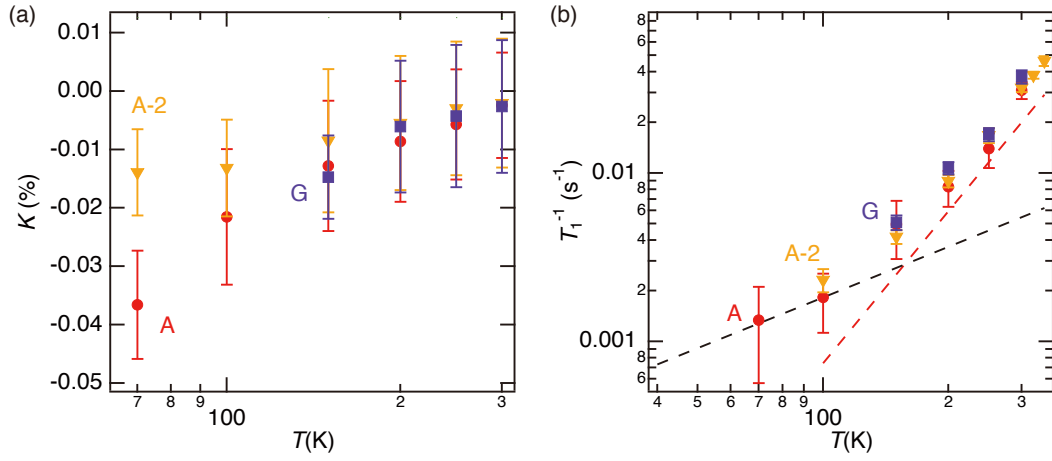
Fig. D.3. NMR Knight shift K and spin lattice relaxation rate T_1^{-1} for samples A-2 and G. (a) The observed K for the samples A-2 and G is in good agreement with that for the sample A. (b) T_1^{-1} for the sample A-2 and G shows T^3-behavior (red dashed line), consistent with the sample A.

Acknowledgements

References

[1] P. A. Dirac, in *Proceedings of the Royal Society of London A: Mathematical, Physical and Engineering Sciences*, Vol. 117, 778 (The Royal Society, 1928), pp. 610–624.

[2] K. Novoselov, A. K. Geim, S. Morozov, D. Jiang, M. Katsnelson, I. Grigorieva, S. Dubonos and A. Firsov, Nature **438**, 197–200 (2005).

[3] Y. Zhang, Y.-W. Tan, H. L. Stormer and P. Kim, Nature **438**, 201–204 (2005).

[4] Y. Xia, D. Qian, D. Hsieh, L. Wray, A. Pal, H. Lin, A. Bansil, D. Grauer, Y. Hor, R. Cava *et al.*, Nature Phys. **5**, 398–402 (2009).

[5] Y. Chen, J. Analytis, J.-H. Chu, Z. Liu, S.-K. Mo, X.-L. Qi, H. Zhang, D. Lu, X. Dai, Z. Fang *et al.*, Science **325**, 178–181 (2009).

[6] C. L. Kane and E. J. Mele, Phys. Rev. Lett. **95**, 146802 (2005).

[7] L. Fu and C. L. Kane, Phys. Rev. B **74**, 195312 (2006).

[8] J. E. Moore and L. Balents, Phys. Rev. B **75**, 121306 (2007).

[9] L. Fu, C. L. Kane and E. J. Mele, Phys. Rev. Lett. **98**, 106803 (2007).

[10] L. Fu and C. L. Kane, Phys. Rev. B **76**, 045302 (2007).

[11] L. Fu, Phys. Rev. Lett. **106**, 106802 (2011).

[12] C.-Z. Chang, J. Zhang, X. Feng, J. Shen, Z. Zhang, M. Guo, K. Li, Y. Ou, P. Wei, L.-L. Wang *et al.*, Science **340**, 167–170 (2013).

[13] J. Checkelsky, R. Yoshimi, A. Tsukazaki, K. Takahashi, Y. Kozuka, J. Falson, M. Kawasaki and Y. Tokura, Nature Phys. **10**, 731–736 (2014).

[14] S. M. Young, S. Zaheer, J. C. Y. Teo, C. L. Kane, E. J. Mele and A. M. Rappe, Phys. Rev. Lett. **108**, 140405 (2012).

[15] Z. Wang, Y. Sun, X.-Q. Chen, C. Franchini, G. Xu, H. Weng, X. Dai and Z. Fang, Phys. Rev. B **85**, 195320 (2012).

[16] Z. Wang, H. Weng, Q. Wu, X. Dai and Z. Fang, Phys. Rev. B **88**, 125427 (2013).

[17] Z. Liu, B. Zhou, Y. Zhang, Z. Wang, H. Weng, D. Prabhakaran, S.-K. Mo, Z. Shen, Z. Fang, X. Dai *et al.*, Science **343**, 864–867 (2014).

[18] S.-Y. Xu, C. Liu, S. K. Kushwaha, R. Sankar, J. W. Krizan, I. Belopolski, M. Neupane, G. Bian, N. Alidoust, T.-R. Chang *et al.*, Science **347**, 294–298 (2015).

[19] M. Neupane, S.-Y. Xu, R. Sankar, N. Alidoust, G. Bian, C. Liu, I. Belopolski, T.-R. Chang, H.-T. Jeng, H. Lin, A. Bansil, F. Chou and M. Z. Hasan, Nature Commun. **5**, 3786 (2014).

[20] Z. Liu, J. Jiang, B. Zhou, Z. Wang, Y. Zhang, H. Weng, D. Prabhakaran, S. Mo, H. Peng, P. Dudin *et al.*, Nature Mater. **13**, 677 (2014).

[21] S. Borisenko, Q. Gibson, D. Evtushinsky, V. Zabolotnyy, B. Büchner and R. J. Cava, Phys. Rev. Lett. **113**, 027603 (2014).

[22] T. Liang, Q. Gibson, M. N. Ali, M. Liu, R. Cava and N. Ong, Nature Mater. **14**, 280–284 (2015).

[23] L. P. He, X. C. Hong, J. K. Dong, J. Pan, Z. Zhang, J. Zhang and S. Y. Li, Phys. Rev. Lett. **113**, 246402 (2014).

[24] A. Narayanan, M. D. Watson, S. F. Blake, N. Bruyant, L. Drigo, Y. L. Chen, D. Prabhakaran, B. Yan, C. Felser, T. Kong, P. C. Canfield and A. I. Coldea, Phys. Rev. Lett. **114**, 117201 (2015).

[25] J. Cao, S. Liang, C. Zhang, Y. Liu, J. Huang, Z. Jin, Z.-G. Chen, Z. Wang, Q. Wang, J. Zhao *et al.*, Nature Commun. **6**, 7779 (2015).

[26] J. Feng, Y. Pang, D. Wu, Z. Wang, H. Weng, J. Li, X. Dai, Z. Fang, Y. Shi and L. Lu, Phys. Rev. B **92**, 081306 (2015).

[27] Y. Zhao, H. Liu, C. Zhang, H. Wang, J. Wang, Z. Lin, Y. Xing, H. Lu, J. Liu, Y. Wang, S. M. Brombosz, Z. Xiao, S. Jia, X. C. Xie and J. Wang, Phys. Rev. X **5**, 031037 (2015).

[28] C.-Z. Li, L.-X. Wang, H. Liu, J. Wang, Z.-M. Liao and D.-P. Yu, Nature Commun. **6**, 10137 (2015).

[29] H. Li, H. He, H.-Z. Lu, H. Zhang, H. Liu, R. Ma, Z. Fan, S.-Q. Shen and J. Wang, Nature Commun. **7**, 10301 (2016).

[30] Z. Jia, C. Li, X. Li, J. Shi, Z. Liao, D. Yu and X. Wu, Nature Commun. **7**, 13013 (2016).

[31] M. Novak, S. Sasaki, K. Segawa and Y. Ando, Phys. Rev. B **91**, 041203 (2015).

[32] R. Y. Chen, S. J. Zhang, J. A. Schneeloch, C. Zhang, Q. Li, G. D. Gu and N. L. Wang, Phys. Rev. B **92**, 075107 (2015).

[33] Q. Li, D. E. Kharzeev, C. Zhang, Y. Huang, I. Pletikosić, A. V. Fedorov, R. D. Zhong, J. A. Schneeloch, G. D. Gu and T. Valla, Nature Phys. **12**, 550 (2016).

[34] G. Zheng, J. Lu, X. Zhu, W. Ning, Y. Han, H. Zhang, J. Zhang, C. Xi, J. Yang, H. Du, K. Yang, Y. Zhang and M. Tian, Phys. Rev. B **93**, 115414 (2016).

[35] T. Kariyado and M. Ogata, J. Phys. Soc. Jpn. **80**, 083704 (2011).

[36] B.-J. Yang and N. Nagaosa, Nature Commun. **5**, 4898 (2014).

[37] S. M. Young and C. L. Kane, Phys. Rev. Lett. **115**, 126803 (2015).

[38] X. Wan, A. M. Turner, A. Vishwanath and S. Y. Savrasov, Phys. Rev. B **83**, 205101 (2011).

[39] A. A. Burkov and L. Balents, Phys. Rev. Lett. **107**, 127205 (2011).

[40] G. B. Halász and L. Balents, Phys. Rev. B **85**, 035103 (2012).

[41] A. A. Zyuzin, S. Wu and A. A. Burkov, Phys. Rev. B **85**, 165110 (2012).

[42] S.-M. Huang, S.-Y. Xu, I. Belopolski, C.-C. Lee, G. Chang, B. Wang, N. Alidoust, G. Bian, M. Neupane, C. Zhang *et al.*, Nature Commun. **6**, 7373 (2015).

[43] H. Weng, C. Fang, Z. Fang, B. A. Bernevig and X. Dai, Phys. Rev. X **5**, 011029 (2015).

[44] S.-Y. Xu, I. Belopolski, N. Alidoust, M. Neupane, G. Bian, C. Zhang, R. Sankar, G. Chang, Z. Yuan, C.-C. Lee *et al.*, Science **349**, 613–617 (2015).

[45] L. Yang, Z. Liu, Y. Sun, H. Peng, H. Yang, T. Zhang, B. Zhou, Y. Zhang, Y. Guo, M. Rahn *et al.*, Nature Phys. **11**, 728–732 (2015).

[46] B. Lv, N. Xu, H. Weng, J. Ma, P. Richard, X. Huang, L. Zhao, G. Chen, C. Matt, F. Bisti *et al.*, Nature Phys. **11**, 724–727 (2015).

[47] B. Q. Lv, H. M. Weng, B. B. Fu, X. P. Wang, H. Miao, J. Ma, P. Richard, X. C. Huang, L. X. Zhao, G. F. Chen, Z. Fang, X. Dai, T. Qian and H. Ding, Phys. Rev. X **5**, 031013 (2015).

[48] S. Nakatsuji, N. Kiyohara and T. Higo, Nature **527**, 212 (2015).

[49] K. Kuroda, T. Tomita, M.-T. Suzuki, C. Bareille, A. Nugroho, P. Goswami, M. Ochi, M. Ikhlas, M. Nakayama, S. Akebi *et al.*, Nature Mater. **16**, 1090 (2017).

[50] H. Yang, Y. Sun, Y. Zhang, W.-J. Shi, S. S. Parkin and B. Yan, New J. Phys. **19**, 015008

(2017).

[51] E. Liu, Y. Sun, N. Kumar, L. Muechler, A. Sun, L. Jiao, S.-Y. Yang, D. Liu, A. Liang, Q. Xu *et al.*, Nature Phys. **14**, 1125 (2018).

[52] Q. Xu, E. Liu, W. Shi, L. Muechler, J. Gayles, C. Felser and Y. Sun, Phys. Rev. B **97**, 235416 (2018).

[53] A. A. Soluyanov, D. Gresch, Z. Wang, Q. Wu, M. Troyer, X. Dai and B. A. Bernevig, Nature **527**, 495–498 (2015).

[54] Y. Wu, D. Mou, N. H. Jo, K. Sun, L. Huang, S. L. Bud'ko, P. C. Canfield and A. Kaminski, Phys. Rev. B **94**, 121113 (2016).

[55] Y. Sun, S.-C. Wu, M. N. Ali, C. Felser and B. Yan, Phys. Rev. B **92**, 161107 (2015).

[56] Z. Wang, D. Gresch, A. A. Soluyanov, W. Xie, S. Kushwaha, X. Dai, M. Troyer, R. J. Cava and B. A. Bernevig, Phys. Rev. Lett. **117**, 056805 (2016).

[57] K. Deng, G. Wan, P. Deng, K. Zhang, S. Ding, E. Wang, M. Yan, H. Huang, H. Zhang, Z. Xu, J. Denlinger, A. Fedorov, H. Yang, W. Duan, H. Yao, Y. Wu, S. Fan, H. Zhang, X. Chen and S. Zhou, Nature Phys. **12**, 1105–1110 (2016).

[58] A. A. Burkov, M. D. Hook and L. Balents, Phys. Rev. B **84**, 235126 (2011).

[59] J.-M. Carter, V. V. Shankar, M. A. Zeb and H.-Y. Kee, Phys. Rev. B **85**, 115105 (2012).

[60] C. Fang, Y. Chen, H.-Y. Kee and L. Fu, Phys. Rev. B **92**, 081201 (2015).

[61] Y. F. Nie, P. D. C. King, C. H. Kim, M. Uchida, H. I. Wei, B. D. Faeth, J. P. Ruf, J. P. C. Ruff, L. Xie, X. Pan, C. J. Fennie, D. G. Schlom and K. M. Shen, Phys. Rev. Lett. **114**, 016401 (2015).

[62] Z. Liu, M. Li, Q. Li, J. Liu, W. Li, H. Yang, Q. Yao, C. Fan, X. Wan, Z. Wang *et al.*, Sci. Rep. **6**, 30309 (2016).

[63] J. Fujioka, R. Yamada, M. Kawamura, S. Sakai, M. Hirayama, R. Arita, T. Okawa, D. Hashizume, M. Hoshino and Y. Tokura, Nature Commun. **10**, 362 (2019).

[64] M. Negishi, N. Hiraoka, D. Nishio-Hamane and H. Takagi, APL Materials **7**, 121101 (2019).

[65] L. M. Schoop, M. N. Ali, C. Straßer, A. Topp, A. Varykhalov, D. Marchenko, V. Duppel, S. S. Parkin, B. V. Lotsch and C. R. Ast, Nature Commun. **7**, 11696 (2016).

[66] M. Neupane, I. Belopolski, M. M. Hosen, D. S. Sanchez, R. Sankar, M. Szlawska, S.-Y. Xu, K. Dimitri, N. Dhakal, P. Maldonado, P. M. Oppeneer, D. Kaczorowski, F. Chou, M. Z. Hasan and T. Durakiewicz, Phys. Rev. B **93**, 201104 (2016).

[67] C. Chen, X. Xu, J. Jiang, S.-C. Wu, Y. P. Qi, L. X. Yang, M. X. Wang, Y. Sun, N. B. M. Schröter, H. F. Yang, L. M. Schoop, Y. Y. Lv, J. Zhou, Y. B. Chen, S. H. Yao, M. H. Lu, Y. F. Chen, C. Felser, B. H. Yan, Z. K. Liu and Y. L. Chen, Phys. Rev. B **95**, 125126 (2017).

[68] M. R. van Delft, S. Pezzini, T. Khouri, C. S. A. Müßller, M. Breitkreiz, L. M. Schoop, A. Carrington, N. E. Hussey and S. Wiedmann, Phys. Rev. Lett. **121**, 256602 (2018).

[69] A. Yamakage, Y. Yamakawa, Y. Tanaka and Y. Okamoto, J. Phys. Soc. Jpn. **85**, 013708 (2015).

[70] Y. Okamoto, T. Inohara, A. Yamakage, Y. Yamakawa and K. Takenaka, J. Phys. Soc. Jpn. **85**, 123701 (2016).

[71] K. Miyagawa, M. Hirayama, M. Tamura and K. Kanoda, J. Phys. Soc. Jpn. **79**, 063703 (2010).

[72] H. Yasuoka, T. Kubo, Y. Kishimoto, D. Kasinathan, M. Schmidt, B. Yan, Y. Zhang, H. Tou, C. Felser, A. P. Mackenzie and M. Baenitz, Phys. Rev. Lett. **118**, 236403 (2017).

[73] S. Kitagawa, K. Ishida, M. Oudah, J. N. Hausmann, A. Ikeda, S. Yonezawa and Y. Maeno, Phys. Rev. B **98**, 100503 (2018).

[74] G. P. Mikitik and Y. V. Sharlai, Phys. Rev. Lett. **82**, 2147–2150 (1999).

[75] D. Xiao, M.-C. Chang and Q. Niu, Rev. Mod. Phys. **82**, 1959–2007 (2010).

[76] H. B. Nielsen and M. Ninomiya, Phys. Lett. B **130**, 389–396 (1983).

[77] D. T. Son and B. Z. Spivak, Phys. Rev. B **88**, 104412 (2013).

[78] K.-Y. Yang, Y.-M. Lu and Y. Ran, Phys. Rev. B **84**, 075129 (2011).

[79] A. A. Burkov, Phys. Rev. B **91**, 245157 (2015).

[80] Y. Fuseya, M. Ogata and H. Fukuyama, J. Phys. Soc. Jpn. **84**, 012001 (2014).

[81] J. Fuchs, F. Piéchon, M. Goerbig and G. Montambaux, The European Physical Journal B **77**, 351–362 (2010).

[82] A. R. Wright and R. H. McKenzie, Phys. Rev. B **87**, 085411 (2013).

[83] I. M. Lifshitz and A. M. Kosevich, Zh. Eksp. Teor. Fiz. **29**, 730 (1955).

[84] I. A. Luk'yanchuk and Y. Kopelevich, Phys. Rev. Lett. **93**, 166402 (2004).

[85] I. A. Luk'yanchuk and Y. Kopelevich, Phys. Rev. Lett. **97**, 256801 (2006).

[86] J. Xiong, Y. Luo, Y. Khoo, S. Jia, R. J. Cava and N. P. Ong, Phys. Rev. B **86**, 045314 (2012).

[87] 安藤陽一 , トポロジカル絶縁体入門 , (講談社 , 2014).

[88] I. Lifshitz and A. Kosevich, Sov. Phys. JETP **2**, 636–645 (1956).

[89] A. A. Abrikosov, Phys. Rev. B **58**, 2788–2794 (1998).

[90] S. Suetsugu, K. Hayama, A. W. Rost, J. Nuss, C. Mühle, J. Kim, K. Kitagawa and H. Takagi, Phys. Rev. B **98**, 115203 (2018).

[91] M. Parish and P. Littlewood, Nature **426**, 162–165 (2003).

[92] M. M. Parish and P. B. Littlewood, Phys. Rev. B **72**, 094417 (2005).

[93] J. Hu, M. M. Parish and T. F. Rosenbaum, Phys. Rev. B **75**, 214203 (2007).

[94] T. Khouri, U. Zeitler, C. Reichl, W. Wegscheider, N. E. Hussey, S. Wiedmann and J. C. Maan, Phys. Rev. Lett. **117**, 256601 (2016).

[95] S. L. Adler, Phys. Rev. **177**, 2426–2438 (1969).

[96] J. S. Bell and R. Jackiw, Il Nuovo Cimento A **60**, 47–61 (1969).

[97] M. E. Peskin and D. V. Schroeder, *An Introduction to Quantum Field Theory*, (Westview Press, 2002).

[98] J. Xiong, S. K. Kushwaha, T. Liang, J. W. Krizan, M. Hirschberger, W. Wang, R. Cava and N. Ong, Science **350**, 413–416 (2015).

[99] X. Huang, L. Zhao, Y. Long, P. Wang, D. Chen, Z. Yang, H. Liang, M. Xue, H. Weng, Z. Fang, X. Dai and G. Chen, Phys. Rev. X **5**, 031023 (2015).

[100] C.-L. Zhang, S.-Y. Xu, I. Belopolski, Z. Yuan, Z. Lin, B. Tong, G. Bian, N. Alidoust, C.-C. Lee, S.-M. Huang *et al.*, Nature Commun. **7**, 10735 (2016).

[101] Z. Wang, Y. Zheng, Z. Shen, Y. Lu, H. Fang, F. Sheng, Y. Zhou, X. Yang, Y. Li, C. Feng and Z.-A. Xu, Phys. Rev. B **93**, 121112 (2016).

[102] M. Hirschberger, S. Kushwaha, Z. Wang, Q. Gibson, C. A. Belvin, B. Bernevig, R. Cava and N. Ong, Nature Mater. **15**, 1161–1165 (2016).

[103] F. Arnold, C. Shekhar, S.-C. Wu, Y. Sun, R. D. dos Reis, N. Kumar, M. Naumann, M. O. Ajeesh, M. Schmidt, A. G. Grushin *et al.*, Nature Commun. **7**, 11615 (2016).

[104] R. Dos, M. Ajeesh, N. Kumar, F. Arnold, C. Shekhar, M. Naumann, M. Schmidt, M. Nicklas and E. Hassinger, New J. Phys. **18**, 085006 (2016).

[105] S. Liang, J. Lin, S. Kushwaha, J. Xing, N. Ni, R. J. Cava and N. P. Ong, Phys. Rev. X **8**, 031002 (2018).

[106] A. A. Burkov, Phys. Rev. B **96**, 041110 (2017).

[107] S. Nandy, G. Sharma, A. Taraphder and S. Tewari, Phys. Rev. Lett. **119**, 176804 (2017).

[108] N. Kumar, S. N. Guin, C. Felser and C. Shekhar, Phys. Rev. B **98**, 041103 (2018).

[109] H. Li, H.-W. Wang, H. He, J. Wang and S.-Q. Shen, Phys. Rev. B **97**, 201110 (2018).

[110] M. Ogata and H. Fukuyama, J. Phys. Soc. Jpn. **84**, 124708 (2015).

[111] H. Fukuyama and R. Kubo, J. Phys. Soc. Jpn. **28**, 570–581 (1970).

[112] A. Goetz and A. B. Focke, Phys. Rev. **45**, 170–199 (1934).

[113] D. Shoenberg and M. Z. Uddin, Proceedings of the Royal Society of London. Series A, Mathematical and Physical Sciences **156**, 687–701 (1936).

[114] L. Wehrli, Physik der kondensierten Materie **8**, 87–128 (1968).

[115] F. Orbanić, M. Novak, M. Baćani and I. Kokanović, Phys. Rev. B **95**, 035208 (2017).

[116] A. Pariari and P. Mandal, Sci. Rep. **7**, 40327 (2017).

[117] N. L. Nair, P. T. Dumitrescu, S. Channa, S. M. Griffin, J. B. Neaton, A. C. Potter and J. G. Analytis, Phys. Rev. B **97**, 041111 (2018).

[118] A. Abragam, *The Principles of Nuclear Magnetism*, (Clarendon Press, 1961).

[119] 朝山邦輔, 遍歴電子系の核磁気共鳴 - 金属磁性と超伝導 -, (裳華房, 2002).

[120] T. Kariyado, *Three-Dimensional Dirac Electron Systems in the Family of Inverse-Perovskite Material Ca_3PbO*, Ph.D. thesis, Univ. of Tokyo (2012).

[121] H. Maebashi, M. Ogata and H. Fukuyama, J. Phys. Soc. Jpn. **86**, 083702 (2017).

[122] H. Maebashi, T. Hirosawa, M. Ogata and H. Fukuyama, Journal of Physics and Chemistry of Solids **128**, 138–143 (2019).

[123] 久保亮吾 , 大学演習 熱学・統計力学 , (裳華房 , 1961).

[124] G. C. Carter, L. H. Bennett and D. J. Kahan, *Metallic shifts in NMR, Part I*, (Pergamon Oxford, 1977).

[125] T. Kariyado and M. Ogata, J. Phys. Soc. Jpn. **81**, 064701 (2012).

[126] T. H. Hsieh, J. Liu and L. Fu, Phys. Rev. B **90**, 081112 (2014).

[127] C.-K. Chiu, Y.-H. Chan, X. Li, Y. Nohara and A. P. Schnyder, Phys. Rev. B **95**, 035151 (2017).

[128] P. Dziawa, B. Kowalski, K. Dybko, R. Buczko, A. Szczerbakow, M. Szot, E. Łusakowska, T. Balasubramanian, B. M. Wojek, M. Berntsen *et al.*, Nature Mater. **11**, 1023–1027 (2012).

[129] T. Liang, Q. Gibson, J. Xiong, M. Hirschberger, S. P. Koduvayur, R. Cava and N. Ong, Nature Commun. **4**, 2696 (2013).

[130] F. Schindler, A. M. Cook, M. G. Vergniory, Z. Wang, S. S. Parkin, B. A. Bernevig and T. Neupert, Sci. Adv. **4**, eaat0346 (2018).

[131] Y. Obata, R. Yukawa, K. Horiba, H. Kumigashira, Y. Toda, S. Matsuishi and H. Hosono, Phys. Rev. B **96**, 155109 (2017).

[132] S. Suetsugu, *Electromagnetic response of three-dimensional Dirac electrons in anti-perovskites*, Masters thesis, Univ. of Tokyo (2017).

[133] M. Oudah, A. Ikeda, J. N. Hausmann, S. Yonezawa, T. Fukumoto, S. Kobayashi, M. Sato and Y. Maeno, Nature Commun. **7**, 13617 (2016).

[134] H. Nakamura, J. Merz, E. Khalaf, P. Ostrovsky, A. Yaresko, D. Samal and H. Takagi, arXiv preprint arXiv:1806.08712 (2018).

[135] D. Huang, H. Nakamura, K. Küster, A. Yaresko, D. Samal, N. B. M. Schröter, V. N. Strocov, U. Starke and H. Takagi, Phys. Rev. Materials **3**, 124203 (2019).

[136] J. Nuss, C. Mühle, K. Hayama, V. Abdolazimi and H. Takagi, Acta Crystallographica Section B: Structural Science, Crystal Engineering and Materials **71**, 300–312 (2015).

[137] A. W. Rost, J. Kim, S. Suetsugu, V. Abdolazimi, K. Hayama, J. Bruin, C. Mühle, K. Kitagawa, A. Yaresko, J. Nuss and H. Takagi, APL Materials (to be published).

[138] S. Jeon, B. B. Zhou, A. Gyenis, B. E. Feldman, I. Kimchi, A. C. Potter, Q. D. Gibson, R. J. Cava, A. Vishwanath and A. Yazdani, Nature Mater. **13**, 851 (2014).

[139] T. Sato, K. Segawa, K. Kosaka, S. Souma, K. Nakayama, K. Eto, T. Minami, Y. Ando and T. Takahashi, Nature Phys. **7**, 840–844 (2011).

[140] S.-Y. Xu, Y. Xia, L. Wray, S. Jia, F. Meier, J. Dil, J. Osterwalder, B. Slomski, A. Bansil, H. Lin *et al.*, Science **332**, 560–564 (2011).

[141] H. Weng, X. Dai and Z. Fang, Phys. Rev. X **4**, 011002 (2014).

[142] G. Manzoni, L. Gragnaniello, G. Autès, T. Kuhn, A. Sterzi, F. Cilento, M. Zacchigna, V. Enenkel, I. Vobornik, L. Barba, F. Bisti, P. Bugnon, A. Magrez, V. N. Strocov, H. Berger, O. V. Yazyev, M. Fonin, F. Parmigiani and A. Crepaldi, Phys. Rev. Lett. **117**, 237601 (2016).

[143] Y. Liu and R. E. Allen, Phys. Rev. B **52**, 1566–1577 (1995).

[144] B. F. Williams and R. R. Hewitt, Phys. Rev. **146**, 286–290 (1966).

[145] F. N. Gygax, A. Schenck, A. J. van Wal and S. Barth, Phys. Rev. Lett. **56**, 2842–2845 (1986).

[146] E. Lippelt, P. Birrer, F. Gygax, B. Hitti, A. Schenck and M. Weber, Zeitschrift für Physik B Condensed Matter **86**, 367–374 (1992).

[147] A. Berger, H. Bertschat, H.-E. Mahnke, B. Spellmeyer and W. Shen, Hyperfine Interactions **34**, 547–551 (1987).

[148] W. Shen, A. Berger, H. Bertschat, H.-E. Mahnke and B. Spellmeyer, Phys. Lett. A **125**, 489–492 (1987).

[149] W. A. MacFarlane, C. B. L. Tschense, T. Buck, K. H. Chow, D. L. Cortie, A. N. Hariwal, R. F. Kiefl, D. Koumoulis, C. D. P. Levy, I. McKenzie, F. H. McGee, G. D. Morris, M. R. Pearson, Q. Song, D. Wang, Y. S. Hor and R. J. Cava, Phys. Rev. B **90**, 214422 (2014).

[150] J. Kim, *Synthesis, structure, and physical properties of M$_2$Tt and M$_3$TtO compounds (M = Ca, Sr, Ba; Tt = Sn, Pb)*, Masters thesis, Univ. of Stuttgart (2015).

[151] N. P. Butch, P. Syers, K. Kirshenbaum, A. P. Hope and J. Paglione, Phys. Rev. B **84**, 220504 (2011).

[152] W. Wang, Y. Du, G. Xu, X. Zhang, E. Liu, Z. Liu, Y. Shi, J. Chen, G. Wu and X.-x. Zhang, Sci. Rep. **3**, 2181 (2013).

[153] O. Pavlosiuk, D. Kaczorowski and P. Wiśniewsk, Sci. Rep. **5**, 9158 (2015).

[154] A. A. Taskin and Y. Ando, Phys. Rev. B **84**, 035301 (2011).

[155] A. Alexandradinata and L. Glazman, Phys. Rev. B **97**, 144422 (2018).

[156] G. Vignale, Phys. Rev. Lett. **67**, 358–361 (1991).

[157] T. Hirosawa, H. Maebashi and M. Ogata, J. Phys. Soc. Jpn. **86**, 063705 (2017).

[158] A. Lurio and D. A. Landman, Journal of the Optical Society of America **60**, 759–763 (
1970).

[159] C. R. Hewes, M. S. Adler and S. D. Senturia, Phys. Rev. B **7**, 5195–5212 (1973).

[160] L. Tterlikkis, S. D. Mahanti and T. P. Das, Phys. Rev. B **1**, 2041–2047 (1970).

[161] X. Zhang, Z. Hou, Y. Wang, G. Xu, C. Shi, E. Liu, X. Xi, W. Wang, G. Wu and X.-
x. Zhang, Sci. Rep. **6**, 23172 (2016).